

The Quasi Two-Day Wave -
its impact on the zonal mean circulation
and wave-wave interactions
in the middle atmosphere

Von der Fakultät für Physik und Geowissenschaften
der Universität Leipzig
genehmigte

DISSERTATION

zur Erlangung des akademischen Grades

DOCTOR RERUM NATURALIUM

Dr. rer. nat.
vorgelegt

von Dipl. Met. Kristina Fröhlich

geboren am 20.10.1970 in Halberstadt

Gutachter: Prof. Dr. Ch. Jacobi
Prof. Dr. A. Ebel
Prof. Dr. Y. Portnyagin

Tag der Verleihung: 21.11.2005

Fröhlich, Kristina

Die Quasi Zwei-Tage Welle - ihr Einfluss auf die mittlere Zonalzirkulation
sowie Untersuchungen der Welle-Welle Wechselwirkungen in der mittleren Atmosphäre

Universität Leipzig, Dissertation

125 S., 118 Lit., 56 Abb., 3 Anlagen

Referat:

Die Quasi Zwei-Tage Welle (QZTW) ist eine auffällige Erscheinung der sommerlichen mittleren Atmosphäre. Die beobachteten Eigenschaften der QZTW geben jedoch kein homogenes Bild wider, das auf einen wohldefinierten Ursprung weist. Die Welle zeigt sich sowohl mit der zonalen Wellenzahl (bezogen auf den Erdumfang) 3, wie auch der Wellenzahl 4. Ihre Periode liegt zwischen 45 und 53 Stunden. Dieses Phänomen ist auf beiden Erdhemisphären zur jeweiligen Sommerszeit zu beobachten, wobei die QZTW in der südlichen Hemisphäre stärkere Amplituden und kürzere Perioden aufweist als in der nördlichen Hemisphäre. Dieses vieldeutige Erscheinungsbild der Welle zieht die Frage ihres Ursprungs nach sich.

Theoretische Arbeiten leiten die QZTW als eine Lösung der Laplace'schen Gezeitengleichung mit den Eigenschaften einer Rossby-Schwerewelle her. Dieser Lösung entsprechend müßte die QZTW eine permanente Erscheinung in der mittleren Atmosphäre sein, somit wird jedoch nicht die plötzlich einsetzende Amplifizierung der Welle während des Sommers erklärt. Weitere Untersuchungen verschiedener Zirkulationsmodelle ergaben, dass sich eine QZTW an den Rändern instabiler Sommerjets der Mesosphäre entwickeln kann. Andere permanent vorherrschende Störungen der mittleren Atmosphäre sind im Zusammenhang mit der QZTW bisher nicht berücksichtigt worden. Auch fehlt bislang eine vollständige Beschreibung der Welle, die alle Beobachtungen im Ganzen erklärt.

Im Rahmen dieser Arbeit wurde das mechanistische Modell COMMA-LIM (Cologne Model of the Middle Atmosphere - Leipzig Institute for Meteorology) betrieben, um die QZTW als einen Eigenmode der Atmosphäre anzuregen und um sowohl ihre globale und vertikale Ausbreitung als auch ihren Einfluß auf die Zirkulation der mittleren Atmosphäre zu untersuchen. Desweiteren wurden Studien über die Wechselwirkungen der Welle mit anderen bedeutenden Störungen der mittleren Atmosphäre durchgeführt sowie untersucht, ob in COMMA-LIM eine QZTW aus instabilen Zuständen der Mesosphäre erwachsen kann.

Zusammenfassend kann gesagt werden, dass die QZTW und ihr charakteristisches Verhalten nicht nur durch Instabilitätsprozesse erklärt werden kann. Die Ergebnisse dieser Arbeit unterstreichen, dass die mittlere Atmosphäre verschiedene Lösungen für das "Quasi Zwei-Tage Welle" genannte Phänomen erlaubt.

Fröhlich, Kristina

The Quasi Two-Day Wave - its impact on the zonal mean circulation
and wave-wave interactions in the middle atmosphere

Universität Leipzig, Dissertation

125 Pages, 118 References, 56 Figures, 3 Appendices

Report:

The quasi two-day wave (QTDW) is a striking feature of the summer middle atmosphere. The observed properties of the wave do not give a unique picture that links to one well-defined mechanism. The wave appears with the zonal wave number 3 as well as with wave number 4. The period lies between 45-53 hours. This phenomenon can be observed in both hemispheres but with differences in period and strength of amplitudes which are stronger in the southern hemisphere than in the northern hemisphere. Thus, the wave's behaviour raises the question about its origin.

From the theoretical point of view, the QTDW can be derived as a solution of the Laplace' tidal equations. It is then referred to the Rossby-gravity mode (3,0). However, according to this solution the wave should be a permanent feature of the middle atmosphere. Thus, this theory cannot explain the sudden onset and offset of the wave during summer. On the other hand, several studies have shown, that a QTDW might develop as a result of an unstable jet in the summer mesosphere. On the other hand, the knowledge about the interactions of the QTDW with other disturbances in the middle atmosphere is still sparse and until now a complete description of the wave is missing.

Within the frame of this work the mechanistic model COMMA-LIM (Cologne Model of the Middle Atmosphere - Leipzig Institute for Meteorology) was used to study the wave, its propagation and impact on the mean flow by forcing it as an Eigenmode of the atmosphere. Furthermore, the interactions of the QTDW with the dominant disturbances of the middle atmosphere - e.g. gravity waves or other planetary waves - were investigated. Additionally, examinations on exciting a growing wave from unstable summer mesospheric jets were carried out.

In summary it could be shown, that not only instability processes can lead to a sudden increase in QTDW activity during summer. In particular, varying gravity waves or transient stationary planetary waves were found to be important in these processes. The numerical investigations on exciting an unstable growing QTDW from barotropic/baroclinic instability were not successful. It does not mean in turn, that a QTDW may not arise from instabilities, however the results underline that the atmosphere allows several solutions to the phenomenon called the QTDW.

Contents

1	Introduction	1
1.1	The middle and upper atmosphere	1
1.2	Waves in the middle atmosphere	3
1.2.1	Some basic definitions	3
1.2.2	A short survey of waves in the middle atmosphere	4
1.2.3	The basic equations of atmospheric motions	5
1.2.4	Laplace's tidal equations	6
1.2.5	Baroclinic and barotropic instability: the Rayleigh theorem	8
1.2.6	Vertical propagation of planetary waves and wave-mean flow interaction	9
1.3	Modelling the middle atmosphere	12
2	The Quasi Two-Day Wave - Observation and Theory	15
2.1	Observation of the QTDW	15
2.1.1	Radar and satellite observations	15
2.1.2	Further studies	19
2.2	Theory and model results	25
2.2.1	Normal mode studies	25
2.2.2	Instability studies	26
2.2.3	Coupling of Eigenmode and instability	28
2.2.4	Self-consistent excitation	29
2.2.5	Model studies	30
2.3	Summary and open questions	31

3	Description of the COMMA-LIM Model, Version 2	33
3.1	Description of the COMMA-Model, the LIM Version	33
3.1.1	Introduction	33
3.1.2	Numerical and computational properties	34
3.1.3	Dynamics	35
3.1.4	Radiation	44
4	Model Results and Discussion	48
4.1	The QTDW in the COMMA - LIM model	48
4.2	Steady forcing as an Eigenmode	48
4.3	Transient forcing	55
4.4	Interaction with gravity waves	60
4.5	Interaction with other planetary waves	66
4.6	Interaction with tides	73
4.7	Influence of the 11-year solar cycle on the QTDW	76
4.8	Experiments with unstable stages of the atmosphere	82
5	Conclusions and outlook	89
5.1	Summary	89
5.2	Outlook	91
	Symbols	92
A	Parameterisation of gravity waves	94
A.1	WKB solution	94
A.2	First order correction due to dissipative terms	95
A.3	Breaking of GWs due to convective instability	97
A.4	Mean flow acceleration due to dissipation and breaking of GWs	97
A.5	Heating/cooling of the atmosphere by GWs	99
B	Radiation	104
B.1	Heating due to absorption of solar radiation	104

B.2 Infrared radiation	107
C July climatology	109
C.1 Temperature field	109
C.2 Wind field	114
References	116
Acknowledgement	125

Chapter 1

Introduction

1.1 The middle and upper atmosphere

The middle and upper atmosphere includes the stratosphere, mesosphere and the lower thermosphere, which are found between the weather-active layer - the troposphere - and layers dominated by electrodynamical processes and plasma physics of the earth's geomagnetic field. The middle atmosphere is particularly important for researchers as it allows them to better understand transition processes coming from space and penetrating downwards. Further, it allows them to develop a comprehension of processes propagating upwards from the troposphere that can be traced and detected in higher altitudes. In order to estimate the meteorological influences on the troposphere that originate in the middle atmosphere and to be able to use the knowledge for space science a fundamental understanding of the inherent processes in this region is required.

The three spheres are divided into layers with boundaries between them based on the vertical structure of the temperature. The mean vertical structure of temperature can be explained in terms of absorption and emission of radiation by the gaseous constituents. The beginning of the stratosphere is marked by a temperature minimum - the *tropopause* - mainly caused by emissions of water vapour. Within the stratosphere temperature increases slowly with altitude to a maximum at about 50 *km* height due to absorption of radiation by ozone. Above this maximum - called *stratopause* - the temperature in the mesosphere drops again because of decreasing ozone concentration and increasing cooling due to carbon dioxide. Within this sphere at altitudes above 60 *km* the increasing mean free path between molecular collisions leads to a change in radiative processes. The local thermodynamic equilibrium (LTE) breaks and non-LTE conditions have to be considered. Molecular diffusion processes become more and more important. Each gas species that was well mixed below - e.g. nitrogen, oxygen and carbon dioxide - undergoes an exponential decay of density with height in the thermosphere determined by its molecular mass, so less massive species increasingly dominate with height. The temperature minimum marks

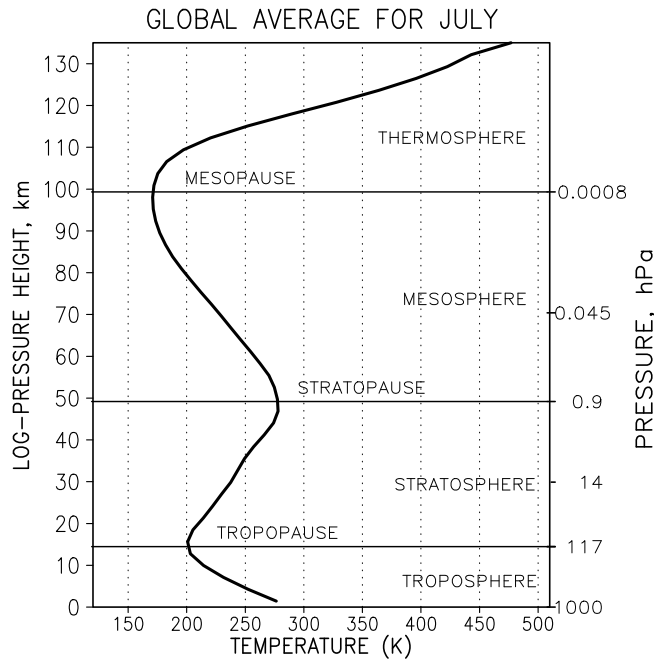


Figure 1.1: Globally averaged temperature profile for July as calculated with COMMA-LIM.

again the end of the mesosphere and is called *mesopause*. Higher in the thermosphere absorption of extreme ultraviolet radiation by molecular and atomic oxygen dominates the temperature structure.

A further interesting feature of this atmospheric region is the interaction between neutral and ionised particles. The ionosphere is the region in which a substantial portion of atoms and molecules have become electrically charged by a broad spectrum of visible and non-visible radiation, which dissociates and ionises the mixture of gases in the upper atmosphere. There, the amount of ionisation is large enough to influence the propagation of radio waves. It starts at mesospheric heights at around 50-60 km, extends throughout the whole thermosphere and has its upper boundary at heights of several earth radii, where ions emanating from the sun interact with ions in the atmosphere. Thus, with rising height electrodynamic forces exert an increasing influence on the movement of the neutral particles.

The differential heating of the atmosphere throughout the year leads to balancing motions of air masses. A moving air parcel in the earth's atmosphere is accelerated by the sum of the following forces: (i) the pressure gradient force, (ii) the gravitational and centrifugal force, (iii) the Coriolis force and (iv) friction, molecular diffusion and acceleration due to eddies. Thus, during solstices the middle atmosphere wind is characterised by a westward jet (*easterlies*) in the summer hemisphere and an eastward jet (*westerlies*) in the winter hemisphere. In contrast, westerlies dominate the stratosphere and mesosphere

during equinoxes when the air masses rise at the equator and drift into both spring and autumn hemispheres.

Several characteristic features of the middle atmosphere, such as the wind reversal in the mesopause region, the extreme cold summer mesopause polar region, the occurrence of sudden stratospheric warmings at the winter pole or the quasi-biennial oscillation in the equatorial stratosphere point to the important role *eddies* play in the middle atmosphere. Not all waves propagating in the middle atmosphere exert such a strong impact on the circulation, however, only the understanding about their origin, propagation and interaction processes gives a comprehensive picture of the middle atmosphere. This work focusses on the investigation of one striking phenomenon that arises regularly in the summer middle atmosphere: the quasi two-day wave (QTDW).

1.2 Waves in the middle atmosphere

1.2.1 Some basic definitions

A wave is a periodical process running in time and space. It is convenient to describe the waves with the EULERIAN-rule $e^{i\varphi} = \cos\varphi + i \sin\varphi$ as

$$\tilde{\Phi}(x, t) = \Phi_0 e^{i(kx - \omega t)}. \quad (1.1)$$

However, the plainest description of a wave propagating in one direction is taking the real part of the EULERIAN expression:

$$\text{Re}(\tilde{\Phi}(x, t)) = \Phi_0 \cos(kx - \omega t), \quad (1.2)$$

where Φ_0 means the amplitude (which is complex so it includes a constant phase factor), $k = \frac{2\pi}{\lambda}$ is the wave number with wavelength λ , and $\omega = \frac{2\pi}{T}$ is the angular frequency with period T . The argument of the cosine-function is called the phase φ of the wave and its characteristic is to remain constant, i.e.,

$$kx - \omega t = 0. \quad (1.3)$$

So, as t increases, x must also increase to keep the phase constant. The propagation speed of a point with constant phase is given by

$$c \equiv \left(\frac{dx}{dt}\right)_{\varphi=\text{const}} = \frac{\omega}{k} = \frac{\lambda}{T}. \quad (1.4)$$

Note, that the transport of momentum and energy via waves cannot be performed with the phase speed but with the group velocity. A superposition of two waves propagating in an arbitrary but the same direction with small different frequencies and wave numbers leads to a wave group. This wave packet can in turn be considered as a wave propagating

with a speed determined by the amplitude modulation of the two single waves. Then, the group velocity is determined by

$$\vec{c}_g = \frac{d\omega}{dK_i} = \nabla_{\vec{K}} \omega \quad (1.5)$$

where $\vec{K} = k \cdot i_1 + l \cdot i_2 + m \cdot i_3$ is the wave vector with its three components and thus leads the group velocity, \vec{c}_g , being a vector as well.

1.2.2 A short survey of waves in the middle atmosphere

Waves propagating in the middle atmosphere originate predominantly at tropospheric-tropopause levels. If they are able to propagate upwards, their amplitudes grow with height due to decreasing density of the atmosphere. During their propagation and succeeding dissipation the oscillations are influenced by the mean circulation and have in turn an impact on the middle atmosphere.

The smallest but nevertheless important waves in the atmosphere are *gravity waves* (GWs). Pure internal GWs owe their existence to stratification of the atmosphere, while inertio-gravity waves result from a combination of stratification and the Coriolis-effect. Gravity waves play an important role in the mesopause region where their increased amplitudes break and their momentum and heat is imposed on the circulation. Their horizontal wavelengths are in the range from around ten to several hundreds kilometres and their periods vary from minutes up to 8 hours. These waves are a permanent feature of the middle atmosphere but show a latitudinal and seasonal dependence.

The latter property is also valid for the migrating *tides* that are induced by the diurnal fluctuation of solar heating, in particular due to absorption of radiation by ozone and water vapour. They amplify also in the mesosphere-lower-thermosphere region (MLT). While the diurnal tide (period $T = 24 h$) has the zonal wave number 1, the semidiurnal tide ($T = 12 h$) shows wave number 2 and so forth.

Stationary planetary waves (SPWs) are waves whose surfaces of constant phase are fixed with respect to the earth. Since information propagates with the group velocity and not with phase speed, propagation can still occur. The stationary waves with zonal wave numbers 1 and 2 are striking features of the winter middle atmosphere.

Kelvin waves are eastward travelling planetary waves confined at equatorial latitudes; their meridional wind component is zero or small. Waves with a short period (e.g. $T \sim 3 days$) are able to propagate up into the MLT region while slower waves ($T \sim 15 days$) are trapped in the stratosphere. *Rossby-gravity waves* are in contrast equatorial waves that propagate westward and exhibit a nonzero meridional velocity wind component.

An important class of waves are *travelling planetary waves* or Rossby waves. These waves predominantly propagate westwards. In the middle atmosphere they have wave

numbers between 1 and 4, and periods between 2 days and 16 days. Many of them are able to propagate upwards through the winter hemisphere into the MLT region. The 5-day wave with zonal wave number 1 appears also in the summer hemisphere.

The following sections will give an overview of theoretical investigations on atmospheric waves. For a complete derivation the reader is referred to the literature, such as Andrews et al. (1987); Holton (1992).

1.2.3 The basic equations of atmospheric motions

Before one can discuss the waves that are perturbations on the basic state of the atmosphere, one has to be introduced into the non-linear differential equation system that describes the movement of a fluid parcel. The horizontal momentum equations and the thermodynamic equation in a log-isobaric system on a sphere can be written as (Andrews et al., 1987)

$$\begin{aligned} \frac{\partial u}{\partial t} = & - \frac{u}{a \cos \phi} \frac{\partial u}{\partial \lambda} - \frac{v}{a \cos \phi} \frac{\partial}{\partial \phi} (u \cos \phi) - w \frac{\partial u}{\partial z} \\ & + (f + \frac{u}{a} \tan \phi) v - \frac{1}{a \cos \phi} \frac{\partial \Phi}{\partial \lambda} + F_\lambda, \end{aligned} \quad (1.6)$$

$$\begin{aligned} \frac{\partial v}{\partial t} = & - \frac{u}{a \cos \phi} \frac{\partial v}{\partial \lambda} - \frac{v}{a} \frac{\partial v}{\partial \phi} - w \frac{\partial v}{\partial z} \\ & - (f + \frac{u}{a} \tan \phi) u - \frac{1}{a} \frac{\partial \Phi}{\partial \phi} + F_\phi, \end{aligned} \quad (1.7)$$

$$\frac{\partial T}{\partial t} = - \frac{u}{a \cos \phi} \frac{\partial T}{\partial \lambda} - \frac{v}{a} \frac{\partial T}{\partial \phi} - w \left(\frac{\partial T}{\partial z} + \frac{\kappa T}{H} \right) + \frac{J}{c_p}. \quad (1.8)$$

These equations express, respectively, the momentum balance in the zonal and meridional directions, and the thermodynamics relation between diabatic heating and the material exchange of temperature. The hydrostatic stability in the vertical column and the conservation of mass - the continuity equation - are expressed as:

$$\frac{\partial \Phi}{\partial z} = \frac{RT}{H}, \quad (1.9)$$

$$\frac{1}{a \cos \phi} \frac{\partial u}{\partial \lambda} + \frac{1}{a \cos \phi} \frac{\partial}{\partial \phi} (v \cos \phi) + \frac{1}{\rho_0} \frac{\partial}{\partial z} (\rho_0 w) = 0, \quad (1.10)$$

where $\rho_0 = \rho_s e^{(-z/H)}$. An explanation of the symbols is given in the list of symbols. The hydrostatic assumption means that acceleration due to gravity is large against vertical acceleration. The vertical component of Coriolis force can therefore be neglected.

1.2.4 Laplace's tidal equations

The atmosphere may be regarded as a system of coupled particles. If such a system is disturbed it develops vibrations whose frequencies are equal for all particles in the medium. These frequencies are called Eigenfrequencies and an Eigenfunction/Eigenvalue pair of such a solution constitutes a mode. Mainly Laplace developed the mathematical description of tides as arising Eigenmodes for a fluid on a rotating body. He used the *perturbation theory* which states that on a known non-linear basic state of a fluid, perturbations are superimposed which are small against the basic state. This assumption leads to a linearised differential equation system for the perturbations because the non-linear terms are of the second order and therefore negligible. In the simplest case further assumptions are:

- an atmosphere at rest so that $u_0 = v_0 = 0$ and because of the thermal wind equation the meridional gradient of basic temperature $\partial_\phi \bar{T}$ also vanishes (partial differentiations with respect to a variable x are abbreviated through $\frac{\partial}{\partial x} \equiv \partial_x$),
- no mechanical and thermal forcing or dissipation is considered: $F_\lambda = F_\phi = J = 0$.

From the linearised and simplified equations (not shown here) under equivalent boundary conditions wave-like solutions are sought. An important method in this way is the separation of the vertical dependence from the horizontal and time dependence

$$(u', v', \Phi') = e^{z/2H} U(z) [\tilde{u}(\lambda, \phi, t), \tilde{v}(\lambda, \phi, t), \tilde{\Phi}(\lambda, \phi, t)], \quad (1.11)$$

$$w' = e^{z/2H} W(z) \tilde{w}(\lambda, \phi, t). \quad (1.12)$$

Insertion of the solution (1.11) into the momentum equations yields to expressions that only contain a (λ, ϕ, t) dependence

$$\partial_t \tilde{u} - f \tilde{v} + \frac{\partial_\lambda \tilde{\Phi}}{a \cos \phi} = 0, \quad (1.13)$$

$$\partial_t \tilde{v} + f \tilde{u} + \frac{\partial_\phi \tilde{\Phi}}{a} = 0, \quad (1.14)$$

while solutions (1.11, 1.12) applied to the continuity and thermodynamic equation involve the z dependence as well. However, it turns out that U can be represented in terms of W

$$U = \frac{dW}{dz} - \frac{W}{2H}. \quad (1.15)$$

Given this relation and examining the z -dependent continuity equation one can write this equation with the aid of the thermodynamic equation as

$$\frac{\partial_\lambda \tilde{u} + \partial_\phi (\tilde{v} \cos \phi)}{a \cos \phi} + \frac{\partial_t \tilde{\Phi}}{g h} = 0, \quad (1.16)$$

where $(gh)^{-1}$ is a separation constant and h has dimensions of length. The *equivalent depth* h of the fluid has to be small against the earth radius a . And $\tilde{\Phi}/g$ is the departure of this mean value h . The three equations (1.13, 1.14, 1.16) form the basis of the horizontal and time structure for disturbances to a thin layer of fluid on a sphere.

After further manipulation one obtains the following for the vertical structure equation:

$$\frac{d^2 W}{dz^2} + \left(\frac{N^2}{gh} - \frac{1}{4H^2} \right) W = 0. \quad (1.17)$$

The procedure for finding solutions to Laplace's tidal equations proceeds in two stages: first, Eq.(1.17) has to be solved under given boundary conditions as an Eigenvalue problem for the equivalent depth h . Then given h , solutions for the horizontal structure are sought in the form

$$\{\tilde{u}, \tilde{v}, \tilde{\Phi}\} = \text{Re}\{[\hat{u}(\phi), \hat{v}(\phi), \hat{\Phi}(\phi)] \exp i(s\lambda - 2\Omega\sigma t)\} \quad (1.18)$$

with zonal wave number k and period $2\pi/2\Omega\sigma$, where $\Omega = 2\pi(\text{sidereal day})^{-1}$ is the earth's rotation rate. Solving Eqs. (1.13) and (1.14) for \hat{u} and \hat{v} and inserting these into Eq.(1.16) we obtain after careful calculations the *Laplace's tidal equation*

$$\mathcal{L}\hat{\Phi} + \gamma\hat{\Phi} = 0. \quad (1.19)$$

Here $\gamma \equiv 4\Omega^2 a^2/gh$ is called Lambs parameter and

$$\mathcal{L} \equiv \frac{d}{d\mu} \left[\frac{(1-\mu^2)}{(\sigma^2 - \mu^2)} \frac{d}{d\mu} \right] - \frac{1}{\sigma^2 - \mu^2} \left[\frac{-k(\sigma^2 + \mu^2)}{\sigma(\sigma^2 - \mu^2)} + \frac{k^2}{1 - \mu^2} \right] \quad (1.20)$$

is a second order differential operator in the variable

$$\mu \equiv \sin \phi \quad (-1 \leq \mu \leq 1). \quad (1.21)$$

The appropriate boundary conditions are that $\hat{\Phi}$ is bounded at the poles, $\mu = \pm 1$. Given these boundary conditions and Eigenvalues $\gamma_n \propto \frac{1}{h}$, corresponding Eigenfunctions Θ_n can be calculated which are called *Hough functions*. Atmospheric tides, gravity waves, mixed planetary-gravity (or Rossby-gravity) waves, Kelvin waves and Rossby waves can all be derived from the Laplace tidal equations.

In the case of deriving a free travelling planetary wave with specified wave number k in an isothermal atmosphere a solution for the vertical structure equation (1.17) with appropriate boundary conditions and $W \rightarrow 0$ as $z \rightarrow 0$ can be obtained for

$$h = \frac{H}{1 - \kappa}, \quad (1.22)$$

where $(1 - \kappa)^{-1} = c_p/c_v$. Then $W(z) \propto \exp[(\kappa - \frac{1}{2})z/H]$ and hence

$$w' \propto e^{\kappa z/H}. \quad (1.23)$$

It can be shown that Φ', u', v' and T' have the same z dependence. The wave therefore has no phase tilt with height. Considering amplitudes of velocity and temperature fields one finds that these amplitudes grow with height but the corresponding energy density $\frac{1}{2}\rho_0(\bar{u}'^2 + \bar{v}'^2 + \bar{\Phi}'^2 N^{-2})$ is confined to lower levels since $\rho_0 \propto e^{-z/H}$. Such a free travelling planetary wave is also called an *external* or an *evanescent* wave or is named as Lamb wave and cannot transport energy upwards. Note that this wave here is derived without mean winds and will alter its structure under the inclusion of latitudinally and vertically varying winds. But then it is no longer possible to separate the equations and the problem can only be solved numerically.

There exists a solution with a period of quasi two days and a zonal wavenumber of three, which can be interpreted as an asymmetric mixed Rossby-gravity mode (3,0). The nomenclature *mode* ($k, |n| - k$) used for planetary waves is due to Longuet-Higgins (1968) where k refers to the zonal wavenumber and n provides information on the number of latitudinal nodes and symmetry characterising Θ_n . For asymmetric modes the meridional wind shows a symmetric behaviour whereas the other variables change sign at the equatorial node.

1.2.5 Baroclinic and barotropic instability: the Rayleigh theorem

Another mechanism of wave excitation results from unstable conditions in the atmosphere. In this case their amplitudes grow without limit and if they take the form of Eq.(1.1), their frequencies are complex, with positive imaginary parts. Stability analysis of a realistic zonal wind profile $\bar{u} = \bar{u}(y, z)$ is difficult because of the non-separability of the y and z dependencies in the perturbation Eigenfunction-Eigenvalue problem. Rayleigh, as the first author in this field, developed necessary conditions for barotropic and baroclinic instabilities from an integral theorem. A derivation is given by Holton (1992) under the geostrophic approximation on a beta-plane with sidewall boundaries $y = \pm L$. He transformed the set of equations into the quasi-geostrophic vorticity equation with the streamfunction Ψ as the only dependent variable.

The main idea is to analyse the system of energetics so as to get information about stability properties when a perturbation streamfunction $\psi'(x, y, z, t) = \text{Re}(\Psi(y, z) \exp[ik(x - ct)])$ is imposed on a zonal flow. The perturbation consists of a single Fourier component, propagating in zonal direction with complex amplitude $\Psi(y, z) = \Psi_r + i\Psi_i$ and complex phase speed $c = c_r + ic_i$

$$\psi'(x, y, z) = e^{kc_it} [\Psi_r \cos k(x - c_r t) - \Psi_i \sin k(x - c_r t)]. \quad (1.24)$$

The obtained set of equations including the boundary conditions is now integrated over the latitude-height (y, z) domain and it turns out that

$$c_i \left[\int_{-L}^{+L} \int_0^\infty \frac{\partial \bar{q}}{\partial y} \frac{\rho_0 |\Psi|^2}{|\bar{u} - c|^2} dy dz - \int_{-L}^{+L} \frac{f_0^2}{N^2} \frac{\partial \bar{u}}{\partial z} \frac{\rho_0 |\Psi|^2}{|\bar{u} - c|^2} \Big|_{z=0} dy \right] = 0, \quad (1.25)$$

where $|\Psi|^2 = \Psi_r^2 + \Psi_i^2$ is the disturbance amplitude squared. Considering equation (1.25) we know that for unstable modes c_i must be nonzero. As $|\Psi|^2/|\bar{u} - c|^2$ is nonnegative, instability is possible only when $\partial\bar{u}/\partial z$ at the lower boundary and $\partial\bar{q}/\partial y$ in the whole domain satisfy certain constraints:

- If there is no meridional temperature gradient at the lower boundary, which implies $\partial\bar{u}/\partial z = 0$ at $z = 0$, the second integral in Eq.(1.25) vanishes. For an instability to occur the first integral thus must therefore vanish. This means $\partial\bar{q}/\partial y = 0$ somewhere. This condition is referred to as the *Rayleigh necessary condition*. Because $\partial\bar{q}/\partial y$ is normally positive we need an occurrence of a negative meridional gradient of quasi-geostrophic potential vorticity, if there is no temperature gradient at the lower boundary.
- If $\partial\bar{q}/\partial y \geq 0$ everywhere, a positive vertical shear of the zonal wind is needed somewhere at the lower boundary, provided that $c_i > 0$.
- If $\partial\bar{u}/\partial z < 0$ at $z = 0$, the meridional gradient of potential vorticity has to be negative somewhere for instability to occur.

The basic state potential vorticity gradient can be written in the form (Holton, 1992)

$$\frac{\partial\bar{q}}{\partial y} = \beta - \frac{\partial^2\bar{u}}{\partial y^2} - \frac{f_0^2}{N^2} \frac{\partial^2\bar{u}}{\partial z^2} + \frac{f_0^2}{N^2 H} \frac{\partial\bar{u}}{\partial z} - \frac{\partial}{\partial z} \left(\frac{f_0^2}{N^2} \right) \frac{\partial\bar{u}}{\partial z}. \quad (1.26)$$

Thus, since $\beta = 2\Omega a^{-1} \cos\phi_0$ is positive and f_0^2/N^2 is constant, a negative basic state potential vorticity gradient can occur only for strong positive mean flow curvature or strong vertical shear in the mean zonal wind. If one considers a vertical change in N^2 then the condition for instability is satisfied when $\partial\bar{u}/dz > 0$ if N^2 decreases with height or $\partial\bar{u}/dz < 0$ where N^2 increases with height. Instability associated with strong positive horizontal curvature is referred to as barotropic instability, whereas baroclinic instability depends on the vertical curvature of the jet.

Additionally, one can see, that baroclinic instability is more likely to occur at latitudes polewards of 20° North or South, because the Coriolis parameter damps all vertical terms very strongly and β increases towards the equator. All this stabilises the gradient of potential vorticity.

1.2.6 Vertical propagation of planetary waves and wave-mean flow interaction

Normally, the free travelling planetary waves as derived above are evanescent at greater heights so they need a continual forcing to maintain their amplitudes at lower levels (Andrews et al., 1987). To investigate the behaviour of vertical propagation of steady planetary

waves in a basic flow \bar{u} depending on y and z but under constant buoyancy frequency N , the quasi-geostrophic theory is again used, where the linearized potential vorticity equation is

$$\left(\frac{\partial}{\partial t} + \bar{u} \frac{\partial}{\partial x} \right) q' + \frac{\partial \bar{q}}{\partial y} \frac{\partial \psi'}{\partial x} = 0, \quad (1.27)$$

with

$$q' \equiv \nabla^2 \psi' + \frac{1}{\rho_0} \frac{\partial}{\partial z} \left(\rho_0 \frac{f_0^2}{N^2} \frac{\partial \psi'}{\partial z} \right) \quad (1.28)$$

and

$$\frac{\partial \bar{q}}{\partial y} = \beta - \frac{\partial^2 \bar{u}}{\partial y^2} - \frac{1}{\rho_0} \frac{\partial}{\partial z} \left(\rho_0 \frac{f_0^2}{N^2} \frac{\partial \bar{u}}{\partial z} \right) \quad (1.29)$$

(note that z here always refers to the log-pressure height).

Substituting the steady-wave form

$$\psi' = e^{z/2H} \operatorname{Re}[\Psi(y, z)e^{ik(x-ct)}] \quad (1.30)$$

one obtains

$$\frac{\partial^2 \Psi}{\partial y^2} + \frac{f_0^2}{N^2} \frac{\partial^2 \Psi}{\partial z^2} + n_k^2 \Psi = 0 \quad (1.31)$$

where

$$n_k^2(y, z) = \frac{\bar{q}_y}{\bar{u} - c} - k^2 - \frac{f_0^2}{N^2 4 H^2}. \quad (1.32)$$

The square of the *refractive index* n_k^2 states that waves propagate into regions with $n_k^2 > 0$ and avoid regions where $n_k^2 < 0$. This means that the first term of Eq.(1.32) has to be positive and has to dominate over terms 2 and 3. For a realisation, the same signs of both numerator and denominator are needed and the ratio of the two terms has to be large enough. Then, under assumption that $\bar{q}_y > 0$ westerly winds ($\bar{u} > 0$) will not filter out a wave with $c < 0$ but the higher the denominator the smaller the first term. On the other hand it is not necessary that \bar{u} remains westerly, but for easterly winds this wave can only propagate if its phase speed is faster than the zonal flow and thereby maintains a positive denominator. In regions of negative meridional potential vorticity gradient, $(\bar{u} - c) < 0$ would be necessary for the first term to be positive.

So, for relative simple wave propagation studies the refractive index gives useful information for Rossby-waves on a β -plane. However, in a more complex (model) atmosphere there exists not only one upward propagating wave but a superposition of upward and downward as well as northward and southward propagating waves (e.g. Harnik and Lindzen (2001), Harnik (2002)). In addition, the meridional and vertical wave numbers (l and m) satisfy the following dispersion relation:

$$m^2 \frac{f_0^2}{N^2} + l^2 = \frac{\bar{q}_y}{\bar{u} - c} - k^2 - \frac{f_0^2}{N^2 4 H^2} \equiv n_k^2(y, z). \quad (1.33)$$

It has been shown by Harnik and Lindzen (2001) that n_k^2 is strongly dominated by the meridional wavenumber and cannot reveal the existence of reflecting surfaces caused by the vertical wavenumber which are responsible for vertical propagation or evanescence of the considered waves. Furthermore, waves are able to tunnel small evanescent regions if their wavelengths are large enough. All this reduces the explanatory power of the refractive index.

Therefore, the Eliassen-Palm flux $\mathbf{F} \equiv (0, F^\phi, F^z)$, its divergence and related parameters are now commonly used to investigate wave properties. The vector components of Eliassen-Palm (EP) flux display the direction and magnitude of the eddy momentum and heat flux in a latitudinal-height β -plane:

$$F^\phi = -\rho_0 \overline{v' u'} \quad (1.34)$$

$$F^z = \rho_0 f_0 \overline{v' \theta'} / \bar{\theta}_z. \quad (1.35)$$

The divergence of the EP flux gives for the quasi-geostrophic β -plane case

$$\nabla \cdot \mathbf{F} \equiv -\rho_0 \frac{\partial \overline{v' u'}}{\partial y} + \rho_0 f_0 \frac{\partial \overline{v' \theta'}}{\partial \theta_z}. \quad (1.36)$$

\mathbf{F} is obtained by using the *transformed Eulerian-mean* equations (TEM), where the *Eulerian mean* is a *zonal mean* and all variables are separated into zonal mean parts and disturbing parts (e.g. Andrews et al. (1987)). Transformation of the Eulerian takes into account a *residual mean meridional circulation* $(0, v^*, w^*)$ which constitutes the mean meridional circulation if the wave driven part is known:

$$\bar{v}^* \equiv \bar{v}_a - \rho_0^{-1} (\rho_0 \overline{v' \theta'} / \theta_{0z})_z \quad (1.37)$$

$$\bar{w}^* \equiv \bar{w}_a + (\overline{v' \theta'} / \theta_{0z})_\phi, \quad (1.38)$$

where \bar{v}_a and \bar{w}_a denote the ageostrophic velocities for the quasi-geostrophic case. It follows for the zonal momentum TEM equation

$$\frac{\partial \bar{u}}{\partial t} - f_0 \bar{v}^* - \bar{\mathbf{X}} = \frac{\nabla \cdot \mathbf{F}}{\rho_0}, \quad (1.39)$$

where $\bar{\mathbf{X}}$ represents a non-conservative term. By considering Eq.(1.39) in the middle atmosphere it turns out that the mean residual meridional velocity, which becomes dominant in the MLT region, is mainly balanced by the non-conservative effects such as the drag exerted by breaking gravity waves. Therefore, the eddy-forcing terms, represented in $\rho_0^{-1} \nabla \cdot \mathbf{F}$ mainly affect the tendency $\partial_t \bar{u}$. A further conclusion is that for linear, steady, conservative waves on a purely zonal basic flow the divergence of EP flux vanishes (Eliassen and Palm, 1961). However, this result was later extended to include frictional and diabatic effects, spherical geometry and time-varying waves (Andrews and McIntyre, 1978). It takes now the form

$$\frac{\partial A}{\partial t} + \nabla \cdot \mathbf{F} = D + O(\alpha^3), \quad (1.40)$$

where A and D , like \mathbf{F} , are mean *quadratic* functions of disturbance quantities. A is called the "wave-activity density", and its time derivatives represent wave transience effects, vanishing for steady waves. The quantity D contains the frictional and diabatic effects, and thus vanishes for conservative waves. The term $O(\alpha^3)$, where α is the wave amplitude, represents non-linear wave effects, and diminishes for purely linear waves. If the wave is forced in a steady way $\partial A/\partial t = 0$ and the acceleration is related to dissipative processes.

Again, when considering one upward propagating wave it can be shown, that the group velocity

$$\mathbf{c}_g = \frac{\mathbf{F}}{A}, \quad (1.41)$$

whereas taking reflected waves into account the equation becomes more complicated and the group velocity is then called the *wave activity velocity*, denoted by \mathbf{V}_a .

1.3 Modelling the middle atmosphere

In order to study the atmospheric processes theoretically various numerical models have been developed, whose equipment was chosen depending on the focus of study and actual knowledge on physics, chemistry and numerics.

Global Circulation Models (GCMs) are complex three dimensional models of the atmosphere which include all known physical and to a large extent chemical processes of the atmosphere. The main focus is dedicated to the troposphere with a detailed description of the earth's surface and related processes; some models include an ocean-coupling. Stratosphere, mesosphere and thermosphere are used only as an extended upper boundary. But in recent years the interest in understanding the processes above has grown and therefore the middle and upper atmosphere now receive more attention. Several additional processes have to be described or parameterised, such as the upward propagating gravity waves, which break in mesopause regions and alter the mean flow by imposing momentum and heat on the mean circulation. These waves are too small at their excitation level in the troposphere to be resolved self-consistently by a model and therefore have to be parameterised. Furthermore, radiative processes in the middle atmosphere, such as the UV-light absorption or important cooling processes due to CO_2 emissions, need to be considered for the main gases (in particular O_2) and the important trace gases (H_2O , O_3 , CO_2). This must include non-LTE processes. In higher altitudes the molecular diffusion and ionospheric influences become important.

One example is the development of the HAMburg Model of the Neutral and Ionized Atmosphere (HAMMONIA, 2004), which extends from the earth's surface up to 250 km. The model combines physics and dynamics from former tropospheric and middle atmospheric models with an extensive chemical transport model. Special upper atmosphere processes as non-LTE effects in the infrared cooling or solar heating at very short wavelengths and ion drag are included as well. In order to parameterise gravity waves the Hines-scheme

(Hines, 1997a,b) is used. For example, simulations are intended to assess the sensitivity of the mesopause region to the 11-year solar cycle or the CO_2 doubling.

The extended Canadian Middle Atmosphere Model (CMAM) also now spans a range from the surface up to 210 km. It contains self-consistent comprehensive tropospheric physics and realistic parameterisation of the processes in the mesosphere/lower thermosphere (MLT) region such as the breaking gravity waves, solar heating and infrared cooling - also under non-LTE conditions, chemical heating, ion drag and diffusive processes. The rationale of the model is to examine the nature of the physical and dynamical processes in the MLT region without the artificial effects of an imposed sponge layer which was set before at ~ 95 km and therefore modified the circulation in an unrealistic manner (Fomichev et al., 2002).

Another GCM, focused on the middle atmosphere, is the Thermosphere Ionosphere Mesosphere Electrodynamics General Circulation Model (TIME-GCM, 2004) from NCAR (National Center of Atmospheric Research) in Boulder, Colorado. Its range of altitude coverage extends from 30-500 km, with the critical mesosphere/lower thermosphere region being in the centre of its numerical grid, allowing dynamical, chemical, radiative, and electro-dynamical couplings between the thermosphere and mesosphere to occur. However, tropospheric processes are neglected. This model has been used in a number of studies to analyse various ground- and satellite-based data from the middle atmosphere.

A GCM should provide a comprehensive simulation of the 3-D general circulation, if all processes are correctly presented. It is, however, rather difficult to study dynamical processes due to the complicated nature of separating the different contributions. Another disadvantage of such a model is its high time cost. Therefore, other models exist, which are simplified in different ways, depending on the purpose of the investigation.

Such a simplified model is the global scale wave model (GSWM). Hagan (2004) developed it to investigate in particular free travelling planetary waves and tides using the linearized and extended Navier-Stokes equations for steady-state global temperature and wind perturbation. The background atmosphere uses winds determined from measurements made by instruments onboard UARS (*Upper Atmosphere Research Satellite*). The GSWM background temperature and density are taken from the MSISE90 model. An enclosing radiation routine allows tidal excitations. Dissipation and diffusion processes due to gravity waves are parameterised. The model provides a useful tool for studying wave processes. However, its linearised set-up cannot account for non-linear interactions between waves and the mean flow.

A mechanistic model for the middle atmosphere for instance is in most cases a non-linear model but with the main focus on the dynamics and radiation schemes in the stratosphere, mesosphere and thermosphere. The troposphere in these cases is considered to be a lower boundary and is therefore only rarely described with a small resolution and without a hydrological cycle. The main advantage of such models is a rather quick calculation and therefore efficient study of dynamical processes. The models are especially useful for inves-

tigations into wave-wave and wave-mean flow interaction, since they allow the possibility of artificial forcing the waves from the lower boundary and to keep track their behaviour separately.

A version of COMMA (Cologne Model of the Middle Atmosphere), which is the basis of this work, is also used at the State University of St. Petersburg, at the Central Aerological Observatory Dolgoprudny (Moscow region) and at the IAP (Institute of Atmospheric Physics) in Kühlungsborn. The main components are the same and will be described in chapter 3 for COMMA-LIM. However, the different versions run for several reasons, for example COMMA-IAP uses a chemistry model to take into account photochemical reactions, particularly in the upper mesosphere and lower thermosphere. COMMA-IAP studies are focused on mesopause phenomena such as noctilucent clouds. Recently, the dynamical core has been changed and the model is now known as LIMA (Leibniz-Institute Middle Atmosphere model). At the Max-Planck-Institute for Aeronomy in Katlenburg-Lindau COMMA also serves a basis for developing a Martian atmosphere model.

The Leipzig COMMA version (COMMA-LIM) will be described in detail in chapter 3. This model focusses on investigations of atmospheric tides, gravity waves and planetary waves in the middle atmosphere. Chemical reactions are not considered in the calculations but radiative processes provide the necessary heating and cooling rates, which force the atmosphere throughout the year.

Chapter 2

2.1 Observation of the QTDW

The QTDW has been well documented over the last 30 years as a striking feature of the summer middle atmosphere. The very regular appearance in one or two bursts shortly after solstice raised the question about its origin. From the ground, radar techniques in particular provide continuous wind data at certain points around the earth while satellites deliver wind and temperature measurements as global pictures. Some of the important observations revealing the structure and characteristics of the QTDW will be presented here. One has to keep in mind that there are not only various methods of measuring wind and temperature but also different applications of data analysis. With increasing information on the wave the search for the origin of the wave has become dominant and has in turn influenced the theories.

2.1.1 Radar and satellite observations

Radars measuring the wind in the MLT region first detected the QTDW. The local measurements could give information about the wave's period together with amplitude and phase of wind. However, to make statements about the wave number and latitudinal behaviour the data had to be collected and compared. The vertical shape was poorly resolved because of the confined region a radar is able to measure. In the following section, the general wave properties are introduced and are listed in table(2.1.2).

First publications of the QTDW were made by Muller (1972). His analyses of time series of wind data showed an oscillation with a strong peak in July/August with a *period* of around 51 *h*. Kalchenko and Bulgakov (1973) reported on wind measurements at Mogadishu between 1968-1970, where a strong 2-day oscillation was found in early August 1969 for the meridional wind component dominating all other harmonics at this time. Later, analyses of radar data in Adelaide, Australia also revealed strongly increased disturbances during each January with a period of 48 *h* (Craig and Elford, 1981). Further reports showed that the period was often close to 48 *h* in the southern hemisphere, while

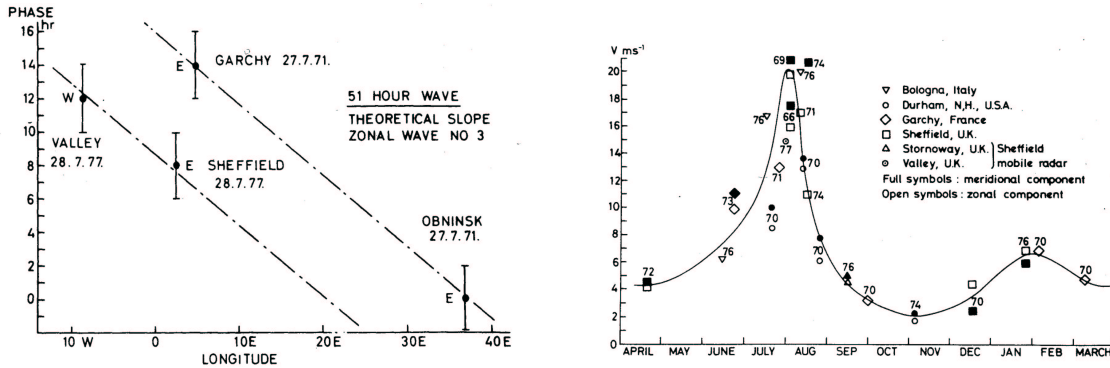


Figure 2.1: Left panel: The phase (time of maximum eastward velocity in UT) of the 51 h meteor wind oscillation as a function of longitude. Values relate to an average altitude of 95 km . Parallel lines indicate the expected phase variation for a westward travelling wave of zonal wave number 3. Right panel: The amplitude of 51 h meteor wind oscillation at various times of the year based on mid-latitude records during the period 1966-1977. Taken from Muller and Nelson (1978).

in the northern hemisphere periods of about 50 – 52.2 h were more frequently recorded. Jacobi et al. (1997) found that with increasing amplitudes the periods shortened, so that maximum amplitude values of more than 30 m s^{-1} corresponded to periods of about 48 h . However, wind data at other stations observed periods of about 46 h , as shown by Thayaparan et al. (1997).

A horizontal *wave number* and a direction of wave propagation could only be derived by making comparisons between different mid-latitudinal radar stations. In the northern hemisphere this oscillation proved to be a westward travelling planetary wave with a zonal wave number of 3 (Glass et al., 1975; Muller and Nelson, 1978). Other papers as that by Meek et al. (1996) reported a wave number 4. Clark et al. (1994) refused to give a determination of a zonal wave number because of the strong modulation of this wave during the observational time. Poole and Harris (1995) derived the zonal wave number in the southern hemisphere. The values differed for the zonal and meridional wind fields, where the meridional component showed wave numbers below the integer value of $k = 3$ with a mean of 2.74 ± 0.07 and the zonal component yielded $k \geq 3$. By accepting the results of non-integer wave numbers at face value, the authors discussed the possibility of two co-existing modes with the same period but different k . Such a superposition would lead to an oscillation that is sinusoidal at a particular longitude but distorted zonally by modulation as one mode overtakes the other. Similar processes can be expected for the northern hemisphere as well. Satellite observations confirmed the analyses of the wave number of being either 3 as well as 4, in depending of strength of the amplitude (e.g. Wu et al. (1996)).

A remarkable feature of the QTDW is its dominating *amplitude* in the meridional wind field, particularly at low latitudes. Zonal (u') and meridional (v') wind disturbances be-

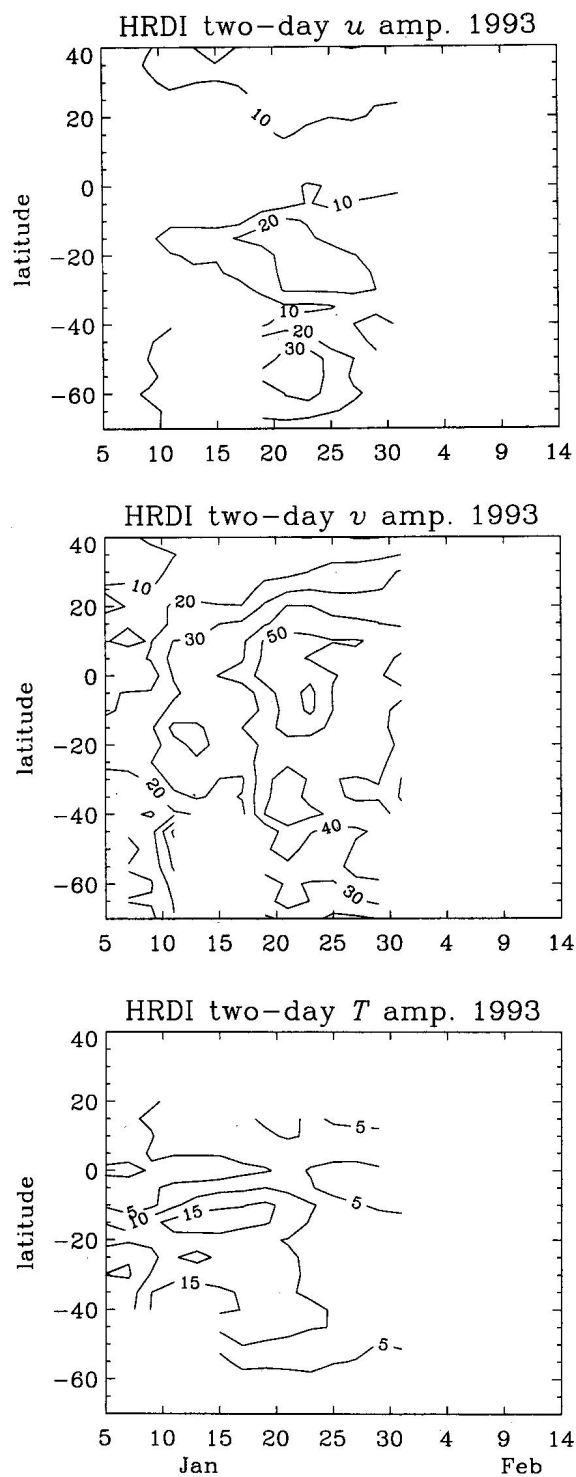


Figure 2.2: The QTDW as observed by the UARS for (top) zonal, (middle) meridional and (bottom) temperature fits at 95 km from January 5 to February 14, 1992. Fits are for sliding 4-day estimates. Taken from Fritts et al. (1999).

come comparable with increasing latitude. Such behaviour, i.e. maximum meridional wind disturbance at the equator where the zonal wind oscillation shows a minimum, is typical for a Rossby-gravity wave. Further results comparing Kyoto and Adelaide radar data (Tsuda et al., 1988) show the east-west(EW) and north-south (NS) wind in out-of-phase and in-phase behaviour, respectively. This pointed again to a manifestation of an asymmetric normal mode. However, amplitudes are differently characterised in the northern and southern hemisphere. Meridional wind amplitudes were found up to 20 m s^{-1} (Gurubaran et al., 2001) in the northern tropics as well as at 52°N (Jacobi et al., 1997), while Craig and Elford (1981) and Plumb et al. (1987) reported speeds of between $40 - 50 \text{ m s}^{-1}$ for Australia. Northern subtropical stations are able to detect the January QTDW as well even though the amplitudes are strongly reduced (Tsuda et al., 1988). The wave extension is thus predominant in the summer hemisphere. Satellite observations during January 1992 (Wu et al., 1993) gave up to 60 m s^{-1} for v' at the equator, while the zonal component was observed with 30 m s^{-1} at low to middle latitudes in the southern hemisphere. Fig.(2.2) shows an example of a developing QTDW during January 1993. Fritts et al. (1999) observed a relatively sudden onset of the wave with a large response in the meridional wind field. The latitudinal and temporal behaviour for wind and temperature disturbance fields clearly shows the equatorial maximum of v' , while u' and T' have their maxima at lower and mid latitudes.

Primarily satellites detected amplitudes of *temperature* disturbances. The first report using *Nimbus 7* data came from Rodger and Prata (1981). The global picture of the temperature field shows an asymmetric behaviour with a large peak at tropical latitudes of the summer hemisphere. However, the obtained absolute values were very small ($< 1 \text{ K}$). Wu et al. (1996) used the *Upper Atmosphere Research Satellite* (UARS) for wave event studies. The authors found stronger temperature peaks during southern summers with maximum values up to 7 K , while during July/August the temperature amplitudes of the QTDW only reached values of up to 2 K for the wave number $k = 3$ and 4.5 K for $k = 4$.

Quite ambiguous features of the QTDW are the *vertical wavelength* and the *phase behaviour*. A small phase tilt with height in the meridional oscillation was found by Craig and Elford (1981) which led to the conclusion of downward phase propagation with a vertical wavelength of about $200 - 400 \text{ km}$. The result was confirmed by Wu et al. (1993). This feature is expected for a free travelling planetary wave. The vertical wavelength observed in Canada (Thayaparan et al., 1997) showed a different behaviour; during strong 2-day wave events the wavelength exceeded 150 km whereas at other times the wavelength was shorter at about $60 - 80 \text{ km}$. Also Gurubaran et al. (2001) found at times structures that revealed wavelengths between 35 and 70 km , while at other times evanescent modes with more than 100 km were recorded. Both increasing and decreasing phases with height as well as very little variation in phase were observed. It was suggested that these different results could be explained by reflection of upward propagating waves at temperature inversion layers and subsequent interference. The phase profile would then show an increasing or decreasing trend corresponding to the strength of one of the two waves. As a further interesting detail a phase locking behaviour of the QTDW at a preferred local time was

reported by Craig and Elford (1981), Thayaparan et al. (1997), Jacobi et al. (1997) and Clark et al. (1994).

2.1.2 Further studies

Since the observations gave no unique picture of the QTDW, studies were extended on searching for possible excitation or amplification mechanism. Investigations into interaction with other waves, latitudinal or vertical propagation of the QTDW or simultaneously occurring wind changes were carried out in order to see whether they could serve as explanation for the burst-like appearance of the wave in summer.

Interaction with the mean flow

Plumb et al. (1987) investigated the QTDW-event in southern summer 1983/1984 and its possible impact on the mean flow at mesospheric heights. A dramatic reverse in the zonal wind at 86 km altitude just at the onset of the wave pulse seemed to point to a response of the background circulation. Using a very basic approximation of the quasi-geostrophic momentum budget of the zonal flow it was shown that a wave pulse similar to the observed 2-day wave at Adelaide with huge meridional wind amplitude is qualitatively capable of inducing a change in the mean flow on a remarkable scale.

Tidal interaction

Several authors reported on a tendency of the QTDW to be locked in phase relative to the local time around noon, e.g. Craig and Elford (1981); Clark et al. (1994); Jacobi et al. (1997)). So this feature is present in both hemispheres. They suggested that these preferred phase values might indicate some solar influence on the 2-day wave, possibly through interaction with the solar tides. Therefore, Thayaparan et al. (1997) examined the relationship between the tides and the QTDW. The mean phase of strong QTDW amplitudes was found to occur quite regularly at $\sim 12 h$ local time in the analysed data set. However, amplitudes of possible secondary waves arising from interaction between tides and QTDW, gave only small values.

The study of Gurubaran et al. (2001) on the simultaneous occurrence of diurnal tide (DT) during wave events showed a clear anti-correlation of QTDW and DT for the year 1995. Increased QTDW activity was almost always accompanied by a weak diurnal tide and vice versa. A 16-*h* oscillation was believed to be generated as a secondary wave from the interaction between DT and QTDW. However, the year 1996 did not show such a clear relationship for the three wave parameters.

Planetary wave interaction

UK Meteorological Office (UKMO) stratospheric analyses and UARS measurements were investigated at the tropical stratopause with a focus on inertial circulations and 2-day waves (Orsolini et al., 1997). The UKMO data suggested a special coupling mechanism through planetary wave activity in the winter hemisphere leading to the amplification of the QTDW. It was argued that the onset of strong inertial disturbances was associated

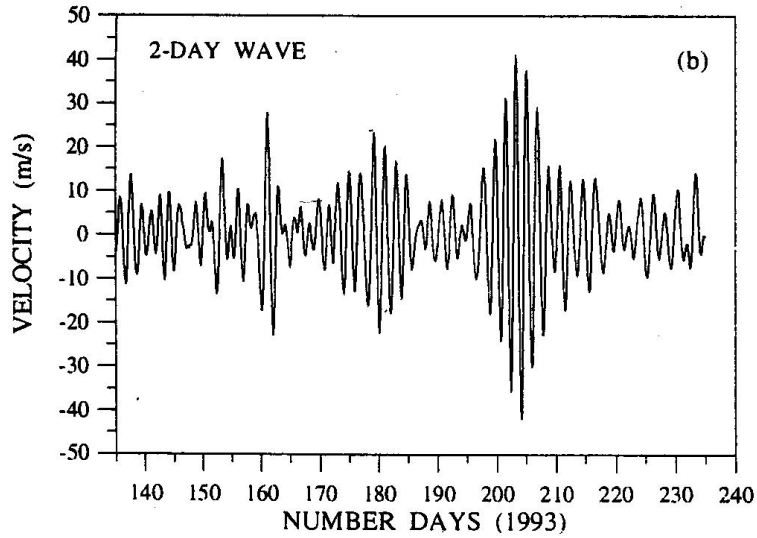


Figure 2.3: Meridional winds obtained by a meteor radar band-pass filtered between period limit of 40 – 58 hours for NH-summer days in 1993. Taken from Pancheva et al. (2000).

with a weakened westward jet due to deposition of westerly momentum near the equator. This in turn can contribute to an increase in the horizontal curvature of zonal mean zonal wind and can lead to a negative meridional gradient of \bar{q} . These conditions were suggested to be favourable, if not sufficient, to the onset of a QTDW. Then, they could also explain the stronger QTDW in the southern hemisphere due to stronger planetary wave activity in the northern hemisphere.

Since the QTDW was observed in most cases as a burst with a length of between two weeks and one month, Jacobi et al. (1998) analysed the 14-year data set of summer Collm-winds with respect to correlations between the 2-day wave and other planetary waves. For some cases non-linear interaction was found to be responsible. Expected secondary waves resulting from non-linear interaction with the 16-day wave (16DW) and 10-day wave (10DW) were found as well. However, the correlation between the secondary waves and 16DW was rather weak and could not be the only process responsible for periodic variations of the QTDW. In some years the wave was found to be divided into two frequencies, which could result from self-interaction of the QTDW during its appearance.

Pancheva et al. (2000) reported on possible non-linear interactions of the QTDW with the 10DW, 16DW and tides for the years 1992 and 1993 (see for instance, Fig.(2.3)). Interaction between the QTDW and 10DW was found to appear in both summers, whereas a strong signal of interaction with the 16DW only occurred in 1992. Nevertheless, the QTDW was involved in many planetary-wave interactions during summer and the splitting up into periods of 1.7 and 2.1 days was assumed to be related to this phenomenon.

Gravity wave interaction

Another interesting feature of the QTDW was reported by Herman et al. (1999). The MF radar wind data ($40^{\circ}\text{N}, 88^{\circ}\text{W}$) of 2-day wave events in July/August 1991 was used to investigate the interaction of gravity waves (GW) and the QTDW. The variance of the obtained zonal and meridional winds was assumed to represent gravity wave activity, and standard deviation is simply the square root of the variance. A composite analysis of both the mean wind components and their related standard deviations gave results suggesting that GW-activity in higher altitudes was controlled by QTDW-activity in levels below.

Manson et al. (2003) studied the modulation of gravity waves by planetary waves (PWs), in particular the QTDW. Based upon a simple model of gravity wave saturation, GW variances should maximise when the PW has its maximum eastward/westward perturbation in the winter/summer season, respectively. Therefore, the phase differences between the PW oscillation in the wind and GW sequences should be in-phase (0°) in winter and out-of-phase (180°) in summer. During the summer of 1994 several bursts of modulation of the GW variances by a 2-day wave activity were found for two bands ($10 - 100 \text{ min}$, $2 - 6 \text{ h}$). The phase differences between the QTDW and the corresponding modulations of the GW variances were generally close to 180° for both zonal and meridional components. These phase relations are consistent with GW propagation into the northeast quadrant.

Solar variability

Jacobi et al. (1997) analysed the years 1982-1995 searching for inter-annual variability of the QTDW. Stronger wave amplitudes were found during solar maximum conditions.

Latitudinal propagation

The time series of UARS at 95 km during 1992 and 1993 (Wu et al., 1993) showed that the QTDW appeared first at higher summer latitudes before it progressed to middle and low latitudes. Therefore, the authors suggested that a triggering of the wave was due to baroclinic instabilities at higher summer latitudes. This oscillation then disperses into global response with an Eigenmode structure.

Temperature data for the same time period showed a precursory wave coming from the winter hemisphere before the onset of the southern QTDW for the month of January (Wu et al., 1996). It was suggested that planetary wave activity in the winter hemisphere triggers the growth of the 2-day wave. During July/August the temperature amplitudes of the QTDW only reached values of up to 2 K for the wave number $k = 3$ and 4.5 K for the wave number $k = 4$. And in turn no precursors or connections between winter and summer waves were found at this time. The conclusions drawn from the analysis were that the characteristics of the QTDW present a mixture of two types of waves and can only be interpreted as a presence of both normal and unstable modes.

A combined study using satellite and radar was carried out in northern summer in 1996. Three radars from the Super Dual Auroral Radar Network (SuperDARN) at northern mid-latitudes compared their July wind data with UARS wind measurements (Bristow et al.,

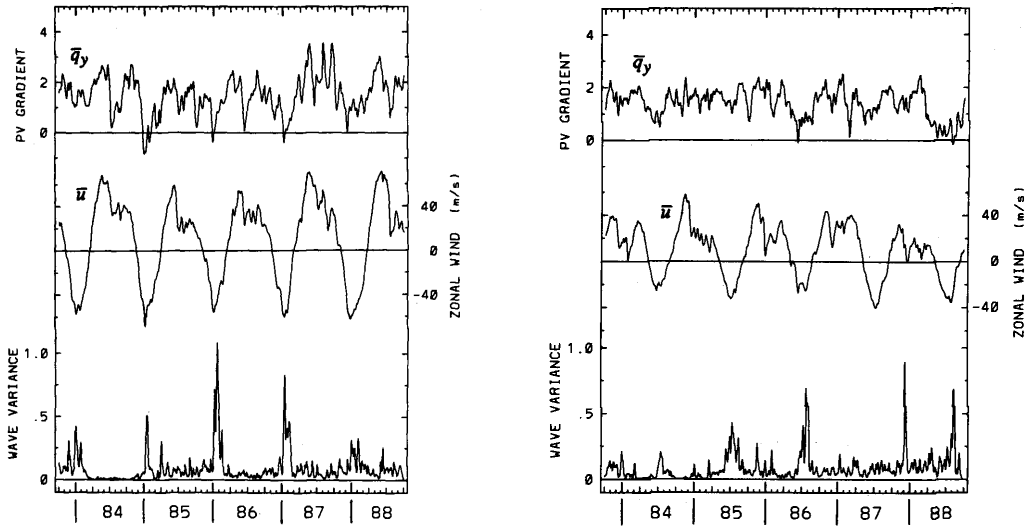


Figure 2.4: A synoptic view of \bar{q}_y ($10^{-1} m^{-1} s^{-1}$), \bar{u} ($m s^{-1}$) and 2-day wave variance for $20^\circ S$ (left) and $20^\circ N$ (right) at $1 mb$. Taken from Randel (1994).

1999). The main disadvantage of the comparison of the two data sets was the different time sequences: while the satellite measured MLT winds from July 10-16, significant QTDW amplitudes in the radars were observed from July 15-21. However, the satellite showed an evolving wave at equatorial latitudes on July 14 and it was therefore suggested, that the wave was originated at low latitudes and propagated to high latitudes with about a 1-day delay.

Unstable stages of the atmosphere

Daily operational stratospheric analyses produced at the National Meteorological Center (NMC) - covering the period of October 1983 to September 1988 - served as a basis for space-time cross-spectral analyses (Randel, 1994). The considered region ranges from approximately 20 to 50 km. Indeed, well-pronounced signals of QTDW events were found. In Fig.(2.4) two-day wave variance in temperature for both wave numbers 3 and 4, derived zonal mean zonal wind \bar{u} from geopotential height data and the meridional gradient of quasi-geostrophic potential vorticity \bar{q}_y were considered together for $20^\circ S$ and $20^\circ N$, respectively. The wave was recognised as a very transient but regularly arising phenomenon following solstice conditions. Furthermore, it turned out that the strongest bursts of QTDW occurred when \bar{u} showed the most intense easterlies and $\bar{q}_y < 0$ although there were also QTDW events with positive \bar{q}_y . It was suggested that in the latter cases the meridional gradient of potential vorticity was negative in uppermost layers. Stronger "southern" waves were connected with stronger easterlies and deeper minima for \bar{q}_y . Latitudinal-height cross-sections showed wave maxima at the highest levels extending from $\sim 10^\circ$ in the winter hemisphere to $\sim 50^\circ$ in the summer hemisphere. The vertical and meridional structures of the QTDW observed in this data provoked again the idea that combined resonant and

Table 2.1: Overview of remarkable observations of the QTDW. Note, that abbreviations NH and SH are used for northern hemisphere and southern hemisphere, respectively.

Zonal wave number	Period, [h]	Maximum u' , [$m s^{-1}$]	Maximum v' , [$m s^{-1}$]	Maximum T' , [K]	vertical Wavelength, [km]	Phase propagation	Time of observation	Location	Instrument	Reference
	51							53°N, 1.5°W	radar	Muller (1972)
	48	7.4	23.4				8/1969	2°N, 45°E	radar	Kalchenko and Bulgakov (1973)
3	51							NH	radar	Glass et al. (1975)
	~ 48						8/1976	52°N, 107°W	radar	Stening et al. (1978)
	4 53	> 25	> 40		200-400	downward	1/1966-1/1975	35°S, 138°E	radar	Craig and Elford (1981)
3	48						1973-1977	global	satellite	Rodger and Prata (1981)
4	~ 40						1973-1977	global	satellite	Rodger and Prata (1981)
	52-55	10 – 15	10 – 15		> 100	downward	1/1984	35°N, 136°E	radar	Tsuda et al. (1988)
	48	small 15 – 20	30 – 35		> 100	downward	1/1984	35°S, 138°E	radar	Tsuda et al. (1988)
3		30	60			downward	January 1992/1993		satellite	Wu et al. (1993)
	49-51	~ 15	~ 30				10/1990-8/1992	22°N, 160°W	radar	Fritts and Isler (1994)
							July/August			
	48	~ 25	~ 30				10/1990-8/1992	22°N, 160°W		
							January/February			
3?	48	28					1980-1983	NH	radar	Clark et al. (1994)
2-4								SH	radar	Poole and Harris (1995)
4	48	10 – 20	25 – 45		~ 80		1992	NH	radar	Meek et al. (1996)
3	48	25 – 30	~ 40		80	downward	1/1993	SH	satellite	Ward et al. (1996)
3	48			7			11/1992-9/1993	SH	satellite	Wu et al. (1996)
4	45.3			1.5						
3				2				NH		
4				4.5						
	46	15 – 20	25 – 30		60 – 80, > 150	downward	1993/1994	43°N, 81°W	radar	Thayaparan et al. (1997)
	48-50		20-30				1982-1995	52°N, 15°E	D1 radio waves	Jacobi et al. (1997)
3		25	25				7/1996	NH	radar	Bristow et al. (1999)
3	48	10-20	30-50		50 – 80, > 100		January	SH	radar and satellite	Fritts et al. (1999)
							1992/93/94			
3	48						1991-1994	global	satellite	Limpasuvan et al. (2000)
4	~ 44									
	48	10 – 15	30		35 – 70, > 100	upward and downward	winter	8.7°N, 77.8°E	radar	Gurubaran et al. (2001)
							1999			
	52	10 – 15	20		35 – 70, > 100	upward and downward	summer			
							1999			

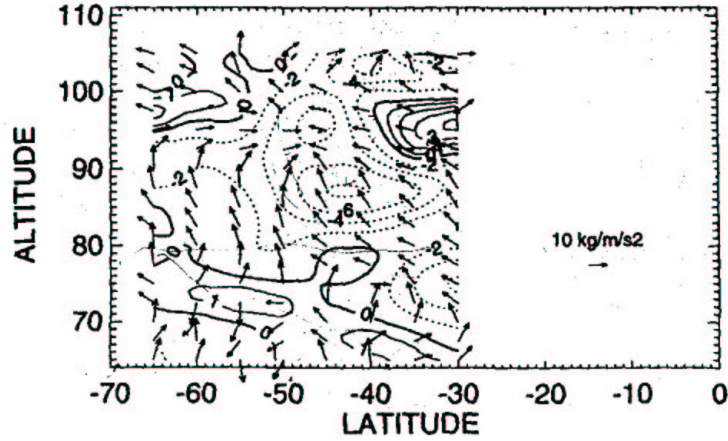


Figure 2.5: Eliassen-Palm flux vectors and contours of EP flux divergence per unit mass. Values are calculated from the sum of wave numbers 2-4 retrieved at quasi 2-day periods, averaged over the period 14-25 January 1994. The vertical component is scaled by 3500; all vectors have been subsequently normalised to a value of 10. Contour interval is $2 m s^{-1} day^{-1}$. Taken from Liebermann (1999).

unstable modes excite this oscillation.

The focus of the work by Liebermann (1999) was to bring more understanding to the wave-mean flow interaction during a 2-day wave event. UARS wind and temperature measurements from January 1994 were used not only to show the wave morphology but also to derive the vector components of the Eliassen-Palm (EP) flux \mathbf{F} . A combination of wave numbers 2-4 which showed a response at a period of ~ 2 days were analysed and the divergence of EP flux per unit mass was obtained on the order of $-5 m s^{-1} d^{-1}$ in the MLT region indicating westward forcing there (see Fig.(2.5)). The vertical convergence of meridional heat flux $\partial F^z / \partial z$ was found to be the dominating term. It was claimed that the positive region of EP-divergence in the mesosphere below and a spatial coincidence of negative \bar{q}_ϕ (not shown) implied a role of instability as a source of a 2-day wave. A response of the zonal mean wind and temperature on the QTDW using a linear quasi-geostrophic model of the TEM circulation (Garcia, 1987) was calculated. The results gave a weak equatorward flow together with westward winds on the order of $20 m s^{-1}$. Baroclinic instability was suggested to be the key process for the QTDW event in 1994.

Fritts et al. (1999) combined radar and satellite measurements for three southern hemisphere summers (1992-1994) in order to derive meridional heat ($\overline{v'T'}$) and momentum fluxes ($\overline{u'v'}$) for QTDW events. Meridional gradients of the flux of zonal momentum were found to be anticorrelated with the low-pass zonal motion which was connected with the two-day wave. Despite the large year-to-year variability of the QTDW, the structures showed some consistency with a broad latitude band from $\sim 0^\circ$ to $30^\circ S$ of negative meridional flux of zonal momentum. The meridional fluxes of heat precede the meridional fluxes of momen-

tum by $\sim 5 - 10$ days. This was explained by earlier arising 2-day wave temperature disturbances before the onset of wave velocity perturbations. These calculated fluxes were suggested to be reasonable approximations of the (measurable) influences of the QTDW on its environment. Nevertheless, by determining terms of the Transformed Eulerian-Mean equations, it was found that the responses in the zonal mean circulation were smaller than expected. A suggested explanation for this discrepancy was that the generation of meridional motions yielded to compensating Coriolis torques or to balancing vertical momentum fluxes which themselves could not be determined. Investigations into instability conditions led to the discovery of important information on baroclinic instability which was claimed to be an evidential source of the QTDW-motion.

The aim of Limpasuvan et al. (2000) was also to analyse the background conditions in order to find answers to the question of its origin. For this purpose temperature data sets recorded by UARS were used from 1991-1994. The height range was limited to upper stratosphere/stratopause regions. In all summers the QTDW appeared with both zonal wave numbers 3 and 4. For the southern summers the variation in relative strength of the westward jet appeared to play a role for the dominant wave number (weaker jet favours wave number 4 and stronger jet favours wave number 3). The searching for instability conditions during or before QTDW events revealed in some cases the occurrence of negative \bar{q}_ϕ together with wave number 3 and 4 temperature amplification. However, this behaviour was not consistently found; barotropic instability interpretation could be applied to southern hemisphere summer 1992/1993 but not to 1993/1994. For northern hemisphere summers baroclinic instability seemed to be the process most likely to trigger a QTDW, predominantly for the wave number 4. In addition, some normal-mode characteristics pointed again to the ambiguity of this phenomenon.

2.2 Theory and model results

2.2.1 Normal mode studies

Based on the first observations in the seventies (e.g. by Muller (1972), Glass et al. (1975), Muller and Nelson (1978)) Salby (1981) investigated the recurrent phenomenon of the QTDW as a possible resonant Eigenmode of the earth's atmosphere. The oscillation suggested the identification with the third Rossby-gravity normal mode in a windless isothermal atmosphere. These modes correspond to solutions of Laplace's tidal equation with a 10 km equivalent depth and a vertical structure of a Lamb wave. The investigation focussed on the sensitivity of wave in relation to the different mean fields in wind and temperature, such as equinox and solstice conditions. The Rossby-gravity mode obtained for an isothermal atmosphere was included in a global model of linearised primitive equations with Newton cooling and linear diffusion. The imposed surface forcing was varied through one of the Eigenfrequencies, in order to find the resonant response and the corresponding normal mode structure. Solutions showed some clear peaks for equinox (~ 2.27

days) and solstice (~ 2.22 days). Wave amplitudes in wind and temperature calculated for summer conditions showed an impressive coincidence with observations (see Fig.(2.6)). The meridional wind maximised at the equator and extended its amplitude at higher levels into summer mid-latitudes, whereas zonal wind and temperature revealed nodes at the equator and maxima also at mesospheric summer mid-latitudes. Under equinox conditions the wave was confined to lower scale heights (~ 45 km) due to prevailing westerlies in the middle atmosphere.

2.2.2 Instability studies

The theory of the QTDW being an Eigenmode of the atmosphere covers many features of the wave, however it cannot explain its burst-like behaviour. An Eigenmode should be present all the time and its dependence on the mean wind structure was not considered to be a sufficient explication.

Therefore, Plumb (1983a) suggested an alternative explanation concerning the origin of the QTDW. Since strong wind gradients exist during solstice conditions in the summer mesosphere the possibility of an unstable developing QTDW was proved. A one-dimensional instability analysis was applied on a β -plane in the middle atmosphere to find the growing modes. The perturbation potential vorticity equation was similar to that already used in (1.27) but with diabatic heating

$$\left(\frac{\partial}{\partial t} + \bar{u} \frac{\partial}{\partial x}\right) q' + \frac{\partial \bar{q}}{\partial y} \frac{\partial \psi'}{\partial x} = -\frac{f^2}{\rho} \frac{\partial}{\partial z} \left(\frac{\rho \alpha}{N^2} \frac{\partial \Psi}{\partial z}\right) \quad (2.1)$$

where α is the Newtonian cooling rate; q' and $\partial \bar{q}/\partial y$ are defined as in (1.28) and (1.29). Solutions were sought in the form

$$\psi'(x, y, z, t) = \text{Re} \Psi(z) e^{ik(x-ct)} \sin(ly), \quad (2.2)$$

and inserted in (2.1) under appropriate boundary conditions. A prescribed vertical wind structure simulated a strong westward jet in the middle atmosphere. The vertical wind structure itself was subject of several investigations including the strength of the shear and the height of the jet core. Together with suitable temperature stratification (represented in N^2) a region of negative meridional gradient of quasi-geostrophic potential vorticity was modelled providing the necessary condition for instability. From the modes of instability found, one rapidly growing wave was detected which had a zonal wavelength of ~ 10000 km and a westward phase velocity of ~ 60 m s⁻¹. For a "mid-latitude" calculation this corresponded to a wave number-3 wave with a period of around 2 days. The mode was associated with the mesospheric occurrence of a negative $\partial \bar{q}/\partial y$. The vertical shear in the mesospheric wind exceeded in this case 6 m s⁻¹ km⁻¹.

A two-dimensional instability analysis for the westward jet in the summer mesosphere was performed by Pfister (1985). Several jet structures were prescribed, ranging from

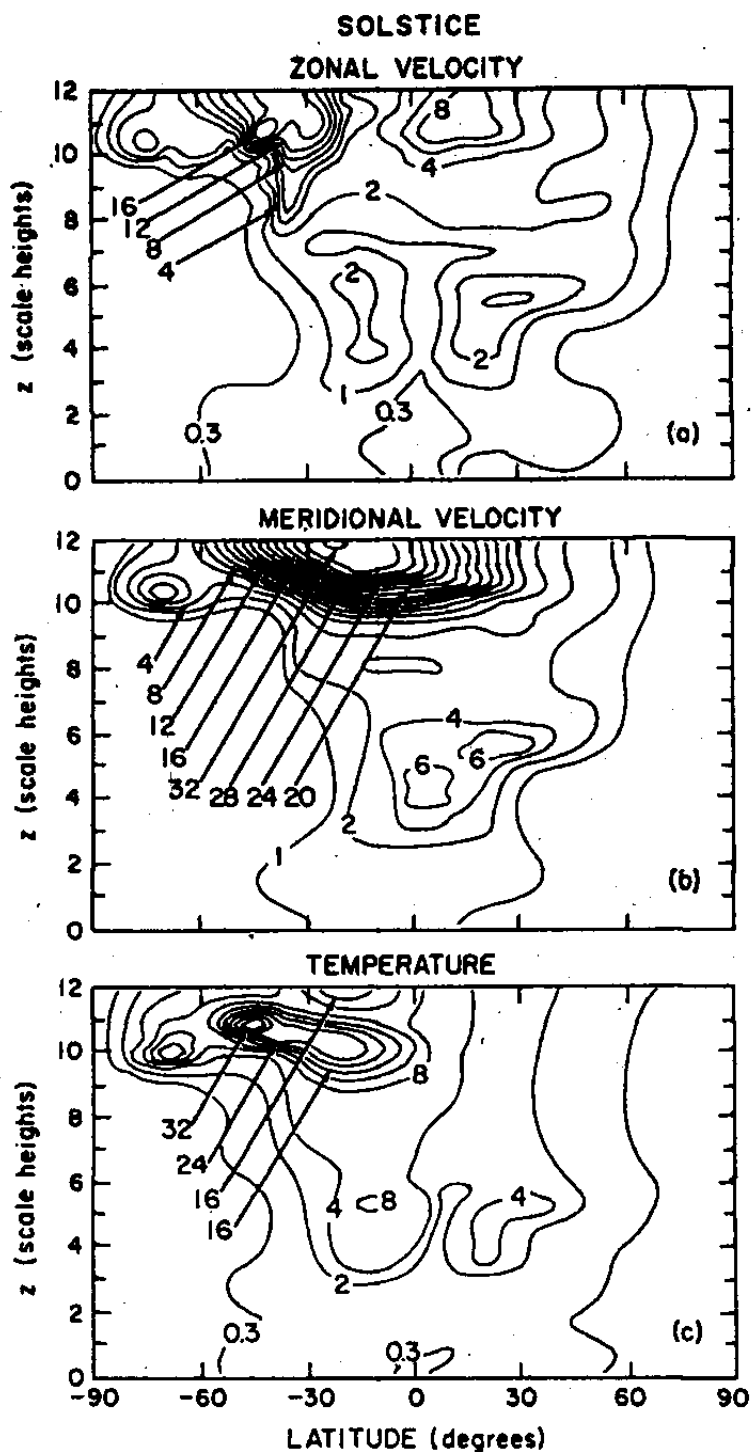


Figure 2.6: Disturbance fields for the third Rossby-gravity mode in solstice: (a) zonal velocity, (b) meridional velocity, both normalised by the maximum "zonal" velocity at the surface; (c) temperature. Taken from Salby (1981).

strongly unstable to weakly unstable profiles, varying the altitude of the jet core as well as the tightness and slope. Contributions of barotropic and baroclinic terms to the negative $\partial\bar{q}/\partial y$ for all profiles were investigated and the baroclinic term was identified as the dominating one. The baroclinically unstable waves found in this study were strongly trapped in the middle and high latitudes and therefore not able to account for a planetary wave maximising in geopotential at around 30° like the QTDW. An obvious shortcoming was the quasi-geostrophic approximation of this topic. Inclusion of thermal damping did not significantly influence the structure of the obtained wave but reduced the wave growth rates.

Further studies on an excitation of the QTDW due to instabilities were carried out by Limpasuvan (1998). His work concentrated on inertial instability processes, which can take place if an imbalance arises between pressure gradient force and centrifugal force. The numerical results simulating inertial instability conditions showed in fact a developing 2-day wave at stratopausal heights, amplifying first as wave number 4 mode followed by a $k = 3$ mode. Note, that the wave developed in this model despite the fact that Rayleigh friction instead of a gravity wave parameterisation was applied.

Exciting the QTDW via instability processes was also the aim of Merzlyakov and Jacobi (2004). In order to generate unstable summer conditions, an additional mean zonal forcing term was inserted near the westward jet core of a simple 3-D non-linear model. As the mean zonal wind reached $\sim -80 \text{ m s}^{-1}$, a well pronounced wave developed with the properties of a QTDW, a zonal wave number 3 wave with a period of 52.7 *h*. The amplitude of the oscillation for the meridional wind showed the characteristic extension from equatorial stratosphere/mesosphere to mid/high latitude mesosphere. The amplitude's maximum in meridional wind peaked at about 20 m s^{-1} . With increasing summer jets the amplitudes grew up to 80 m s^{-1} , while the periods shortened to 51.5 *h*.

The PhD-thesis by Schröder (2003) was concentrated on coupled barotropic-inertial instability as a mechanism for the excitation of planetary waves, in particular the QTDW, in the lower mesosphere. A horizontal 2-D spectral model was developed and applied to mesospheric levels for instability analyses. The background wind was obtained from observational data and typical wind profiles were extracted which are able to excite barotropic as well as inertial instability. The studies showed that an important factor of necessary instability conditions turned out to be not only the absolute value of negative $\partial\bar{q}/\partial y$ but also its relatively wide meridional extension. In such cases 2-day waves appeared in the calculations showing good accordance with the well-known properties of the QTDW. However, this behaviour was only obtained for December/January conditions.

2.2.3 Coupling of Eigenmode and instability

The idea of a coupling between Eigenmode structure and instability led Salby and Callaghan (2000) to use their model (Salby, 1981) to calculate the normal modes in a new way. Complex frequencies allowed the modes not only to become neutral but they

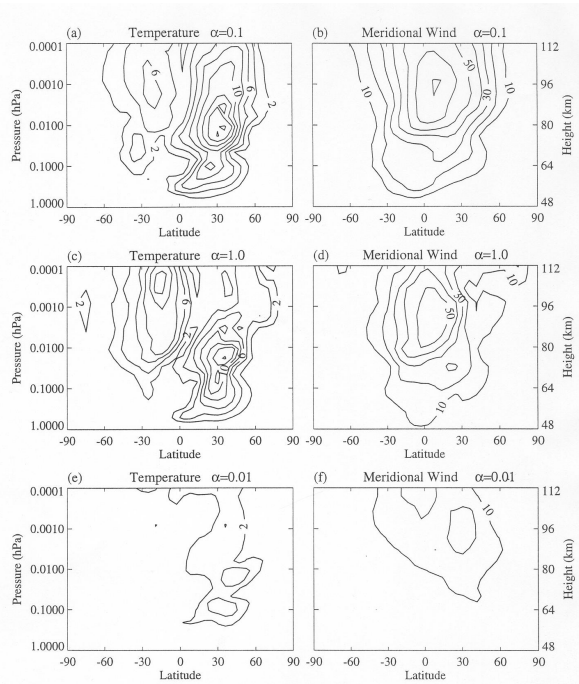


Figure 2.7: UGAMP results of amplitude of the 2-day wave under different gravity wave parameters (α). Note that the lower boundary is at 48 km. Taken from Norton and Thuburn (1996).

also were able to account for unstable interaction with the zonal mean flow. Under solstitial conditions the wave amplified even in the troposphere. In the middle atmosphere structures pointed to baroclinic instability processes. In addition, a joint appearance of planetary wave activity in the winter hemisphere was found, whose transient behaviour in particular was thought to trigger the amplification of the QTDW. However, the absolute values of amplitudes in the wind and temperature fields exceeded the observed ones by a factor of ~ 10 .

2.2.4 Self-consistent excitation

The QTDW was accidentally discovered in a general circulation model for the middle atmosphere by Hunt (1981). The model did not include any diurnal cycle for radiation processes and neither orography nor a hydrological cycle at surface. By running it for perpetual January conditions a very clear 2-day signal in the meridional wind was recognised showing the strongest values of about 10 m s^{-1} at around 60°S . The oscillation was identified as westward travelling with a zonal wave number of 3. The wave had a small phase variation with altitude, and did not show any sign of baroclinic instability except for a region near 70 km . Even if not all results compared very well with observations it could be stated that

the exclusion of the diurnal cycle indicated that tides do not necessarily pave the way for a developing 2-day wave. The same applied for the omission of orography and hydrological cycle.

Norton and Thuburn (1996) showed QTDW properties as coming from barotropic-baroclinic instability processes. The UGAMP GCM (UK Universities Global Atmospheric Modelling Programme Global Circulation Model) exhibit clear 2-day wave structures with both wave number 3 and 4. While looking for the meridional gradient of \bar{q} , the model gave negative $\partial\bar{q}/\partial y$ in coincidence with positive divergence of Eliassen-Palm flux which is an expected pattern for instability. An important point of the work was that the wave was strongly connected with the gravity wave drag parameterisation. No QTDW was observed using Rayleigh friction instead of a gravity wave scheme because of an altered mean circulation. Even a change in the scheme leading to more gentle wave breaking reduced the amplitude of the 2-day wave by approximately a factor of two. A much more extended study on this topic was published by Norton and Thuburn (1999). There the simulations for northern summer were performed with three different strong parameters causing the gravity waves (GW) to break (compare with Fig.(2.7)). Due to the impacts on the wind and temperature fields it was stated that GWs are responsible for the changes in stability of the zonal mean state, making it more or less susceptible of barotropic and/or baroclinic instability.

In another study Salby and Callaghan (2003) investigated the assumption of planetary wave activity being able to excite a two-day wave. For this purpose stochastic fluctuations characterising tropospheric planetary wave structures were imposed at the lower boundary in the winter hemisphere of a 3D primitive-equation model. After 50 days of calculation the random fluctuations in the wave number-3 component gave a monotonically amplifying signal reaching maximum values after 100 days. Frequency analysis showed a strong peak at periods of 2.0-2.3 days indicating a westward propagating wave, even in the absence of instability. The wave structure itself resembled the Rossby-gravity mode obtained from Salby's model. However, the results have to be interpreted carefully because a rapid amplification, which is characteristic of a QTDW-event could not be shown within this approximation.

2.2.5 Model studies

Palo et al. (1999) were interested in the effects the QTDW can have on the middle atmosphere, in particular its ability to excite secondary waves. The 2-day wave was forced in the TIME-GCM at the lower boundary ($\sim 35\text{ km}$) under January conditions, together with tidal amplitudes and phases obtained from the GSWM. Analysed frequency-wave number spectra revealed a large number of secondary and tertiary waves, which were generated from the interaction between tides and the QTDW. The 16 h and 9.6 h oscillations, referring to interaction with the DT and the SDT, respectively, showed strong responses. Tidal amplitudes decreased down to 50% for the diurnal tide and 40% for the semidiurnal tide.

2.3 Summary and open questions

This overview has shown, that the QTDW can be observed and analysed with strong amplitudes shortly after solstice in the respective summer hemisphere, while during the rest of the year the wave shows only small amplitudes. The meridional wind field has its maximum above the equator but propagates well into mid latitudes in mesospheric regions. Fields of zonal wind, temperature and geopotential exhibit a node at equator and two maxima in mid latitudes, again with pronounced propagation conditions for the summer hemisphere. As a result, the ratio of zonal to meridional wind grows from 0.5 at the equator to nearly unity at middle latitudes. The amplitudes in all fields for the southern hemisphere events are approximately twice as high as those for the northern hemisphere.

Not only zonal wave number 3 was observed but also $k = 4$ and the wave period appears to be shorter for the higher wave number. Another interesting feature is the decreased period when the amplitude values are increased. The phase behaviour of the QTDW was found to be quite ambiguous. Almost no phase tilt with height was reported as well as increasing and decreasing phase tilts with height. Some observations reported on phase locking behaviour to the tides. Further considerations of interaction between tides and the QTDW found weaker diurnal tide amplitudes during strong QTDW events. Wind reversals were found together with the onset of a QTDW event. In connection with the appearance of the wave a high wind shear in the easterlies and a negative meridional gradient of potential vorticity was often observed.

When looking for mechanisms of origin the Rossby-gravity wave mode (3,0) as a solution of Laplace's tidal equations agrees in many cases with observations but cannot cover all observed features of the QTDW, in particular the burst-like occurrence in summer. Therefore, several kinds of instability processes - inertial, barotropic and baroclinic - were subject of theoretical investigations and data analysis. Conditions of instability were often found to arise at the same time as the QTDW amplifies. But again, no definite answer could be derived. In some years barotropic instability in the southern hemisphere and baroclinic instability in the northern hemisphere was found, or coupled inertial-barotropic instability was found, however for some years no such process was found yet the QTDW was present. The shortcoming of some instability studies was that they were based on inserted, unstable wind fields, either obtained from observational data or introduced by hand. Some unstable modes took to develop more than 50 days, although a quick reaction of the atmosphere is expected.

It has to be noted that only a few general circulation models showed the QTDW arising self-consistently from the model design; most of them investigated the wave as being forced from the surface as an Eigenmode.

A further conclusion made from the generation of unstable waves with different model approaches is that a developing mesospheric instability does not necessarily need a troposphere, but sufficient strong summer jets and the occurrence of a negative meridional gradient of potential vorticity are required. However, upward propagating tropospheric

disturbances such as, for instance, gravity waves may be responsible for a development of horizontal or vertical gradients in the zonal mean flow, particularly for short timescales.

Thus, the large amount of studies on the origin of the QTDW revealed many details but until now a complete description of the wave is missing. Furthermore, the knowledge about the interactions of the QTDW with other disturbances in the middle atmosphere is still sparse. However, only with enclosing information on all potential processes the wave contributes to, an estimation is possible how a QTDW event develops and what it does mean for the middle atmosphere.

Therefore, the mechanistic model COMMA-LIM will be applied to investigate the important processes in connection with the QTDW. The focus lies in dynamic studies, such as the impact of the wave on the mean flow and its interaction with manifold middle atmosphere waves. However, it will be difficult to give a final and complete description of the wave using a mechanistic model, since the onset of sudden dramatic changes of a mesospheric summer circulation will not arise self-consistently. Therefore, this circulation has to be prescribed. On the other hand, an amplification does not necessarily have to be related to another origin of the wave. The aim of this work is, through the investigation of the QTDW in all important processes, to bring together the accumulated knowledge of the wave using one model. This in turn will help to enhance the understanding of the dynamics of the middle atmosphere.

Chapter 3

COMMA-LIM

3.1 Description of the COMMA-Model, the LIM Version

3.1.1 Introduction

The Cologne Model of the Middle Atmosphere in the version of the Leipzig Institute for Meteorology (COMMA-LIM) is a 3D mechanistic grid point model based on the primitive equations on a sphere. In COMMA-LIM the troposphere is particularly considered as a lower boundary with only 4 to 5 vertical grid points, with no hydrological cycle nor orography. The so called *primitive* equations approximate the exact Navier-Stokes equations under the assumption of hydrostatic balance, a constant mean distance to the center of the earth and omitted Coriolis terms involving the vertical velocity in the horizontal-momentum equations (Phillips, 1966).

COMMA based on a hemispherical model for the stratosphere and mesosphere created by Rose (1983). Jakobs (1986) extended the vertical domain on a global scale up to 150 *km* geometric height. He also included thermospheric processes like ion drag, molecular heat conduction and dynamical viscosity as well as dissipation through breaking gravity waves. The parameterisation for gravity wave drag, which based on Lindzen (1981) was improved by Grollmann (1992) through extensions obtained from Holton and Zhu (1984), which allow the individual wave components to be absorbed by thermal damping and damped by self-generated eddy diffusion. Later, a detailed radiation routine for solar heating and infrared cooling was added by Berger (1994). It enabled the model to excite the solar tides self-consistently. In Cologne, COMMA also was used for chemical studies in the middle atmosphere, a chemical transport model was developed by Günther (1995) and Baier (2000) who built up an adjoint model (AMMOC) to assimilate ozone data. However, for the following work in Leipzig, the chemical processes were omitted.

Several improvements were made in the last years in the parameterisation of gravity wave drag, radiative processes, heating/cooling due to atmospheric waves and turbulence, as well as in the numerical realisation of the horizontal diffusion and filtering. New or updated climatologies for ozone, water vapour and geopotential are included. In the following the basic equations and some calculations for the updated parameterisations are described.

3.1.2 Numerical and computational properties

COMMA-LIM is a grid point model.

- **The horizontal resolution** of the earth is given in 36 latitudinal and 64 longitudinal points, referring to a $5^\circ \times 5.625^\circ$ mesh.
- **The vertical domain** consists of 48 layers extending from the ground up to 150 km in geometrical height. As vertical coordinate the log-pressure system is used. The logarithmic vertical coordinate is $z = -H \ln(p/p_0)$ with $H = 7 \text{ km}$ as the scale height and p_0 is the reference pressure at the lower boundary. The first grid point lies at 1.421 km and $\Delta z = 2.842 \text{ km}$. The uppermost layer in log-pressure height is therefore at 135 km.
- **Time integration scheme** The model equations are integrated numerically by using the Leapfrog-scheme. This method calculates the value a at time step $n+1$ via central differences from time step $n-1$ and tendency term at time n , $f(a_{m,n})$

$$a_{m,n+1} = \overline{a_{m,n-1}} + f(a_{m,n}) \cdot 2 \Delta t, \quad (3.1)$$

where

$$f(a_{m,n}) = -c \left(\frac{a_{m+1,n} - a_{m-1,n}}{2 \Delta x} \right) \quad (3.2)$$

with c as the phase velocity of the considered air parcel. To ensure stability of the numerical solution the 'Courant-Friedrich-Levy'-criterion is applied which states that $\|c \Delta t\| \leq \Delta x$. It is important to note that in the leapfrog-scheme the even and odd time steps are calculated independently from each other. For non-linear differential equations both solutions may diverge. Therefore, a numerical diffusive-scheme is applied following Asselin (1972), which incorporates an approximate second-order time filter into the time integration cycle. After each leapfrog step the filtering operation is applied to the actual time step. With the filter parameter $\varepsilon = 0.1$, we have

$$\overline{a_{m,n}} = a_{m,n} + \varepsilon(\overline{a_{m,n-1}} - 2a_{m,n} + a_{m,n+1}). \quad (3.3)$$

The time interval for the dynamic equations is $\Delta t = 450 \text{ s}$. Solar radiation, the gravity wave parameterisation and the molecular conduction scheme are computed hourly, whereas the infrared radiation scheme is solved every 6 hours.

- **The computation** of horizontal wind, temperature and geopotential is carried out on the grid points while the vertical velocity is calculated between them.
- **The model initialisation** is given by a temperature profile obtained from CIRA86, and a zero wind field. At the lower boundary a monthly climatology of zonal mean and stationary planetary wave with zonal wave number 1 is incorporated into the temperature and geopotential field. The differential radiation of the atmosphere forces the circulation and a steady state is obtained after approximately 90 days.

3.1.3 Dynamics

Model equations

The prognostic equations for horizontal wind components are the Navier-Stokes-equations, while the temperature is obtained using the first law of thermodynamics respectively. Because, of hydrostatic assumption, the vertical velocity w is calculated diagnostically from hydrostatic and continuity equation and density is given by the gas law. In principle, these are the same equations as used in the introduction (Eqs (1.6) to (1.9)). Additionally, the continuity equation is used to rewrite (1.6) to (1.9) in flux form, which ensures the compliance of the upper and lower boundary if the vertical velocity is treated correctly there. And so we obtain

$$\begin{aligned} \frac{\partial u}{\partial t} = & - \frac{1}{a \cos \phi} \frac{\partial u^2}{\partial \lambda} - \frac{1}{a \cos \phi} \frac{\partial}{\partial \phi} (uv \cos \phi) - \frac{1}{\rho_0} \frac{\partial}{\partial z} (\rho_0 u w) \\ & + \left(f + \frac{u}{a} \tan \phi \right) v - \frac{1}{a \cos \phi} \frac{\partial \Phi}{\partial \lambda} + F_\lambda, \end{aligned} \quad (3.4)$$

$$\begin{aligned} \frac{\partial v}{\partial t} = & - \frac{1}{a \cos \phi} \frac{\partial uv}{\partial \lambda} - \frac{1}{a \cos \phi} \frac{\partial}{\partial \phi} (v^2 \cos \phi) - \frac{1}{\rho_0} \frac{\partial}{\partial z} (\rho_0 v w) \\ & - \left(f + \frac{u}{a} \tan \phi \right) u - \frac{1}{a} \frac{\partial \Phi}{\partial \phi} + F_\phi, \end{aligned} \quad (3.5)$$

$$\begin{aligned} \frac{\partial T}{\partial t} = & - \frac{1}{a \cos \phi} \frac{\partial u T}{\partial \lambda} - \frac{1}{a \cos \phi} \frac{\partial}{\partial \phi} (v T \cos \phi) - \frac{1}{\rho_0} \frac{\partial}{\partial z} (\rho_0 w T) \\ & + \frac{R w T}{m' c_p H} + \left. \frac{\partial T}{\partial t} \right|_{sol} + \left. \frac{\partial T}{\partial t} \right|_{ir} + F_T \end{aligned} \quad (3.6)$$

$$0 = \frac{1}{a \cos \phi} \frac{\partial u}{\partial \lambda} + \frac{1}{a \cos \phi} \frac{\partial}{\partial \phi} (v \cos \phi) + \frac{1}{\rho_0} \frac{\partial}{\partial z} (\rho_0 w), \quad (3.7)$$

$$\frac{\partial \Phi}{\partial z} = \frac{R T}{m' H}. \quad (3.8)$$

The explanation of the symbols is given in the list of symbols. The first three terms of equation (3.4) describe the advection of the zonal momentum, followed by the Coriolis

force and pressure gradient. F_λ summarises the zonal dissipative and accelerating terms which will be described below. In analogy, the meridional momentum equation is built up. The thermodynamic energy equation also shows the advective terms in its first row, and the adiabatic heating and cooling as well as the contributions from absorption of solar radiation and flux divergence of infrared emission in the second row. F_T means the forcing via turbulent diffusion and molecular heat conduction. Then follow the two diagnostic equations: the continuity equation and the hydrostatic equation.

In appendix C Figures (C.1, C.2, C.3) show the different contributing parts of the horizontal momentum equations and the thermodynamic equation on COMMA-LIM day 90.

Boundary conditions

In COMMA-LIM the lower boundary condition follows from the climatological distribution of the geopotential height at 1000 *hPa*. At this level 11-year averaged data of geopotential height of zonal wavenumber 1 and 2 are included, derived from UKMO analyses (Fedulina et al., 2004). The initial state of atmosphere is that of a quiet atmosphere without wind and a given temperature profile from CIRA-86. Now, the first 90 days are calculated only with daily averaged heating rates, so all of the internal sources of global scale waves are switched off. In the end, we obtain averaged solutions of the given time point as $u_0, v_0, w_0, \Phi_0, T_0$. And then, step-by-step the daily variances, which occur if the earth is heated around the globe, are introduced with a characteristic time.

The surface of the earth, while a rigid surface in the geometric system, is moving in the log-pressure system (Eliassen, 1949). If the earth's surface is taken as the zero level of geopotential, then the kinematic lower boundary condition for perturbations of the geopotential due to internal sources at this surface is

$$\frac{D\Phi'}{Dt} = 0 \text{ at } z = 0, \quad (3.9)$$

where the operator D/Dt refers to the sum of local change and horizontal advection $D/Dt = \partial/\partial t + \nabla_H$. Remember that z is the log-pressure height. Earlier versions of COMMA used the condition $\Phi' = 0$ at $z = z_0$ for any wave generated by internal sources. This condition does not allow the model to respond to the resonant modes as the real atmosphere does.

In the new version the vertical streaming mass $W = \rho_0 w$ in COMMA-LIM is calculated after each time step via the continuity equation. At the lowest level, where W is calculated between inclined levels, the equation is

$$W_{k-0.5} = W_{k+0.5} + \Delta z \rho_0 \nabla_h \cdot \mathbf{v}_h, \quad (3.10)$$

where k is the number of the equation of prognostic changes, $\nabla_h \mathbf{v}$ the wind divergence on horizontal surfaces. At the upper boundary the condition

$$W_{NK+0.5} = 0 \text{ where } NK = 48 \quad (3.11)$$

is used. The equation at the lowest level is set to the height $z = \Delta z/2$. In this way from (3.10) we obtain at each time step the distribution of vertical velocity at $z = 0$.

Considering again the lower boundary condition (3.9), the geopotential field has to be separated into $\Phi(t) = \Phi_0 + \Phi'(t)$, where Φ_0 refers to the steady state solution, and $\Phi'(t)$ stands for the sources distributed in the atmosphere (due to heating variability, instability, or non-linear interaction of primary planetary waves) and the effects of these waves on the quasi-steady state solution. The latter part of $\Phi'(t)$ varies slowly with time. The material derivative of $\Phi(t)$ can be written as

$$\begin{aligned} \frac{D\Phi}{Dt} &= \frac{\partial\Phi_0}{\partial t} + \frac{\partial\Phi'(t)}{\partial t} \\ &+ \mathbf{v}(t)_h \cdot \nabla\Phi(t) + w(t)\frac{RT(t)}{H}. \end{aligned} \quad (3.12)$$

The partial derivative in time of Φ_0 must equal zero, but because of the introduced stationary planetary waves (SPWs) or other orographic effects the advective terms of the material derivation of Φ_0 are nonzero. However, $D\Phi'(t)/Dt = 0$ at $z = 0$ is the natural condition for tidal oscillations and other waves which are excited by some sources distributed in the atmosphere. So, now we have in spherical coordinates

$$\begin{aligned} \left. \frac{\partial\Phi(t)}{\partial t} \right|_{z=0} &= + \left(\frac{u_0}{a \cos\phi} \frac{\partial\Phi_0}{\partial\lambda} + \frac{v_0}{a} \frac{\partial\Phi_0}{\partial\phi} + w_0 \frac{RT_0}{H} \right) \\ &- \left(\frac{u(t)}{a \cos\phi} \frac{\partial\Phi(t)}{\partial\lambda} + \frac{v(t)}{a} \frac{\partial\Phi(t)}{\partial\phi} + w(t) \frac{RT(t)}{H} \right). \end{aligned} \quad (3.13)$$

To obtain the tendency for $\Phi(t)$ at $z = 0$, we have to extrapolate linearly the variables u , v , T from the above layers.

Gravity Waves

An important factor in the middle atmosphere are the upward propagating gravity waves which break mainly in mesopause heights and deposit momentum and heat there. This acceleration on the zonal mean flow causes a wind reversal and leads to a meridional circulation, which in turn causes upwelling in the summer hemisphere and downwelling in the winter hemisphere. Because gravity waves are far too small to be resolved in the COMMA-LIM grid, and neither orography nor cloud convection is applied, they have to be parameterised.

The gravity wave (GW) parameterising scheme is based on the approach by Lindzen (1981), which states that wave breaking occurs when the isentropes first become vertical, with $\partial\theta/\partial z = 0$, thus implying a loss of static stability and the onset of turbulence and mixing (see also Andrews et al. (1987)). This assumption is improved taking into account possible multiple breaking levels and wave propagation between layers where the wave is

saturated, as well as heating/cooling effects due to GW dissipation. The parameterisation is based on an analytical solution (WKB approximation) of the vertical structure equation for the GW in the atmosphere with realistic arbitrary background wind and realistic radiative damping. The Eddy diffusion coefficient is estimated using the idea of GW breaking due to instability proposed by Lindzen (1981). Appendix A describes the update on the Lindzen based scheme, developed by A. Pogoreltsev.

Solar Tides and Planetary Waves

Solar tides are generated in the model directly by absorption of radiation (see next section). A set of stationary (with zonal wave number $m=1, 2$) and travelling (the Rossby normal-mode and Kelvin waves) planetary waves can now be introduced into COMMA-LIM. For this purpose, the corresponding Hough functions as the latitudinal structure are calculated after (Swarztrauber and Kasahara, 1985). These waves can be added as heating terms near the tropopause level after COMMA-LIM day 90.

For each month 11-year averaged monthly mean UKMO assimilated data are included in the geopotential height field at 1000 hPa (Fedulina et al., 2004) to insert stationary planetary waves. This gives a different lower boundary conditions for each season and is one of the main reasons for different summer and winter climatologies in each hemisphere which otherwise would be approximately mirrored. In the current work only the stationary planetary wave with zonal wave number 1 (SPW1) is included.

In table (3.1.3) the possible to be forced planetary waves are listed. Note that the name of the waves and their period do not coincide in all cases. For instance, the 16-day wave has a period of only 15 days, the 5-day wave instead is set to 6.5 days in the model. The differences are given by the obtained solutions of the Laplace tidal equations and the observed values of these waves. Further, the periods are chosen due to the resonant response in the model calculation. For convenience we shall refer to the planetary waves based on their analytically obtained period. The latitudinal structure of these Kelvin waves has been calculated using the period to obtain the Hough-function, however these modes are not resonant Eigenmodes of the atmosphere.

The resolved waves (solar tides and planetary waves) deposit a mechanical energy in the atmosphere due to dissipation by molecular and turbulent viscosity, ion drag and Rayleigh friction. A part of this energy is lost through radiation and/or generation of other waves. The remaining energy has to be converted into heat. The viscous term in the energy balance equation can be separated into the "flux" and "dissipative" (always negative) parts. The loss of energy ("dissipative" part) can be written as follows

$$\varepsilon_v = -\frac{\mu}{\rho} \left(\frac{H}{H_T}\right)^2 \left[\left(\frac{\partial u}{\partial z}\right)^2 + \left(\frac{\partial v}{\partial z}\right)^2 \right], \quad (3.14)$$

where the dynamic viscosity $\mu = \mu_m + \rho\nu_e$, μ_m is the dynamic molecular viscosity, and ν_e is the kinematic eddy viscosity which is described here by the eddy diffusion D calculated

Planetary wave	Wave number	Period (h)	Hough mode
16-day wave (16DW)	1	-360	(1,3)
10-day wave (10DW)	1	-220	(1,2)
5-day wave (5DW)	1	-156	(1,1)
4-day wave (4DW)	2	-96	(2,1)
quasi 2-day wave (QTDW)	3	-52.5	(3,0)
slow Kelvin wave (SKW)	1	336	
fast Kelvin wave (FKW)	1	168	
ultra fast Kelvin wave (UFKW)	1	90	
15-day wave (15DW)	1	360	(2,3)

Table 3.1: Properties of the planetary waves. The negative or positive sign at the period refers to westward or eastward propagating waves, respectively.

in the gravity wave scheme. The molecular viscosity coefficient μ_m is calculated using the thermal conduction coefficient K_m by Eucken formula derived from kinetic theory (Forbes and Garrett, 1979) with $K_m = K_{m0}T^{2/3}/M$, where $K_{m0} = 0.015 JK^{-1}m^{-1}s^{-1}$ and M as the mean molecular weight in atomic mass units:

$$\mu_m = \frac{K_m}{0.25(9c_p - 5c_v)}. \quad (3.15)$$

The coefficient c_v is the specific heat at constant volume.

The losses of energy due to ion drag and Rayleigh friction can be presented in the following form

$$\varepsilon_{fr} = -\beta_{r\lambda}u^2 - \beta_{r\varphi}v^2, \quad (3.16)$$

where $\beta_{r\lambda}$ and $\beta_{r\varphi}$ are the combined ion drag and Rayleigh friction coefficients in the zonal and meridional momentum equation, respectively.

The most part of this mechanical energy has to be converted into heat and we have to include an additional heating term in the thermodynamic equation:

$$Q_M = -e_M(\varepsilon_v + \varepsilon_{fr})/c_p, \quad (3.17)$$

where e_M is the efficiency of the mechanical energy conversion into heat for the resolved waves and the mean flow. In the present study $e_M = 1$ has been used.

Cooling/heating of the atmosphere by turbulence and molecular heat conduction

By accounting the temperature stratification of the atmosphere, the second term in the right-hand side of the thermodynamic equation (A.28) can be written as follows

$$\frac{T}{\theta} \frac{H}{H_T} \frac{1}{\rho c_p} \frac{\partial}{\partial z} \left(\rho c_p \frac{D}{Pr} \frac{H}{H_T} \frac{\partial \theta}{\partial z} \right) = \frac{H}{H_T} \frac{1}{\rho c_p} \frac{\partial}{\partial z} \left[\rho K_h \left(\frac{H}{H_T} \frac{\partial T}{\partial z} + \frac{g}{c_p} \right) \right] + \frac{\kappa K_h}{c_p H_T} \left(\frac{H}{H_T} \frac{\partial T}{\partial z} + \frac{g}{c_p} \right), \quad (3.18)$$

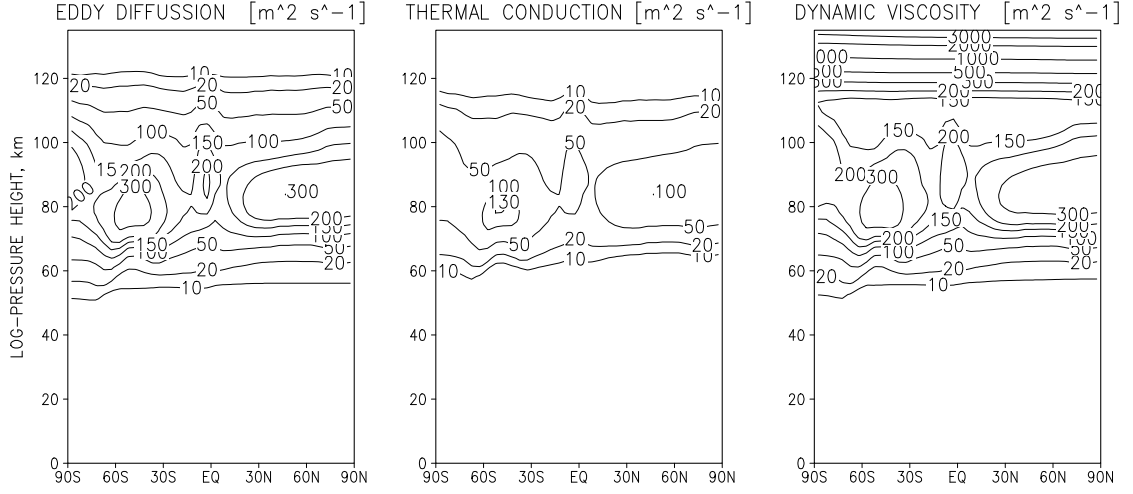


Figure 3.1: From left to right: eddy diffusion coefficient D , turbulent thermal conduction coefficient $K_h c_p^{-1} \rho^{-1}$ and the dynamic molecular viscosity coefficient $\mu_m \rho^{-1}$ as used in COMMA-LIM.

where $H = \text{const}$ and $H_T(z) = RT/g$ is the scale height for the atmosphere with a stratification of the temperature; $K_h = \rho c_p D / Pr$ is the coefficient of turbulent thermal conduction. It should be noted that there are several sources of turbulence, for instance, shear instability of the mean flow, breaking of solar tides and planetary waves. It means that in general $K_h \neq \rho c_p D / Pr$, where D is the eddy diffusion coefficient conditioned by the GW breaking, but in practice there is a gap of knowledge and so we use D . We assume that turbulence in the middle atmosphere is generated within relatively thin layers, and the effective eddy heat exchange is weaker than eddy transport of momentum, i.e., $Pr > 1$ (Coy and Fritts, 1988; Gavrilov and Yudin, 1992). In the present study we accept $Pr = 3$. In Fig.(3.1) the eddy diffusion coefficient D , the turbulent thermal conduction coefficient K_h and the dynamic molecular viscosity μ_m are shown. The latter two terms are weighted to show the same dimensions as D .

The heating term Q in (A.28) contains also the heating per unit mass due to dissipation of the turbulent energy ε_d / c_p (Izakov, 1978), and we can write the thermodynamic equation (A.28) in the following form

$$\frac{\partial T}{\partial t} + \mathbf{V} \cdot \nabla T + w \frac{\kappa T}{H} = -\frac{H}{H_T} \frac{1}{\rho c_p} \frac{\partial q_t}{\partial z} + \frac{\varepsilon_b + \varepsilon_d}{c_p} + Q - C, \quad (3.19)$$

where the turbulent flux of heat q_t and work against the buoyancy force ε_b are written as follows:

$$q_t = -\rho K_h \left(\frac{H}{H_T} \frac{\partial T}{\partial z} + \frac{g}{c_p} \right), \quad \varepsilon_b = \frac{g}{T} \frac{K_h}{c_p} \left(\frac{H}{H_T} \frac{\partial T}{\partial z} + \frac{g}{c_p} \right).$$

To estimate the role of the heating due to dissipation of the turbulent energy ε_d , we consider

the balance equation of the turbulent energy (Monin and Yaglom, 1975)

$$\frac{de_t}{dt} = \varepsilon_s - \varepsilon_b - \varepsilon_d = (1 - Ri_f)\varepsilon_s - \varepsilon_d, \quad (3.20)$$

where e_t is the turbulent energy per unit mass, ε_s is the source of turbulent energy due to shear instability of the mean flow, and $Ri_f = \varepsilon_b/\varepsilon_s$ is the dynamical (or flux) Richardson number (see Izakov (1978)). Under steady-state conditions $de_t/dt = 0$ we obtain

$$\varepsilon_d = \frac{1 - Ri_{fc}}{Ri_{fc}}\varepsilon_b, \quad (3.21)$$

where the critical flux Richardson number $Ri_{fc} = 1 - \varepsilon_d/\varepsilon_s$. In this case the thermodynamic equation can be written as follows:

$$\frac{\partial T}{\partial t} + \mathbf{V} \cdot \nabla T + w \frac{\kappa T}{H} = -\frac{H}{H_T} \frac{1}{\rho c_p} \frac{\partial q_t}{\partial z} + \frac{\varepsilon_b}{c_p Ri_{fc}} + Q - C. \quad (3.22)$$

Under stable stratification the divergence of the turbulent heat flux produces cooling of the atmosphere, and equation (3.18) shows that the relative role of cooling/heating due to turbulence depends on the value of the critical flux Richardson number. Measurements show that for the earth's thermosphere $0.2 \leq Ri_{fc} \leq 0.6$ (Izakov, 1978). In the present simulations $Ri_{fc} = 0.4$ has been used.

In the thermosphere the molecular thermal conduction plays an important role, and we have to replace q_t in (3.19) by $q = q_t + q_m$, where the molecular flux of heat q_m can be presented as follows:

$$q_m = -K_m \frac{H}{H_T} \frac{\partial T}{\partial z}.$$

K_m is the molecular thermal conduction coefficient, which is calculated by a semi-empirical formula as already mentioned.

Parameterisation of the horizontal turbulent diffusion

To smooth the subgrid-scale motions, which occur due to physical and numerical reasons, we now use the parameterisation of the horizontal turbulent diffusion suggested by Marchuk et al. (1984) instead of the usually used Shapiro-Filter. In the simplest form the terms describing horizontal diffusion in the zonal and meridional momentum equations can be written as follows:

$$F_u^H = \frac{K_H}{a^2 \cos^2 \varphi} \left[\frac{\partial^2 u}{\partial^2 \lambda} + \frac{\partial}{\partial \varphi} \cos^3 \varphi \frac{\partial}{\partial \varphi} \left(\frac{u}{\cos \varphi} \right) - 2 \sin \varphi \frac{\partial v}{\partial \lambda} \right], \quad (3.23)$$

$$F_v^H = \frac{K_H}{a^2 \cos^2 \varphi} \left[\frac{\partial^2 v}{\partial^2 \lambda} + \frac{\partial}{\partial \varphi} \cos^3 \varphi \frac{\partial}{\partial \varphi} \left(\frac{v}{\cos \varphi} \right) + 2 \sin \varphi \frac{\partial u}{\partial \lambda} \right], \quad (3.24)$$

where K_H is the horizontal diffusion coefficient. The corresponding term in the energy equation is:

$$F_T^H = \frac{K_H}{a^2 \cos^2 \varphi} \left[\frac{\partial^2 T}{\partial^2 \lambda} + \cos \varphi \frac{\partial}{\partial \varphi} \left(\cos \varphi \frac{\partial T}{\partial \varphi} \right) \right]. \quad (3.25)$$

In our simulation we use the height dependent horizontal diffusion coefficient

$$K_H(z) = [1.25 + 0.75 \tanh(\frac{z - z_0}{20})] 10^6 \text{ m}^2 \text{ s}^{-1}, \quad (3.26)$$

where z is the altitude in kilometers and $z_0=40$ or 60 km (referring to strong or weak coefficient of the horizontal diffusion in the stratosphere). In the present work $z_0 = 60 \text{ km}$.

Additionally, to suppress the motions with small unresolved vertical scales, a weak vertical bi-harmonic diffusion is introduced in the model, which practically does not influence the considered large-scale waves and the mean flow.

Ion drag, Lorentz deflection, and Rayleigh friction terms

In the lower thermosphere (the dynamo-region of the ionosphere) interaction between the ionised and neutral components can substantially influence the large-scale neutral gas motions. If ionised particles move in the earth's magnetic field they underlie the Lorentz force and are able to propagate freely only in the parallel direction to the magnetic field. Thus, in zonal direction the ionised gas acts as a stationary medium that decelerates the neutral gas moving in this direction. Also, the deflected ionised gas exerted by Lorentz force leads to a compensation of Coriolis force in the propagating neutral gas. To take into account this interaction, we have to include the electromagnetic force $c^{-1}[\mathbf{j} \times \mathbf{B}]$ into the momentum equation, where c is the speed of light, \mathbf{B} is the geomagnetic field, and the electric current density \mathbf{j} can be presented as follows:

$$\mathbf{j} = \sigma_0(\mathbf{E}' \cdot \mathbf{B})\mathbf{B}/B_0^2 + \sigma_1\mathbf{B} \times \mathbf{E}' \times \mathbf{B}/B_0^2 + \sigma_2\mathbf{B} \times \mathbf{E}'/B_0, \quad (3.27)$$

where $\mathbf{E}' = \mathbf{E} + c^{-1}[\mathbf{V} \times \mathbf{B}]$; σ_0 , σ_1 , and σ_2 are parallel, Pedersen, and Hall conductivities, respectively. Note, that \mathbf{V} is the *horizontal* wind field. Assuming $\mathbf{E}=0$ (the electrostatic electric field assumed to be negligible) and using the geomagnetic field in the form of magnetic dipole $\mathbf{B} = \{B_x, B_y, B_z\} = B_0\{0, \cos \varphi/(1 + 3 \sin^2 \varphi)^{1/2}, -2 \sin \varphi/(1 + 3 \sin^2 \varphi)^{1/2}\}$, we obtain the ion drag and Lorentz deflection terms, which can be presented as additional Rayleigh friction coefficients in the zonal and meridional momentum equations and correction to the Coriolis term, respectively

$$\beta_{r\lambda} = \beta_r + \frac{\sigma_1 B_0^2}{\rho c^2}, \quad \beta_{r\varphi} = \beta_r + \frac{\sigma_1 B_0^2 4 \sin^2 \varphi}{\rho c^2 (1 + 3 \sin^2 \varphi)}, \quad (3.28)$$

and

$$2\Omega \sin \varphi \quad - > \quad \left(2\Omega - \frac{\sigma_2 B_0^2 2 \sin \varphi}{\rho c^2 \sqrt{1 + 3 \sin^2 \varphi}} \right) \sin \varphi. \quad (3.29)$$

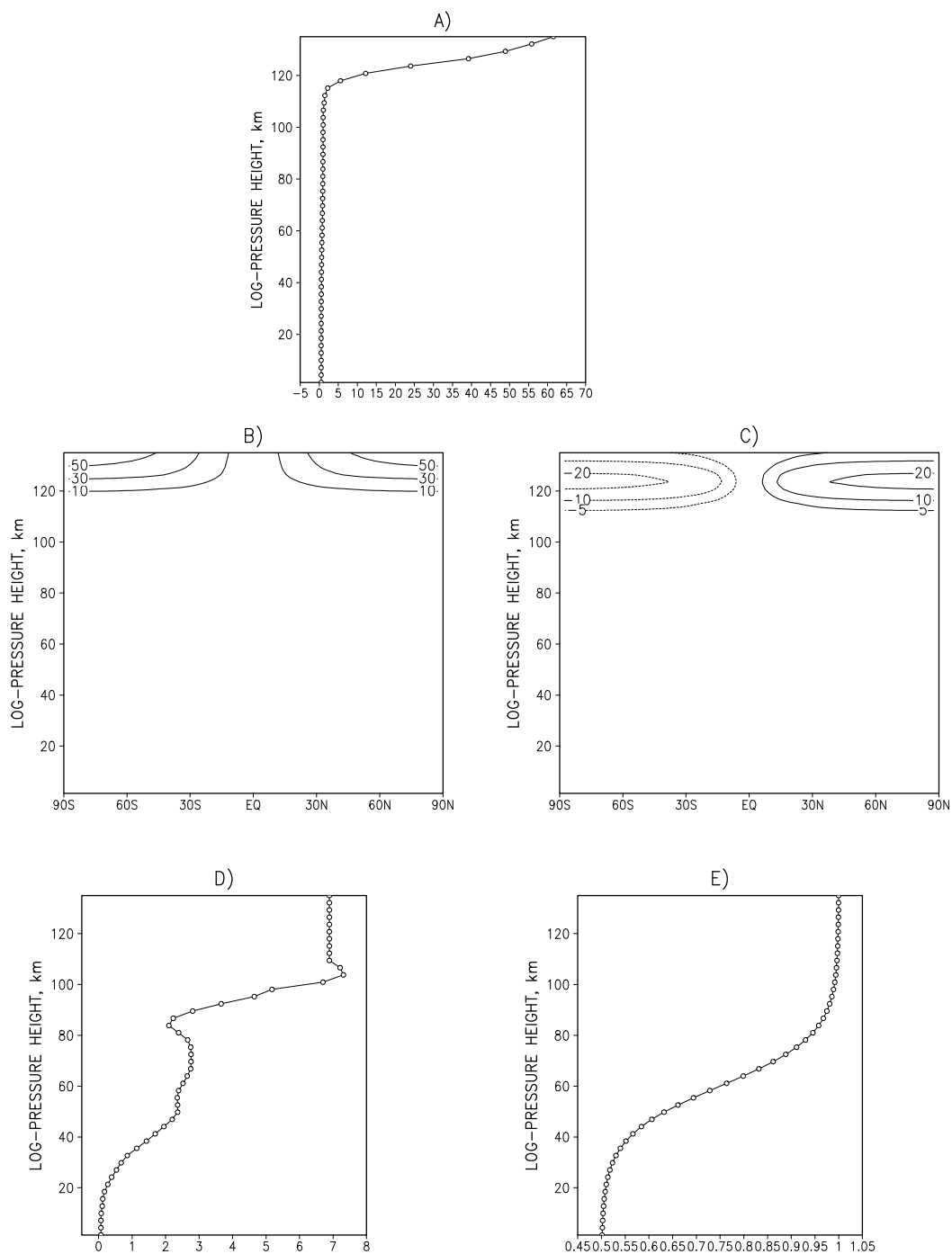


Figure 3.2: A) Rayleigh friction $\beta_{r\lambda}$ with correction term for ion drag in zonal direction, and B) in meridional direction $\beta_{r\phi}$. C) Lorentz deflection, D) Newton cooling coefficient α , and E) Rayleigh friction β_r as used in COMMA-LIM. Units are given in $10^{-6} s^{-1}$.

Daily averaged profiles of Pedersen and Hall conductivities are calculated as averaged over low latitudes ($-45^\circ \leq \varphi \leq 45^\circ$) using empirical models of the thermosphere and ionosphere and standard expressions for collision frequencies (Pogoreltsev, 1996).

The background Rayleigh friction coefficient β_r is introduced to parameterise the loss of energy due to non-linear interaction of the mean flow and resolved waves with other waves, which are not taken into consideration. The role of the non-linear processes increases with altitude (McLandress, 2002), and we use an analytical formula to account for this effect:

$$\beta_r(z) = [1.25 + 0.75 \tanh(\frac{z - z_0}{20})] 10^{-6} \text{ s}^{-1}, \quad (3.30)$$

where z and z_0 are defined as aforementioned (compare with Eq.(3.26)) but represent strong or weak Rayleigh friction coefficient in the stratosphere. In Figure (3.2) the terms $\beta_{r\lambda}$, $\beta_{r\varphi}$, $\sigma_2 B_0 B_z / \rho / c^2$, α and β_r are displayed. Note, that the horizontal diffusion coefficient K_H has the same profile as β_r .

3.1.4 Radiation

Heating due to absorption of solar radiation

An important assumption for radiative calculations is the plane-parallel approximation, which neglects the curvature of the earth and reduces in this way the properties of the medium and radiation field to only the vertical dependence. In the middle atmosphere this condition is well satisfied because there are not such large horizontal inhomogeneities as in the troposphere. But at large solar zenith angles θ_0 , a correction must be applied. Because of the earth's curvature, solar radiation can reach the upper atmosphere even if the sun is below the horizon. In this case we use *Chapman functions* to evaluate the integral of the optical depth (Berger, 1994). An outline on the calculation of rates of absorption and emission is given in Appendix B.

Heating of the most important gases as water vapour, carbon dioxide, ozone and oxygen and nitrogen is considered and calculated in the routine after Strobel (1978).

1. The water vapour field was extracted from the NCEP/NCAR data between 1000 and 300 *hPa* levels and the climatology was separated into 4 time-harmonics to describe the seasonal behaviour of this component in the troposphere. In the vertical an analytical decreasing with height function obtained empirically is applied. Heating due to absorption of H_2O is adjusted according to Liou (1992). Rayleigh scattering and surface reflection are taken into account for heating of H_2O . The heating rates are divided into 6 frequency intervals with the central wavelengths of 0.94 μm , 1.1 μm , 1.38 μm , 1.87 μm , 2.7 μm and 3.2 μm .
2. Carbon dioxide is assumed to be equally distributed up to ~ 80 *km* and to decrease above, the volume mixing ratio is set to 360 *ppmV*; but CO_2 gives the most sub-

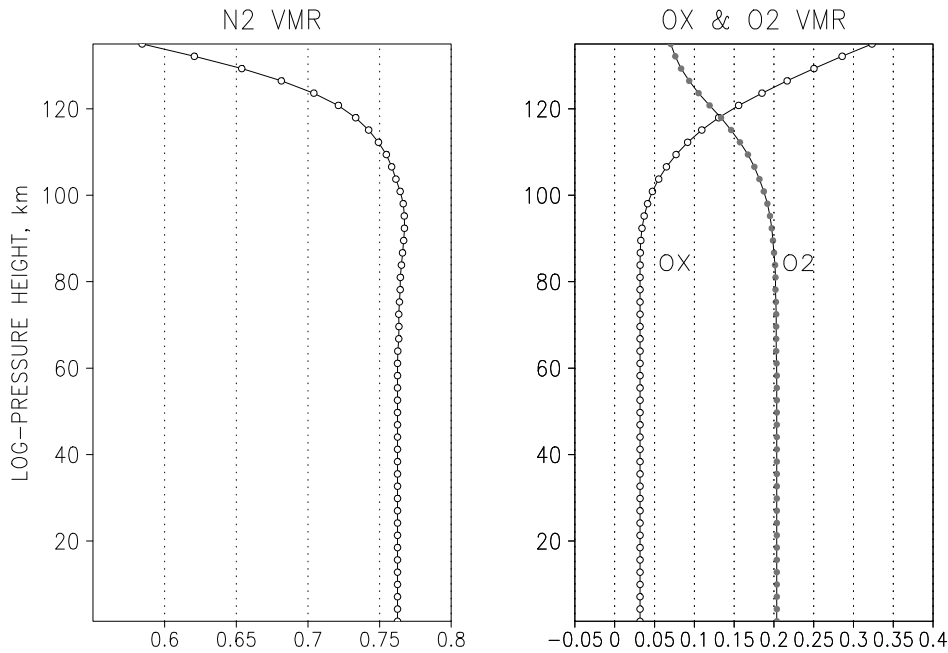


Figure 3.3: Volume mixing ratios of N_2 , O_2 and O

stantial contribution to heat in the troposphere and lower stratosphere because its absorption is strongly dependent on the pressure ratio. Again, the heating rate of CO_2 is adjusted according to Liou (1992).

- Ozone clearly dominates stratospheric heating but has a secondary maximum in the mesosphere. Ozone data are used from the Berlin climatology (Fortuin and Langematz, 1995) and combined with new satellite data from GOME (Global Ozone Monitoring Experiment) by I. Fedulina. The GOME data were averaged from 1996-2002. Monthly means are used. In Figure (3.4) the ozone distribution is displayed for July conditions. Ozone absorbs the solar flux in the

- Herzberg band (205-242 nm) at around 40-100 km height,
- Hartley band (200 -300 nm) between 30 - 100 km ,
- Huggins band (300-350 nm) between 20 - 100 km ,
- Chappius band (450-700 nm) between 20 - 60 km .

- Atomic and molecular oxygen are given as climatological globally averaged profiles of the volume-mixing ratio. In the thermosphere atomic oxygen becomes much more important (Figure 3.3). O_2 absorption takes place in the stratosphere together with O_3 in the Herzberg band but the strongest absorption occurs in lower thermospheric heights. There

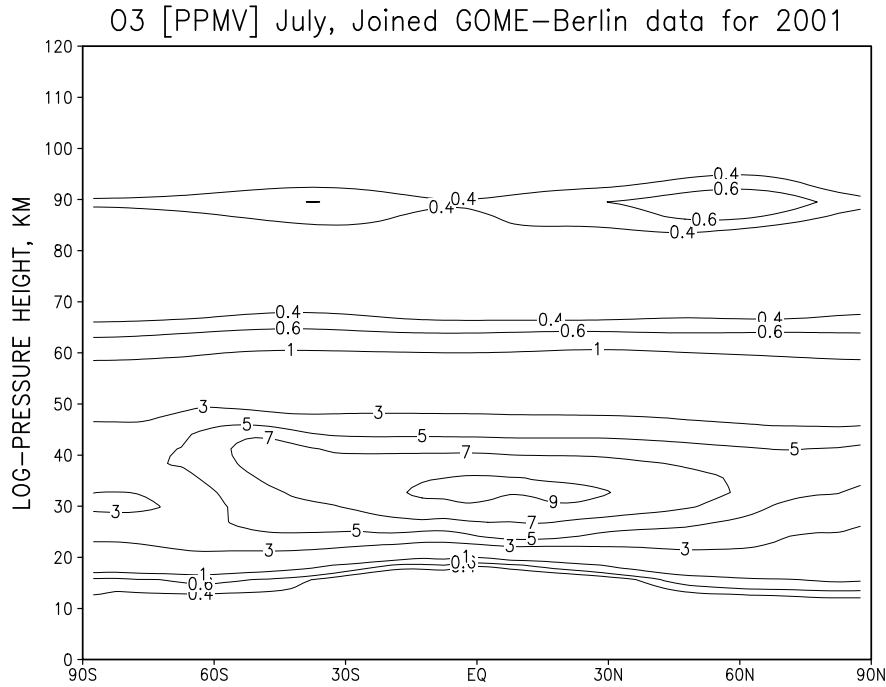
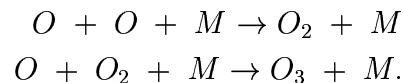


Figure 3.4: Ozone climatology for July.

- the Schumann-Runge band (175-205 nm),
- the Schumann-Runge continuum (125-175 nm) and
- the Lyman- α line at 121 nm

are the main absorption bands. Additionally, in the EUV range from 5-105 nm molecular oxygen plays a role together with atomic oxygen.

5. Nitrogen is a radiative unimportant gas, the absorption is nonegligible only in the thermosphere. Nitrogen absorption in the EUV-bands is taken into account.
6. Two processes of chemical heating due to recombination reactions of O_2 and O_3 are added to the radiation routine according Riese et al. (1994):



In order to take into account the energy losses because of low frequent collisions between molecules above $\sim 70 km$, the approach suggested by Mlynzak and Solomon (1993) was incorporated into the routine. In Figure (B.1) the different heating rates are displayed.

Cooling due to infrared radiation

Infrared radiation is the terrestrial radiation flux, which balances the solar flux in the atmosphere. For more details the reader is also referred to Appendix B or to Andrews et al. (1987); Lange (2001).

In the upper atmosphere at around 70 km the local thermodynamic equilibrium breaks down because the mean free path length of molecules becomes more and more larger and the Boltzmann distribution is not longer valid. Then, the source function departs strongly from the Planck function so that non-LTE formulations have to be applied.

The most important gas components responsible for IR cooling/heating are H_2O , CO_2 and O_3 . Again,

- water vapour is relevant especially in the troposphere. The 6.3 μm band with 9 intervals are calculated. The parameterisation follows formulations by Chou et al. (1993).
- Ozone contributes to cooling mainly in the 9.6 μm -band in the upper stratosphere/lower mesosphere. The cooling rates are calculated after a scheme developed by Fomichev and Shved (1985).
- Carbon dioxide absorbs IR radiation in the 15 μm band in the troposphere as well as in the stratosphere and mesosphere/lower thermosphere under LTE and non-LTE conditions. Now in COMMA-LIM also exists a parameterisation for the troposphere following Chou et al. (1993). The processes in the middle and upper atmosphere are described by Fomichev et al. (1998); Ogibalov et al. (2000). Details are given in Lange (2001).
- NO is currently not considered in COMMA-LIM.

The cooling rates are displayed in Fig.(B.2). The bottom panels show the contributions of CO_2 and H_2O in the troposphere and lower stratosphere. The water vapour exhibits two minima arising from surface fluxes in the summer hemisphere. Carbon dioxide IR-radiation absorption contributes to weak heating in the troposphere, whereas the 15 μm -band leads to strong cooling in the upper atmosphere.

There are two possibilities in COMMA-LIM to calculate the cooling processes. Either with an explicit longitudinal dependence - which means the temperature dependence - or as a fast longitudinal independent scheme, which is corrected by Newton cooling processes of planetary waves and tides. In this work, the latter method is applied.

The climatology of the middle atmosphere simulated with COMMA-LIM is presented and discussed in appendix C for the month of July since all following calculations are done for northern hemisphere summer conditions.

Chapter 4

Results

4.1 The QTDW in the COMMA - LIM model

The following section describes and discusses the numerical experiments performed with a QTDW forced from the ground and its development and propagation into mesospheric heights. All experiments were carried out under July conditions. After the steady state is obtained, the tides and the travelling planetary waves are included and established within 30 days. Afterwards, the 30 days of July were recorded in a consecutive order, usually with a 4-hourly output.

In order to obtain a picture of how the QTDW propagates and behaves in the model we have to analyse the wave from the data. The method of the least squares is used in order to extract the wave numbers in time series. The time series of the wave number then is again subject to the least square method in order to calculate the response of the estimated frequency of the wave.

4.2 Steady forcing as an Eigenmode

The quasi two-day wave was inserted into the model as a heating disturbance per unit mass at around the tropopause level. The forcing itself was smoothed in the vertical with an exponential factor F and the disturbance term h_{2dw} was defined by the properties of the wave:

$$h_{2dw} = A \Phi(\phi) F(z) \cos(kx - \omega t) \quad (4.1)$$

where $F(z) = \exp[-\frac{(z-10)^2}{25}]$ with z in km, A is the amplitude scaled to produce the observed values, $\Phi(\phi)$ represents the latitudinal structure of the wave, obtained from Hough-mode calculations for the Rossby-gravity wave (3,0) (Swarztrauber and Kasahara (1985), see also Fig.(4.1)). The zonal wave number is given by $k = 3$, $x = 2\pi\lambda/360^\circ$. Within the angular frequency $\omega = 2\pi/T$ the period $T = 52.5 h$ has been chosen, as this period gives

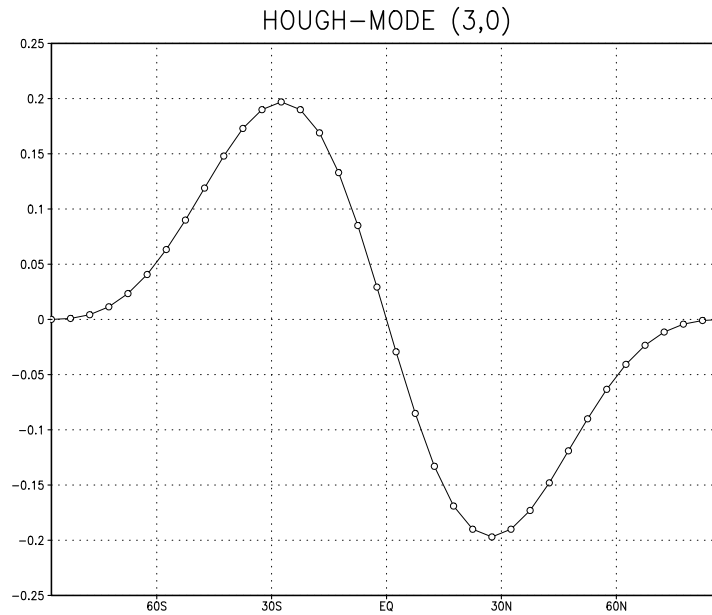


Figure 4.1: Hough-mode for the temperature disturbance of the QTDW. Values are non-dimensional.

the resonant response in COMMA-LIM. The first experiment was a control run of July conditions including only the SPW1 (case 1.A). The second run included the steady forced QTDW (case 1.B).

In Fig.(4.2) the amplitudes and phases of the QTDW in the wind, temperature and geopotential fields are displayed. The main characteristic is the maximum of the meridional wind above the equator while the other variables show maxima in both hemispheres - more pronounced in the summer hemisphere - and a node at the equator. This behaviour is typical for a Rossby-gravity wave with asymmetric mode (Johnson and Killeen, 1995), which is confirmed by the displayed phases. However, the phase structures only show vertical wavelengths of about $\sim 60 - 70 \text{ km}$, where more than 100 km were expected. The meridional amplitude shows a maximum in the equatorial mesosphere which is twice as strong as that for the zonal wind. With increasing latitude towards the north pole both wind components become comparable in magnitude. All amplitude fields show a well-pronounced propagation into the summer hemisphere and a suppression of the wave on the winter side. When compared to the plots obtained by Salby (1981) the wave matches all characteristic properties, however, the absolute values of amplitudes are smaller.

The way in which QTDW-structures propagate around the globe is shown in Fig.(4.3) in a polar stereographic plot of the northern hemisphere. In order to display the behaviour of the wave in a times series, only the wave number 3 pattern for meridional wind has been used. The terdiurnal tide, which is not separated at this stage of analysis, was excluded by

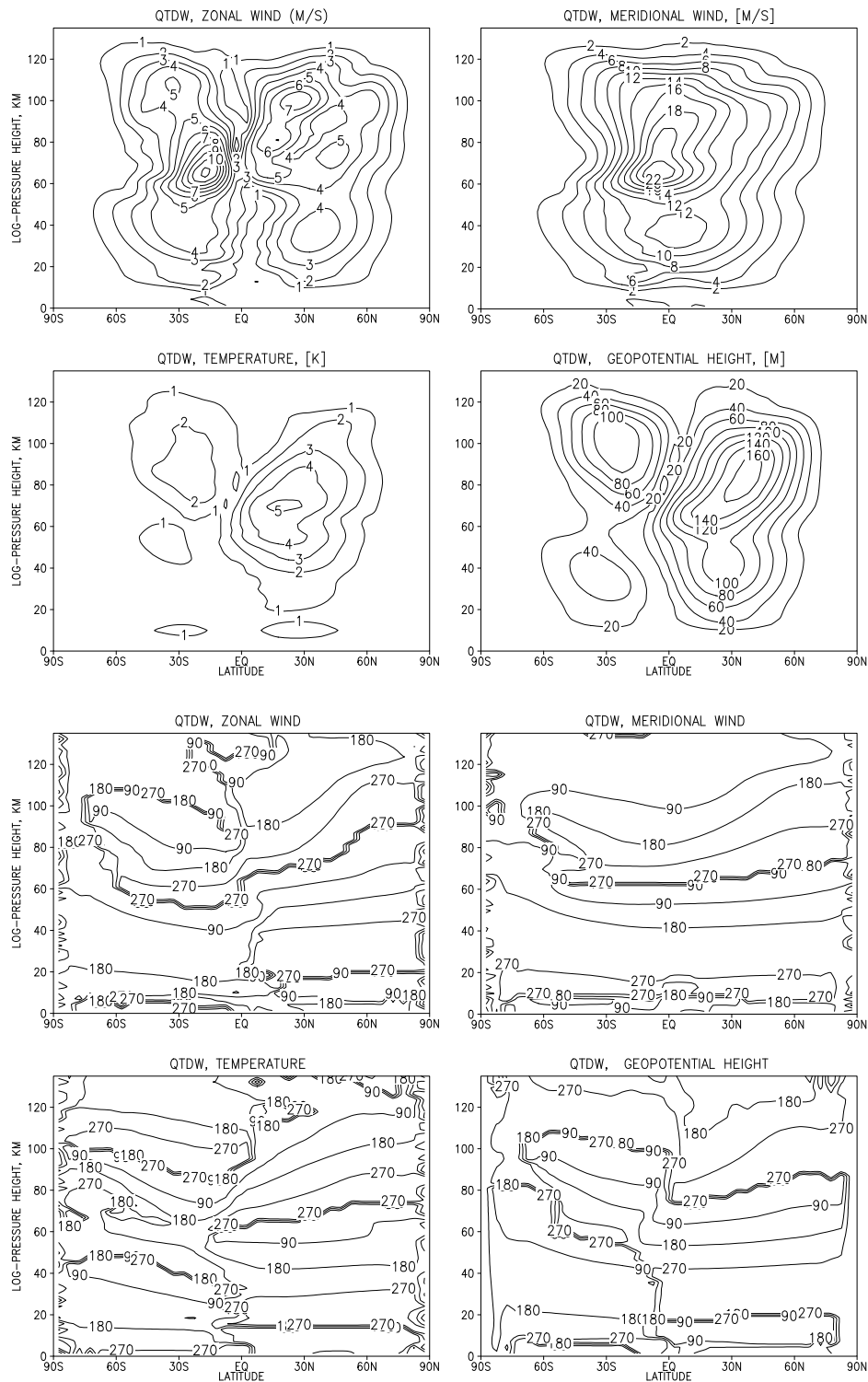


Figure 4.2: Amplitudes (top) and phases (bottom) of the QTDW with wave number 3, and period $T = 52.5 h$ for zonal and meridional wind, temperature and geopotential.

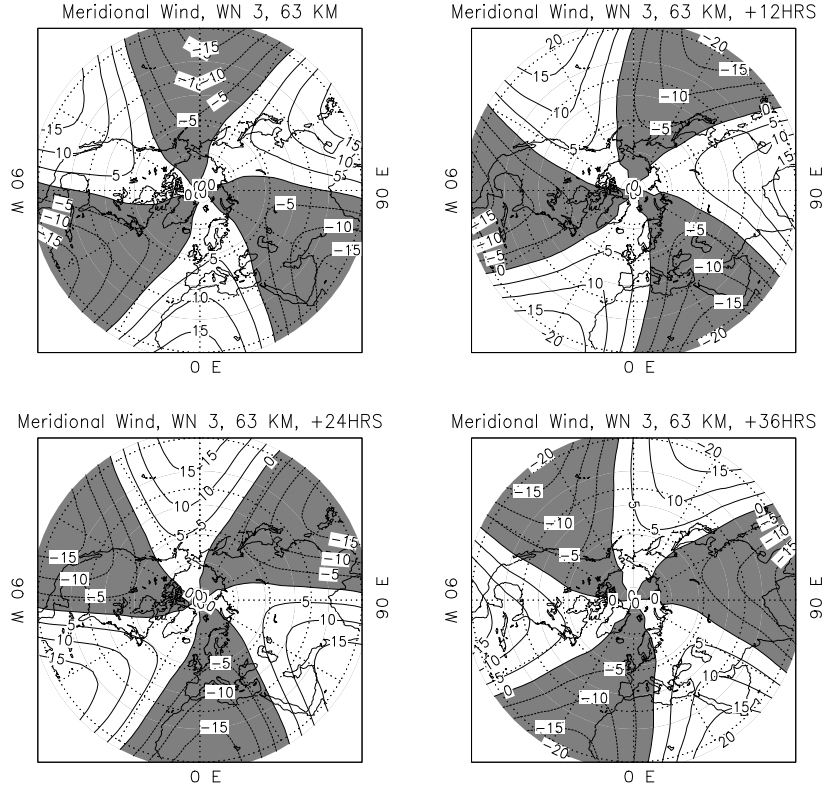


Figure 4.3: Time series of meridional wind structure for wave number 3. Outer circle: $10^\circ N$. Negative values are shaded.

choosing a lower mesospheric height level. The minimum at $180^\circ W$ in the upper left panel moves westward - clockwise - and accomplishes as expected 90° after 36 hours.

Fig.(4.4) demonstrates further properties of the Rossby-gravity wave. The QTDW-geopotential field shows alternating regions of high and low geopotential height with respect to the equator. There, the horizontal wind perturbations flow clockwise if the geopotential high is at the northern hemisphere and anticlockwise if there is a low. On the right panel a longitude-height cross-section at $30^\circ N$ is shown for the stratosphere and mesosphere; negative temperature perturbations are shaded. Note the coincidence of positive temperature and positive (northward) meridional wind highlighting the transport of warm air northwards and cold air southwards. The westward travelling QTDW also shows a westward tilt with height as is characteristic of westward travelling Rossby-waves.

Fig.(4.5) displays the divergence of Eliassen-Palm flux $\mathbf{F} \equiv (0, F^\phi, F^z)$ in the left panel using spherical coordinates:

$$\nabla \cdot \mathbf{F} \equiv (a \cos\phi)^{-1} \frac{\partial}{\partial \phi} (F^\phi \cos\phi) + \frac{\partial F^z}{\partial z}, \quad (4.2)$$

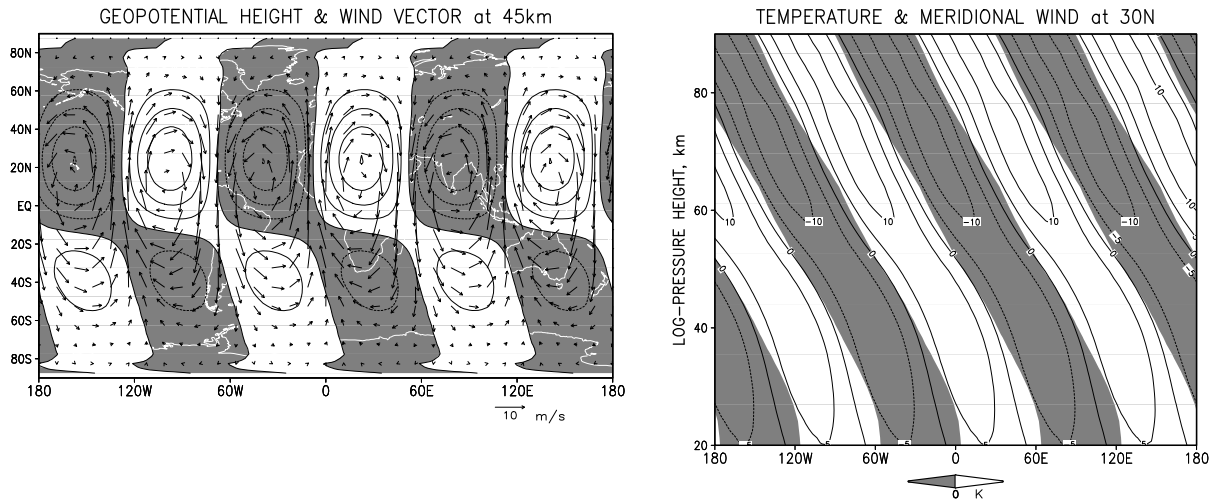


Figure 4.4: Left panel: Longitude-latitude cross-section of geopotential and horizontal wind fluctuations for the QTDW. Negative values of geopotential height are shaded. Right panel: Longitude-height cross-section for temperature and meridional wind perturbation, with shaded negative temperature values.

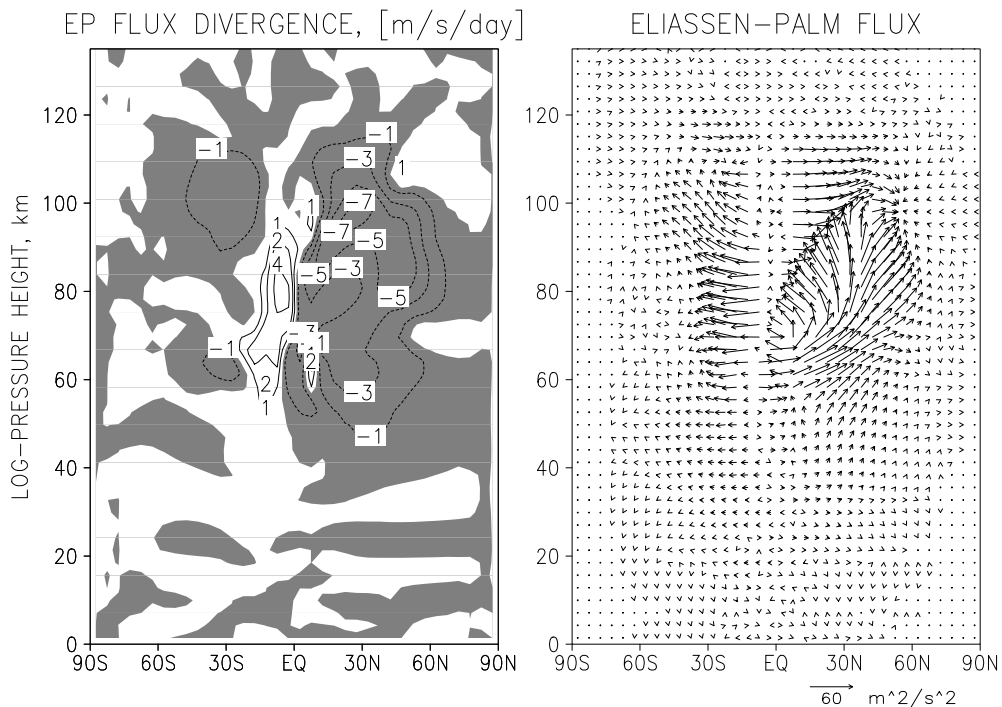


Figure 4.5: Left panel: Force per unit mass due to divergence of Eliassen-Palm flux exerted by the QTDW. Negative values are shaded. Right panel: Eliassen-Palm flux vector with enhanced vertical component ($F_z \cdot 100$) to highlight the upward propagation direction. July mean.

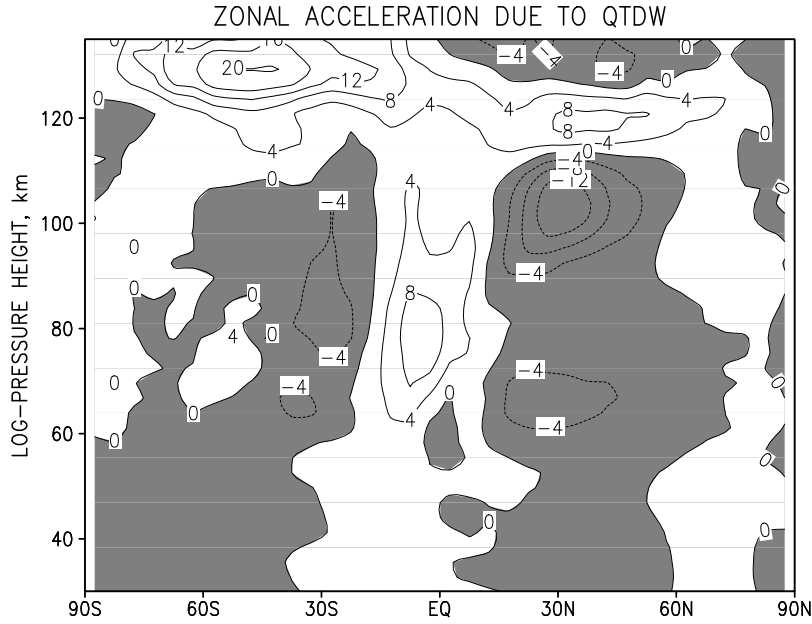


Figure 4.6: Resulting zonal acceleration exerted by the QTDW.

with the vector components in spherical coordinates

$$F^\phi = \rho_0 a \cos\phi \left(\overline{u_z} \frac{\overline{v' \theta'}}{\theta_z} - \overline{v' u'} \right), \quad (4.3)$$

$$F^z = \rho_0 a \cos\phi \left\{ \left[f - \frac{1}{a \cos\phi} (\overline{u} \cos\phi)_\phi \right] \frac{\overline{v' \theta'}}{\theta_z} - \overline{w' u'} \right\}. \quad (4.4)$$

The EP-flux divergence is mapped as force *per unit mass* and the vector components are also depicted as fluxes per unit mass. The QTDW exerts mainly a negative acceleration of up to $7 \text{ m s}^{-1} \text{ d}^{-1}$ on the summer mesosphere. An eastward acceleration exists only in the tropical winter mesosphere. The zonal wind amplitude plays the main role in the positive acceleration. The structure of the zonal wind amplitude – 2 maxima at low latitudes and a minimum at the equator – leads to an interaction with the meridional wind disturbance which produces several intense cells of the meridional momentum flux $\overline{v' u'}$ with alternating signs and leads therefore to strong gradients of the latter. This pattern is responsible for the positive acceleration because the eddy heat flux divergence is of negligible magnitude there. A comparison of Fig.(4.5) with observational data (see Fig.(2.5)) for a southern hemisphere wave event reveals that the structure as well as the order of magnitude of flux divergence are very similar.

Regarding the EP-flux vector itself, it turns out that the wave fluxes are divided into summer and winter branches. The vertical component F^z was multiplied by a factor of 100 to highlight the upward direction. At the winter low latitudes the fluxes are directed southwards and weakly upwards throughout the mesosphere and lower thermosphere. The

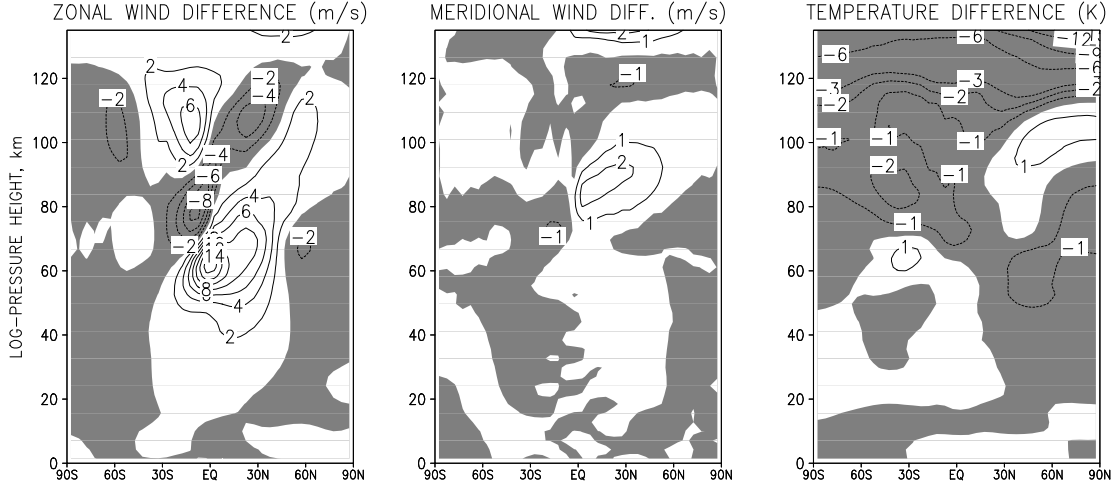


Figure 4.7: Plots of the July climatology (zonal and monthly mean) with and without QTDW (1.A - 1.B) left: zonal wind difference, middle: meridional wind difference, and right: temperature difference.

summer hemisphere shows fluxes emanating upwards and northwards as well as equatorwards. Along a region tilted from the equator at 70 km to 30° N at 100 km a strong convergent pattern can be recognised indicating dissipation processes of the wave amplitudes just above their maxima.

In order to estimate the resulting zonal acceleration all terms of the zonal momentum equation of the *transformed Eulerian mean* have to be calculated in spherical coordinates

$$\frac{\partial \bar{u}}{\partial t} + \bar{v}^* \left[\frac{(\bar{u} \cos \phi)_\phi}{a \cos \phi} - f \right] + \bar{w}^* \frac{\partial \bar{u}}{\partial z} - \bar{\mathbf{X}} = \frac{\nabla \cdot \mathbf{F}}{\rho_0 a \cos \phi}, \quad (4.5)$$

with the residual mean meridional circulation, where wave driven parts are removed from the mean velocities

$$\bar{v}^* \equiv \bar{v} - \rho_0^{-1} (\rho_0 \overline{v'\theta'}) / \bar{\theta}_z \quad (4.6)$$

$$\bar{w}^* \equiv \bar{w} + (a \cos \phi)^{-1} (\cos \phi \overline{v'\theta'}) / \bar{\theta}_z \quad (4.7)$$

The frictional processes that contributed to the drag $\bar{\mathbf{X}}$ are breaking gravity waves, molecular and eddy viscosity, Rayleigh friction and turbulent diffusion. Fig.(4.6) shows that the structure of the resulting zonal acceleration resembles the EP-flux-divergence pattern. Thus, the residual mean meridional circulation is almost balanced by the frictional processes. The QTDW intensifies the westward jet in the summer mesosphere at $\sim 60 \text{ km}$. There is a second negative maximum in the lower summer thermosphere. The local minimum between the two maxima of westward acceleration might be caused by the eastward acceleration due to breaking gravity waves.

The difference between the control experiment (1.A) and the experiment that includes the QTDW (1.B) is displayed in Fig.(4.7). The left panel shows that the mesospheric summer jet at low-to-mid latitudes is enhanced in accordance with the results of EP-flux divergence. Also the differences in the wind reversal at the subtropical MLT region show that a QTDW intensifies the circulation. However, the occurrence of both positive and negative differences pointed to a tilted and shifted wind reversal at the summer MLT. The positive change in the meridional wind of about 2 m s^{-1} in the summer mesopause represents an enhancement of 25% since the mean meridional wind in COMMA-LIM is about -7 to -8 m s^{-1} . The increased meridional transport towards the south results in a colder polar summer mesopause as indicated by the positive difference of $\sim 1 \text{ K}$ there. The negative cell below may stem from dissipative processes due to QTDW wave breaking.

4.3 Transient forcing

Since the QTDW is known to show a very transient behaviour (e.g. Wu et al. (1996), Thayaparan et al. (1997) and Fritts et al. (1999)), this study analyses the extent to which a *transient* "Eigenmode - QTDW" is able to exert an influence on the mean flow in comparison to a steady wave. According to the theory, the acceleration of a transient wave on the mean flow must be stronger. It is important to note, that on a monthly mean basis, the differences become negligible, given the condition that the transient wave amplitude oscillates around the level of the steady wave. Therefore, increasing and decreasing wave amplitudes over a relatively short time-scale and the consequences of this were the subject of investigation.

Listing	Experiment
1.A	control run including the SPW1
1.B	run including the steady forced QTDW
1.C	run including the transient forced QTDW
1.D	run of 60 days for July 1 including the steady forced QTDW
1.E	run of 60 days for July 1 including the transient forced QTDW

Table 4.1: Overview of the experiments.

In order to carry out this numerical experiment several calculations were performed (see also table(4.1)). The first was again the control run of the undisturbed July atmosphere including only the SPW1 (case 1.A). The second run was performed with the additional forcing of a steady quasi two-day wave as was explained in the previous section (case 1.B) while the third included the transient forced wave (case 1.C). Further experiments tested the transient and steady wave for 60 days under fixed summer conditions (case 1.D and 1.E). In order to obtain an insight into the time dependent behaviour of the wave the frequency analysis of the time series with 4-hourly output for one month was subject to a

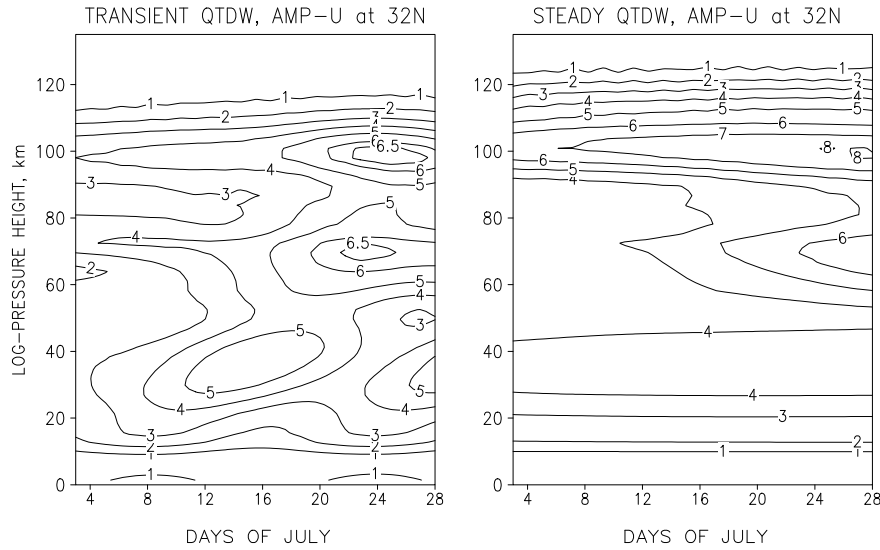


Figure 4.8: Time-height cross-section at $32^\circ N$ for the transient (case 1.C) and steady QTDW (case 1.B) in the zonal wind.

sliding window of a 6 day interval moving in a one-day step. Therefore, only 25 days can be presented and values are shown for the centre of the interval.

The transient wave starts with a lower amplitude and oscillates in a sine-quadratic-form around the steady state amplitude-level in order to ensure that the energy input at the tropopause of both waves is the same. The oscillation is forced twice during the 30 days of July, peaking firstly at the tropopause level around day 8 and subsequently \sim day 24.

The transient forcing as well as the steady behaviour of the QTDW-amplitude of zonal wind are presented in Fig.(4.8) for summer mid-latitudes, where the zonal wind amplitude has a maximum. The double peak of tropopause forcing is well depicted in the left panel. The transient signal needs approximately 14-15 days to propagate into the mesosphere, but within the mesosphere the upward propagation takes only two days. In the thermosphere both transient and steady wave amplitudes decrease rapidly with height, however the steady QTDW amplitude extends higher than the transient amplitude does. The reason that the transient QTDW is not well established at these heights is due to the non-steady nature of the mean flow itself.

In order to estimate the different behaviour of both experiments, days 21 to 27 have been averaged since at this time the transient wave peaks firstly in the MLT region. The Fig.(4.9) shows in the top panels horizontal wind amplitudes for the transient forced QTDW. The pictures below plot the difference of the steady and transient case. Negative values indicate stronger transient wave propagation. At height levels up to 100 km the difference structure highlights the regions where the transient QTDW shows local maxima - in the lower stratosphere and in the mesosphere - and a minimum in the upper stratosphere. The

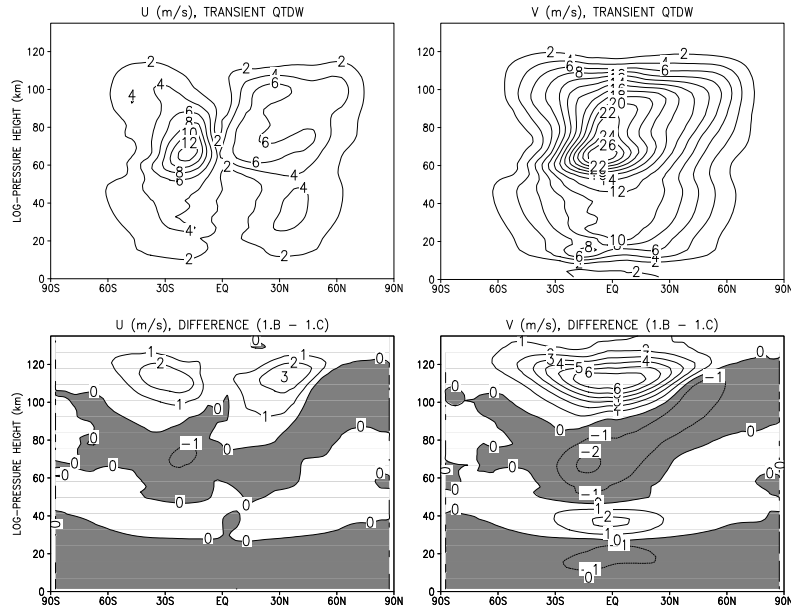


Figure 4.9: Top: Amplitudes of QTDW in zonal and meridional wind for transient forcing averaged from day 21 to day 27. Below: The differences between the steady QTDW and the transient QTDW are shown for the same time period.

positive values in the lower thermosphere show the more established steady QTDW.

If one compares the mean zonal wind for experiment 1.B and experiment 1.C (see Fig.(4.10)) for the same time period the differences proved to be relatively small. However, at the summer hemisphere low-latitudes, where the wave propagates, a positive difference in the westward jet is shown which means a stronger westward wind for the transient case. The negative difference above indicates weaker eastward wind. Please note that this difference reduces in magnitude if a monthly average is taken since the transient wave establishes very slowly in the mesosphere. However, a time average of two completed oscillations in the middle atmosphere during experiments 1.D and 1.E gives a similar pattern even with reduced absolute values (see Fig.(4.11)). This means that two effects compete against each other - a transient QTDW exerts a stronger impact on the equatorial mean flow but the middle atmosphere behaves relatively resistant to change.

In order to gain a detailed view of the time dependent behaviour at the summer tropics, the zonal mean wind, the meridional wind amplitude of QTDW, and its force per unit mass due to divergence of Eliassen-Palm flux, are considered. Fig.(4.12) shows a comparison of the time series of the three aforementioned terms at $2^{\circ} N$, $58 km$, where the strongest differences occurred. First let us consider case 1.C with the transient QTDW. In the top left panel the force per unit mass due to the divergence of Eliassen-Palm flux shows its minimum occurring just before the QTDW-amplitude in meridional wind reaches its maximum (bottom panel). This time delay can be explained by the behaviour of the

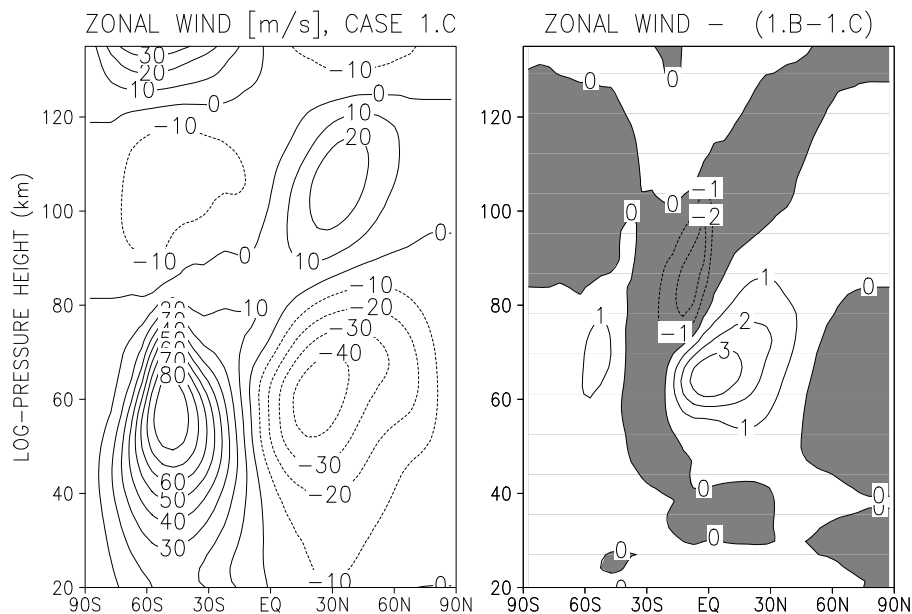


Figure 4.10: Left: Latitude-height cross-section of zonal mean wind for the experiment with transient forced QTDW (1.C). Right: The differences between steady and transient forcing. Values are averaged over days 21-27.

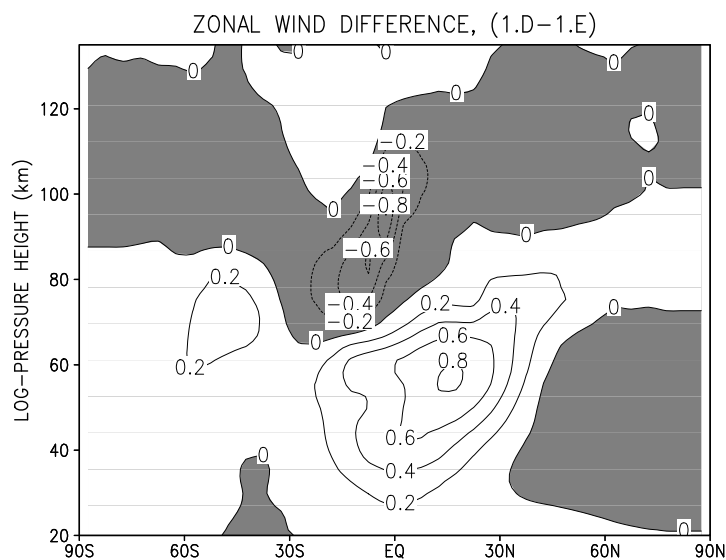


Figure 4.11: Latitude-height cross-section of zonal mean wind difference for the case 1.D and 1.E. Values are averaged over days 18-48.

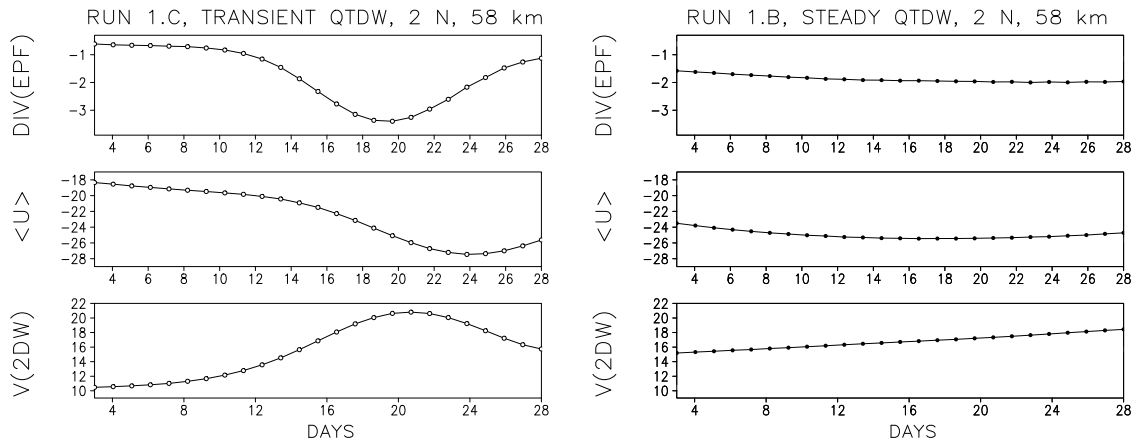


Figure 4.12: Synoptic view of the following parameters for the transient wave (1.C) and steady wave (1.B) experiments. Top panel: acceleration on the mean flow in $ms^{-1}d^{-1}$, middle: zonal mean wind in ms^{-1} , bottom: amplitude of the QTDW in meridional wind in ms^{-1} .

zonal wind amplitude, which amplifies earlier at this height. So the meridional momentum flux $\overline{u'v'}$ as the dominant term in the EP-flux divergence at these coordinates is shifted between the two wind disturbances. The wave exerts a westward (negative) acceleration on the mean flow, which leads to the observed increase in the westward jet strength. The overall view of the QTDW-amplitude of meridional wind and zonal mean wind reveals the increase in the westward jet just after the increase of the QTDW amplitude around July 21. The resulting change in the background flow amounts to $\sim 8 ms^{-1}$ from day 8 to day 24. The amplitude change of the QTDW is $\sim 10 ms^{-1}$. In comparison, the steady forced wave (case 1.B) represented in the right panels of Fig.(4.12), shows only a weak increase in westward acceleration on the mean flow during July ($< 0.5 ms^{-1}d^{-1}$). This results partly from further establishment of the wave and partly from changing background conditions during the progressing season which allow better propagation of the QTDW. Only a small change in the zonal mean wind exists with a typical decrease in the westward jet towards the end of the month. The wave itself undergoes a change of about $\sim 3 ms^{-1}$ under steady forcing.

To summarise, it could be shown, that a transient QTDW exerts a stronger acceleration on the mean flow than the forcing with a steady wave. The most intense effect of a transient QTDW was found around the equator extending into both hemispheres. If a transient wave is propagating upwards for the first time the change in zonal mean wind amounts to a maximum of $\sim 8-10 ms^{-1}$. In this region the wave attenuates the seasonal change in the middle atmosphere where the sun drives the circulation towards weaker jets in the course of summer. However, if a transient wave is able to establish within 60 days its impact on the mean circulation is strongly reduced because the atmosphere is able to adjust to a regularly amplifying phenomenon. This impact is however itself larger than that of the steady QTDW. On the other hand, in a real atmosphere transient processes may not

reach the level of a balanced interaction between wave and mean flow, thus the processes connected to the primary appearance of disturbances in the middle atmosphere might be more important. These results indicate that some observed features of atmospheric dynamics might be explained not only by the existence of planetary waves but also by their special behaviour in the course of a season.

4.4 Interaction with gravity waves

Gravity waves play a crucial role in the dynamics of the atmosphere. These waves are necessary for the QTDW to be able to propagate upwards into the MLT region.

Listing	Experiment
2.A	run with steady forced QTDW using only Rayleigh friction
2.B	run with steady forced QTDW and increased GW amplitudes
2.C	run with steady forced QTDW and decreased GW amplitudes

Table 4.2: Overview of the experiments.

The way in which the gravity waves and their impact on the mean circulation are parameterised is described in detail in Appendix A. Gravity waves are responsible for the wind reversal at mesopause heights as shown in Fig.(C.5). The imposed eastward acceleration on the summer westward jet leads to a meridional circulation, which in turn causes upwelling at the summer mesopause and downwelling at the winter mesopause, leading to the temperature anomaly in polar mesopause heights.

In order to show the importance of gravity waves in middle atmosphere dynamics a numerical experiment (2.A) was carried out using Rayleigh friction only. The derived zonal mean wind and temperature are depicted in Fig.(4.13) and should be compared with Figs.(C.5) and (C.4). Both jets reach values of up to $\pm 130 \text{ m s}^{-1}$ and no wind reversals appear at mesopause heights. The jets are only closed due to strongly increased Rayleigh friction at the upper boundary. The polar summer mesopause temperature in the bottom panel of Fig.(4.13) is $\sim 30 \text{ K}$ higher than in Fig.(C.4).

The very strong westward jet prevents the QTDW from propagating upwards. Fig.(4.14) shows the highly different amplitudes of the QTDW, peaking at much lower altitudes and decelerating in the mesosphere. If the winds are slowed down under the inclusion of the gravity wave parameterisation the QTDW is able to propagate higher because their critical line, where the zonal mean wind matches the wave's phase speed, rises or even vanishes. In this fundamental way, through decelerating the mesospheric jets and imposing a reverse circulation, gravity waves provide a vertical path for planetary waves.

However, gravity waves are in turn influenced by planetary oscillations such as tides and planetary waves. Fig.(4.15) depicts on the left side the acceleration and heating rate

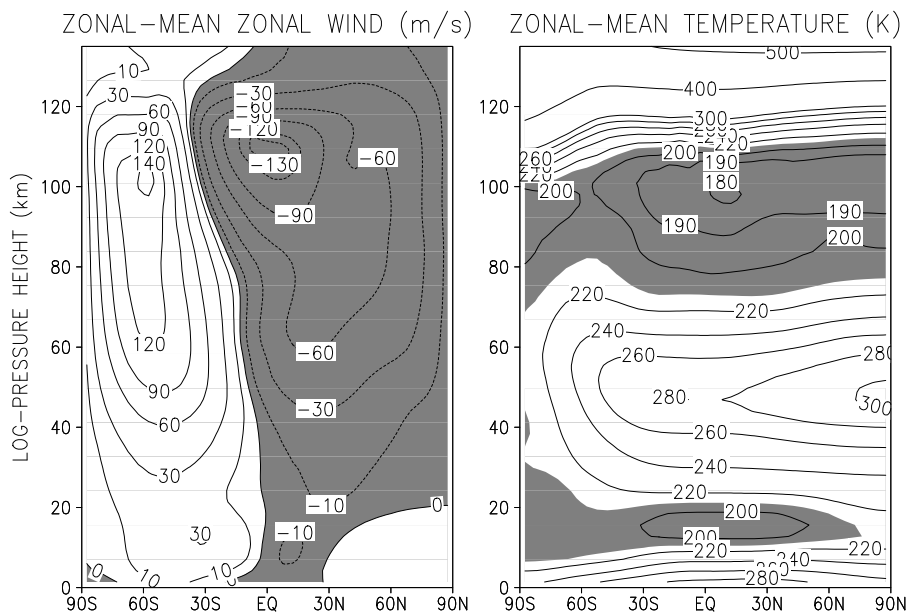


Figure 4.13: July mean of zonal wind and temperature under exclusion gravity waves.

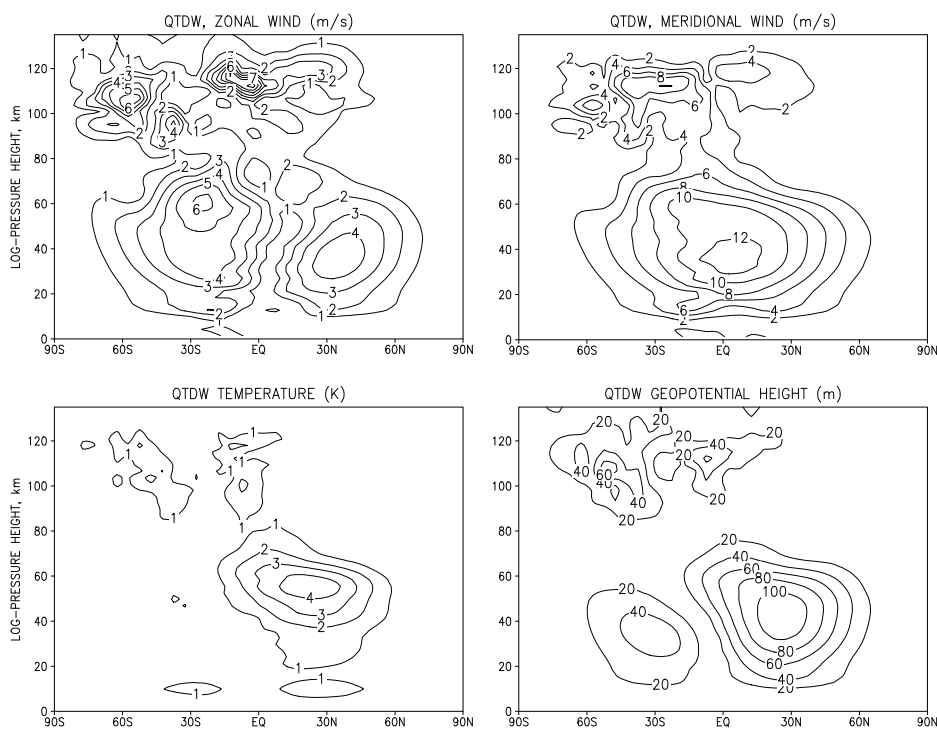


Figure 4.14: Amplitudes of QTDW forcing using Rayleigh friction only.

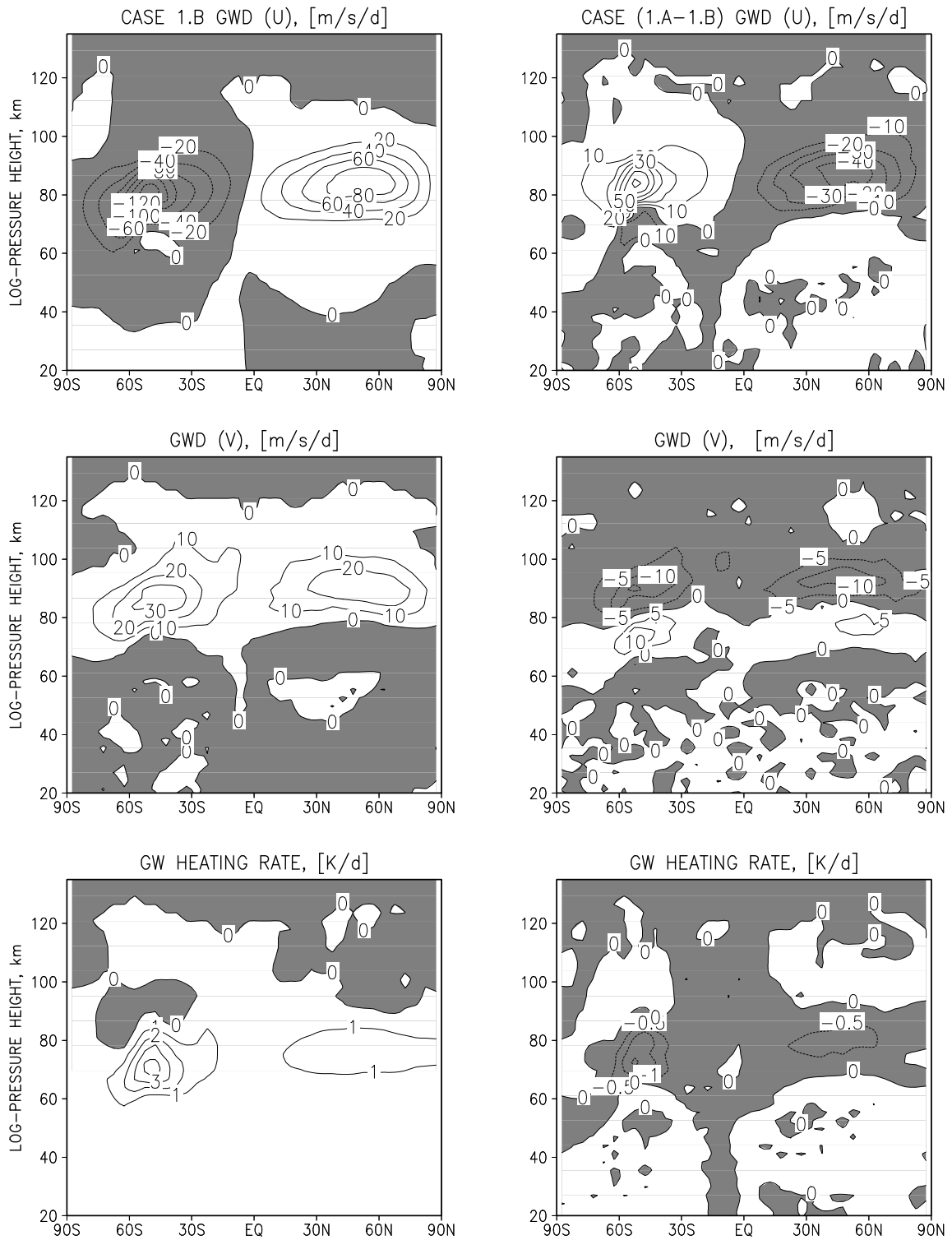


Figure 4.15: Left side: Acceleration and heating rate due to breaking gravity waves for case 1.B. Right side: differences between case 1.A and 1.B. Note, that COMMA-LIM day 120 is applied, i.e. after the establishment of tides and QTDW.

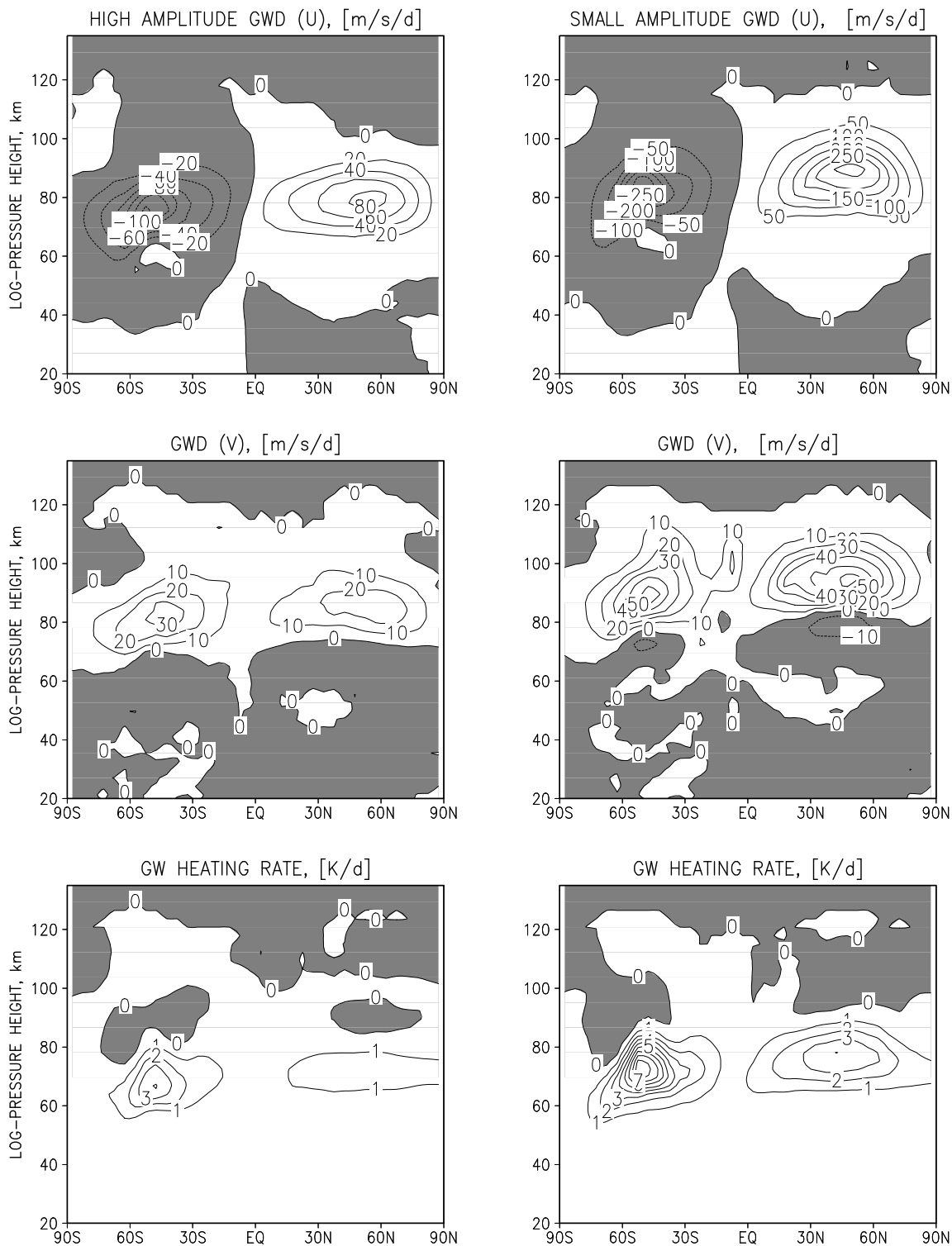


Figure 4.16: Acceleration and heating rate due to breaking gravity waves for case 2.B (left) and 2.C (right). Please note, that COMMA-LIM day 120 is applied, i.e. after establishing of tides and planetary waves.

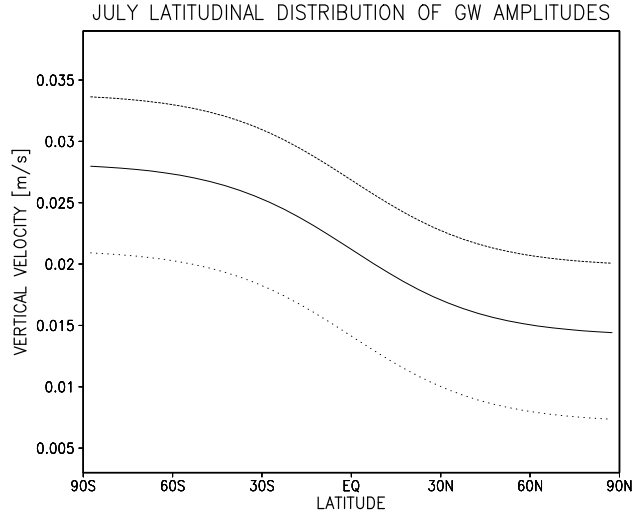


Figure 4.17: Latitudinal distribution of July-mean gravity waves for case 1.A (solid line), case 2.B (short dashed line) and case 2.C (dotted line), averaged over 6 waves with different phase speeds. Amplitudes are given in terms of vertical velocity. Please refer to Appendix A for further explanation.

due to GWs on day 120 of COMMA-LIM calculations (experiment 1.B). The right side presents the differences between the control run (1.A) and the steady forced QTDW. The plots show, that the QTDW leads to a striking increase of GW-acceleration and heating rate. Thus, the westward acceleration the QTDW imposes on the mean flow causes a larger GW induced acceleration. In this way GWs grow at the expense of the QTDW. Please note, that the drag is generally smaller than in Fig.(A.2) because the tides on day 120 reduce the GW related acceleration.

Further investigations into the influence of GW drag on both the mean flow and the QTDW used GW-amplitudes of different strengths (2.B and 2.C). While the standard amplitudes of the gravity waves have on average a speed of $\sim 2.1 \text{ cm s}^{-1}$ at the equator (see Fig.(4.17)), the large-amplitude GWs were forced with $\sim 2.7 \text{ cm s}^{-1}$ and the small-amplitude GWs were set to a speed of $\sim 1.5 \text{ cm s}^{-1}$. Note that these are mean values since the amplitudes of the gravity waves vary according a spectrum formula (see Appendix A). The sources of gravity waves are assumed to be topography, convection, generation due to wind shears or frontal processes. Since the latter three sources change as the weather changes in the troposphere this must have an effect on the size and distribution of breaking gravity waves in the mesosphere. However, climatological values for amplitudes and distribution of gravity waves as used in our parameterisation are not able to simulate the highly variable situation under which gravity waves are generated. Therefore, two experiments of large and small sized GW amplitudes were carried out as examples in order to study how the atmosphere might react to the different possible conditions.

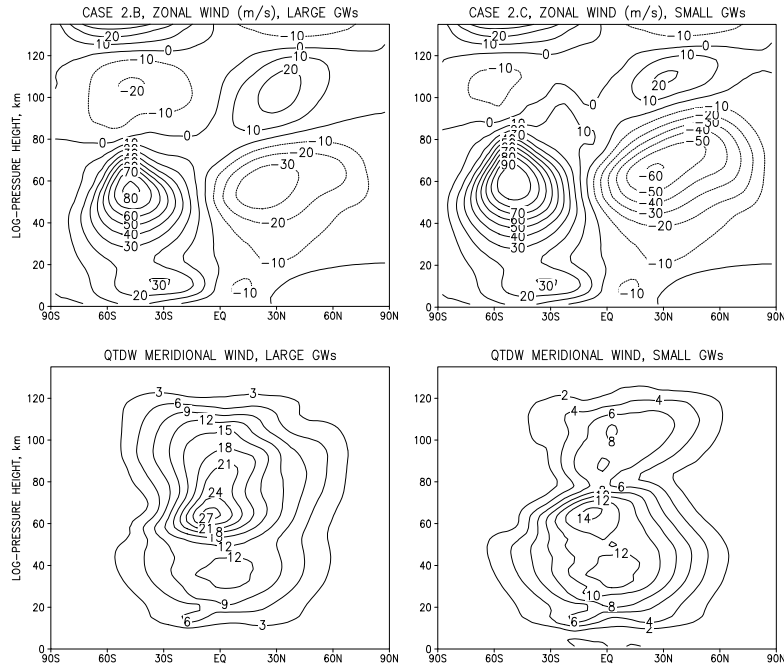


Figure 4.18: Top panels: July mean of zonal wind for small- and high-amplitude gravity waves. Bottom panels: the subsequent QTDW amplitudes of the meridional wind component.

Fig.(4.16) shows the GW induced drag for experiment 2.B and 2.C. The larger the GW-size at the excitation level, the lower the heights of which the gravity waves reach their critical size and break. On the other hand, small GW-amplitudes cause very high propagating gravity waves that have a minimal effect on the mean flow in the mesosphere. The increased jets lead in turn to stronger acceleration if the waves break higher in the lower thermosphere. An increase in GW activity leads to weaker easterlies at low latitudes near the stratopause. These changes in the general circulation near the equator modify QTDW-propagation conditions into the northern hemisphere MLT. Fig.(4.18) shows the zonal mean wind and the meridional wind amplitudes of the QTDW for the two experiments. Case 2.B leads to strongly reduced jets allowing the QTDW to penetrate higher into the MLT region. The vertical propagation of the QTDW for case 2.C stops at altitudes where the easterly jet core exceeds values of 60 m s^{-1} which is approximately the phase speed of the QTDW at mid-latitudes.

The role of gravity waves in connection with the QTDW was studied by Norton and Thuburn (1996, 1999), as mentioned in chapter 2. In their study, the QTDW developed self-consistently in the mesosphere and lower thermosphere due to the insertion of a gravity wave parameterisation. However, the key process in the UGAMP GCM was thought to be barotropic and baroclinic instability evolving at the jet shear zones formed by breaking gravity waves. In COMMA-LIM a QTDW developing from instabilities was not obtained

in the latter numerical experiments, nevertheless, unstable stages of the middle atmosphere as a precondition for a mesospheric QTDW will be a separate subject of investigation.

In conclusion, it has been shown, that gravity waves play an important role in the propagation conditions of the QTDW. Gravity waves provide the path for its upward propagation, even if the wave will transfer energy to the smaller scale waves during its propagation. Additionally, due to the highly variable nature of their generation GWs might be responsible for transient-like amplitudes of the QTDW. The experiments also revealed the still existing gaps of knowledge and numerical capability which are needed in order to realistically describe the gravity waves in the middle atmosphere.

4.5 Interaction with other planetary waves

The theory of a non-linear coupling between two planetary waves or a planetary wave and tides says that two "primary" waves can interact through the advection terms in the momentum equation and produce a family of "secondary" waves (Teitelbaum and Vial, 1991). For instance, if a signal consisting of two cosine waves with zonal wave numbers and frequencies (k_1, σ_1) and (k_2, σ_2) pass through a quadratic system, the output of this system will contain the secondary waves $(2k_1, 2\sigma_1), (2k_2, 2\sigma_2), (k_1 + k_2, \sigma_1 + \sigma_2), (k_1 - k_2, \sigma_1 - \sigma_2)$. The strongest secondary waves are those whose frequencies are the sum and difference of the frequencies of the primary waves. The secondary waves then beat with the primary waves and modulate the amplitude of the higher-frequency wave at the period of the lower-frequency wave.

Listing	Experiment
3.A	run with steady forced QTDW and SPW1 as in case 1.B
3.B	run with steady forced QTDW and 16DW
3.C	run with steady forced QTDW and 10DW
3.D	run with steady forced QTDW and 5DW
3.E	run with steady forced QTDW but without SPW1

Table 4.3: Overview of the experiments.

As mentioned in chapter 2, Jacobi et al. (1998) and Pancheva et al. (2000) among others, reported on observations, which confirmed this theory, especially in connection with the QTDW. Therefore, COMMA-LIM was used to study possible interactions of the QTDW and other planetary waves. The aim was to determine the size of contribution of the coupling processes to the observed QTDW amplitude variations. Experiment 1.B was used to investigate the interaction between the QTDW and (SPW1).

Three additional experiments were carried out, each forced with different planetary waves (16DW, 10DW and 5DW). The long-period PWs and QTDW were switched on

Interaction	Wave number of secondary PW ($k_{sPW} = k_1 \pm k_2$)	Period of secondary PW (h) ($1/T_{sPW} = 1/T_1 \pm 1/T_2$)	Spectral analysis (h)
<i>QTDW</i> +SPW1	4	-52.5	51.2
<i>QTDW</i> -SPW1	2	-52.5	53.9
<i>QTDW</i> +16DW	4	-45	46.5
<i>QTDW</i> -16DW	2	-61	-
<i>QTDW</i> +10DW	4	-42.3	42.6
<i>QTDW</i> -10DW	2	-69	68
<i>QTDW</i> +5DW	4	-39.3	39.4
<i>QTDW</i> -5DW	2	-79	-

Table 4.4: Secondary waves arising from the sum and the difference of the primary waves. The negative or positive sign at the period corresponds to westward or eastward propagating waves, respectively.

after day 90 and after the settling time of 30 days the model begins to simulate the course of July. The methods of wave analysis were the same as those for the QTDW. Table (4.4) lists the main secondary waves arising from interaction of the QTDW with the subsequent PWs. Together with the estimated periods the results from a power spectrum using a fast Fourier Transformation are listed. It was found, that secondary PW signals arising from interaction with the 16DW and 5DW are either small or not detected. This result was confirmed when the amplitudes of possible secondary waves were calculated.

The listed secondary waves arising from the sum and the difference of the primary waves are plotted in Figs.(4.19) and (4.20). Using the method of least squares the frequency that gives the largest feedback signal in amplitude was chosen. The strongest response resulted from the interaction between the QTDW and SPW1 and the waves arising from QTDW/10DW interaction. Wave number 2 shows always stronger signals than wave number 4. The secondary $k = 2$ SPW-wave resembles the shape of the QTDW, and also shows stronger amplitudes for the meridional wind than for the zonal wind. For all other waves both wind fields have the same order of magnitude. Similar experiments were performed with a 2D linearised model (Pogoreltsev et al., 2002). However, in this experiment the selected planetary waves were forced with different frequencies and amplitudes at times 3 times stronger than in COMMA-LIM. All these factors make it difficult to draw comparisons. Qualitatively, the authors also obtained the strongest signal for the 10DW-interaction but did not carry out investigations into stationary planetary waves.

Modulation of QTDW by 16DW and 10DW

Fig.(4.21) shows the results of experiments 3.B and 3.C. In the top panels the modulation in the meridional wind field of the QTDW by the 16DW in the mesosphere and thermosphere is displayed for two different latitudes. This picture is obtained by taking

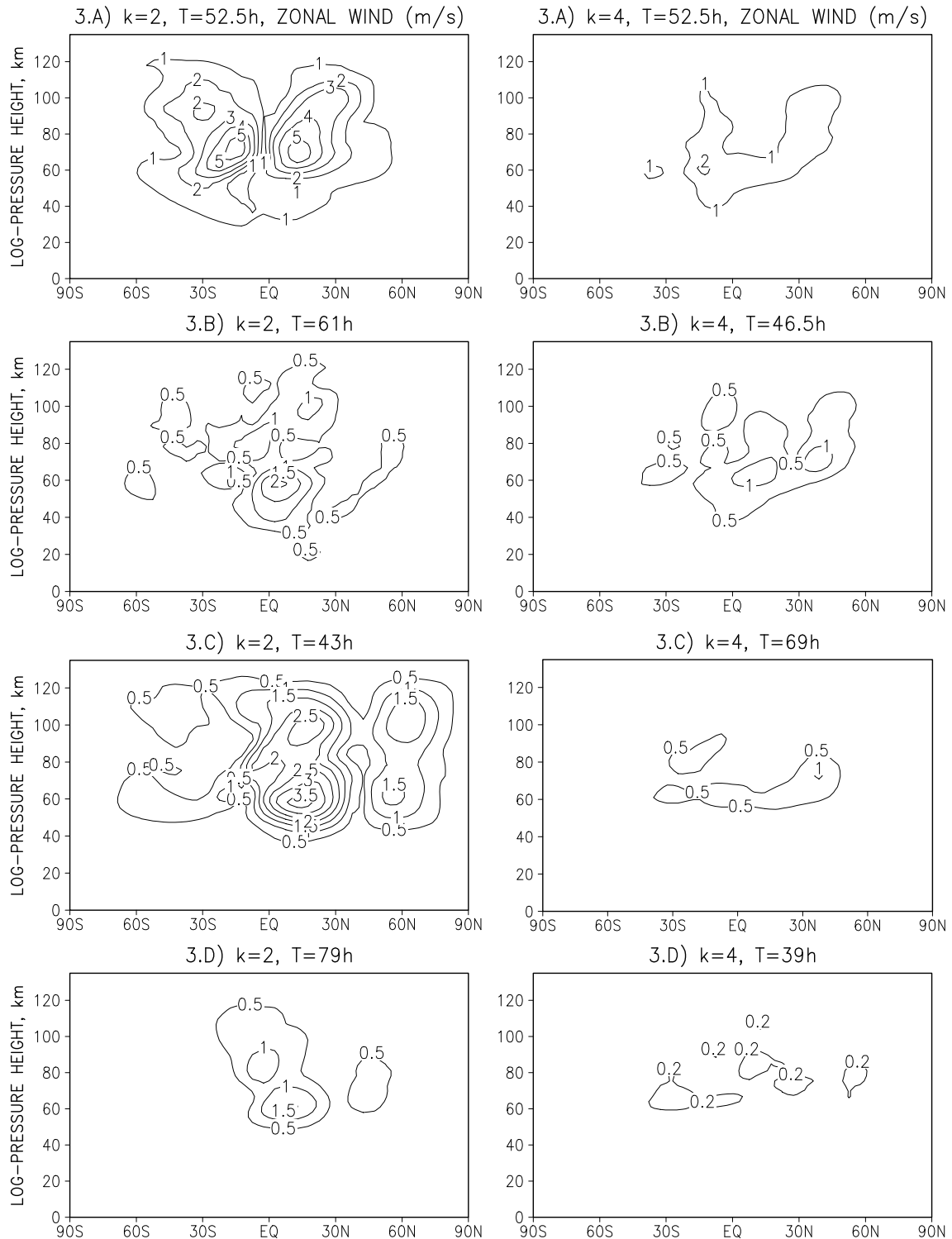


Figure 4.19: Zonal wind amplitudes of secondary planetary waves due to interaction of different planetary waves and QTDW. Left panels represent waves with $k = 2$: 3.A) QTDW-SPW1, 3.B) QTDW-16DW, 3.C) QTDW-10DW, 3.D) QTDW-5DW. Right panels show waves with $k = 4$: 3.A) QTDW+SPW1, 3.B) QTDW+16DW, 3.C) QTDW+10DW, 3.D) QTDW+5DW.

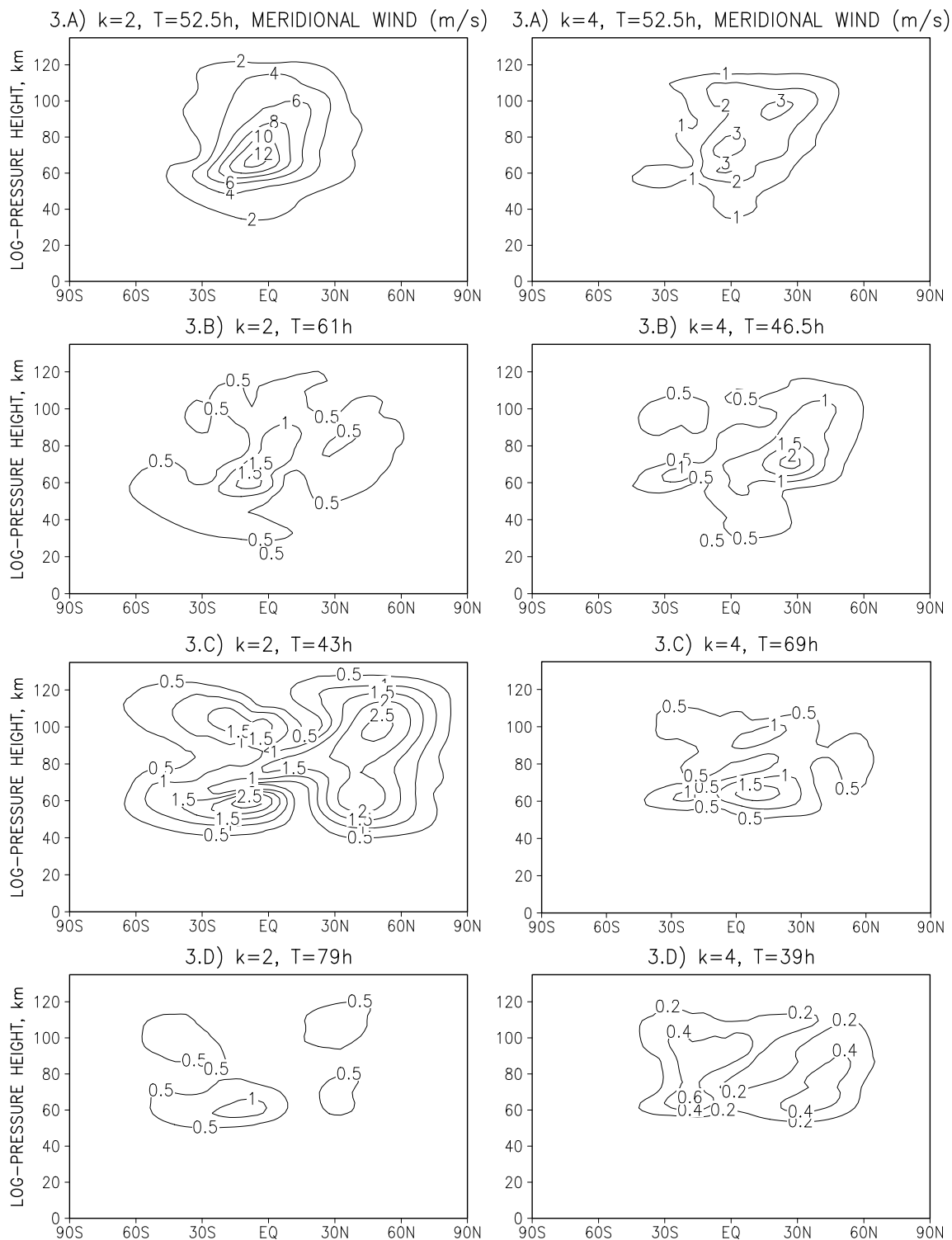


Figure 4.20: As in Fig.(4.19) but for meridional wind amplitudes.

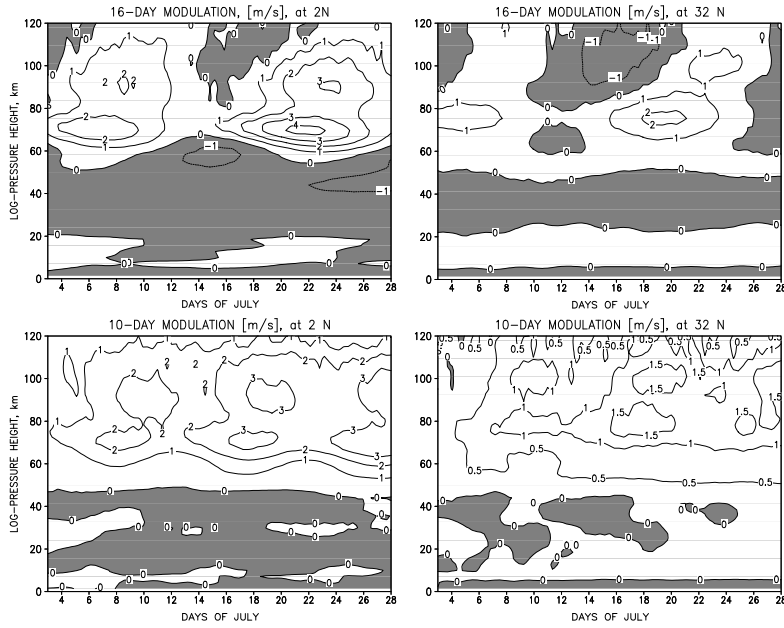


Figure 4.21: Top panels: time-height plot of modulation of the QTDW by the 16DW. Bottom panels: Modulation by the 10DW. Amplitudes of meridional wind are displayed near the equator (left) and mid-latitudes.

the difference between experiment 3.A and 3.B. The variation in the zonal wind field at $32^{\circ} N$ accounts for $1.5 m s^{-1}$ (not shown here) representing an $\sim 20\%$ change, whereas the meridional component is modulated strongest at the equator with around $4 m s^{-1}$ (referring to an 8% change). The strength of modulation decreases towards the north pole at mesospheric heights. Furthermore, increasing modulation in the course of July can be seen. Thus, these are mechanisms that could be responsible for transient-like behaviour of the QTDW if not for burst-like events. However, COMMA-LIM results showed a weaker modulation than that reported by Pancheva et al. (2000). In their study the variation of wave amplitudes exceeded 400% between minimum and maximum. Additionally, in observations by Pancheva et al. (2000) the QTDW seemed to grow through the interaction with the 16DW, whereas in COMMA-LIM the 16DW-modulation results in smaller amplitude values than those for the controlled QTDW (positive differences between control and modulated QTDW). Similar results are obtained for the modulation of the QTDW by the 10DW. The modulation begins also at around $60 km$ height where the winter planetary waves penetrate into the summer hemisphere and is comparable in magnitude and latitudinal decrease of modulation.

Interaction of QTDW and SPW1

Strong secondary waves arised from interaction of these two waves (3.A) as shown in the top panels of Figs.(4.19) and (4.20). Especially the wind amplitudes of wave number 2 show values that reach of about 50 % of the original QTDW, and the structure looks similar

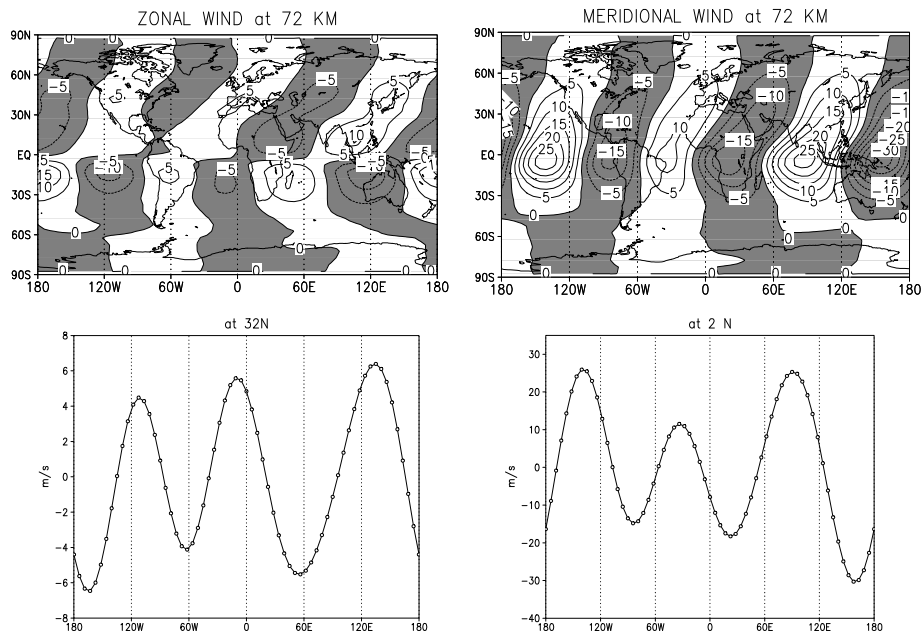


Figure 4.22: Superposition of wave numbers 2, 3 and 4 with period of 52.5 h for zonal (left) and meridional (right) wind. Upper panels show a longitude-latitude section at 72 km , whereas lower panels depict the sum at a specific latitude.

to the primary QTDW. It was proved if the $k = 2$ QTDW arises from interaction with the stationary planetary wave and not as a sub harmonic of the diurnal tide by carrying out a separate calculation without the SPW1 (experiment 3.E). Then, such waves did not arise. Furthermore, the very weak response of the self-interacting DT exhibits a different shape from the $k = 2$ -QTDW. Wave number 4 is not as strong but still more pronounced than other secondary PWs. A further interesting feature of experiment 3.E is that the QTDW forced without the presence of a SPW1 exhibits amplitudes of the same magnitude as in case 3.A. This means that an existing SPW1 delivers the main part of energy to the secondary two-day waves. Under this assumption transient events of SPW1 will increase the secondary wave amplitudes. The secondary QTDWs indicate that it seems necessary to take them into account when comparing the QTDW with radar measurements. Local measurements are only able to collect the frequency but cannot account for different wave numbers of the observed oscillations or divide them into parts of primary and secondary waves.

By restoring the three waves back to the longitudinal grid the superposition of the waves with equal frequency but different wave number and amplitude shows a wave with the wave number of the strongest amplitude, see Fig.(4.22). The longitude-latitude plots show that the wave number changes to 2 in the high-latitude winter hemisphere; however, there the QTDW amplitudes are smaller than $5 m s^{-1}$. Nevertheless, regarding this picture

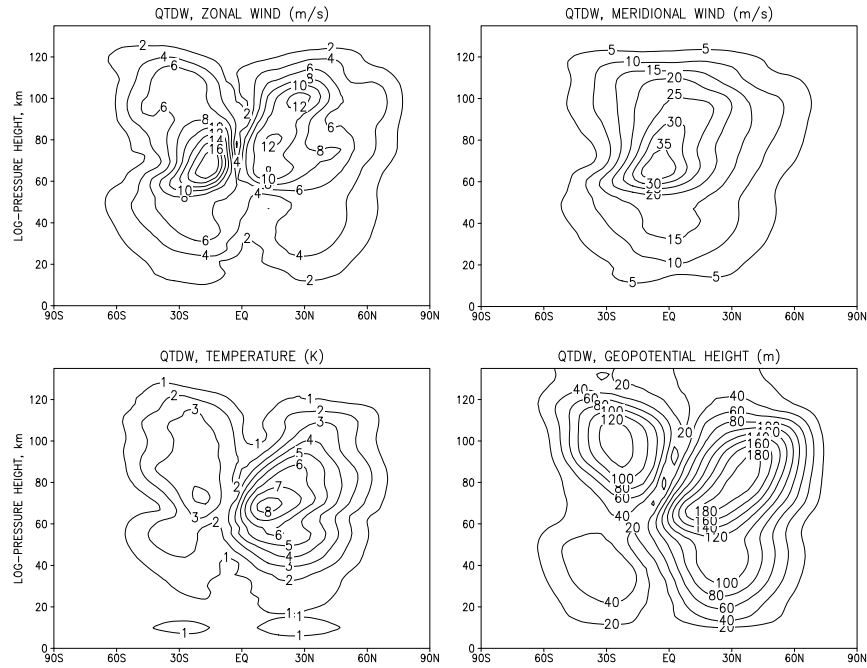


Figure 4.23: Amplitudes of QTDW as in Fig.(4.2) but as the sum of wave numbers 2-4 with period of $52.5 h$.

it seems possible that the wave number can change at specific latitudes or altitudes if one of the secondary waves grows stronger than the primary QTDW. The characteristic feature of the not equally distributed distance between two ridges over the latitudinal circle develops due to beating between the three waves. In the bottom panels of Fig.(4.22) a clear example is given for the wind amplitudes at $32^\circ N, 72 km$ height. Wave number estimation from radar stations at different longitudes would yield in this case a non-integer wave number as was the case in the papers by Poole and Harris (1995) and Meek et al. (1996). The authors of these papers suggested that beating of waves might be responsible for wave number ambiguities. COMMA-LIM model investigations could confirm this assumption and explain it by taking into account the SPW1-QTDW interaction. Fig.(4.23) shows the sum of the waves (wave number 2 to 4) with the same period $52.5 h$, on a latitude-height cross-section. The amplitude increased at about 60% in zonal and meridional wind amplitudes when compared with the wave number-3 part alone (see also Fig.(4.2)).

To summarise, the interaction of the QTDW with other PWs leads to significant amplitude modulations of the quasi two-day wave and a number of secondary PWs arise. The SPW1 seems to play the most important role in these non-linear interactions since the developing secondary PWs have the same period as the primary QTDW. Thus, radar data from a single station that cannot distinguish between the wave numbers may observe increased QTDW amplitudes at a time, where the SPW1 shows a transient behaviour.

4.6 Interaction with tides

Several authors reported on phase locking of the 48 h -QTDW to the local time, preferably at noon, e.g. Craig and Elford (1981), Clark et al. (1994), Jacobi et al. (1997). They suggested an interaction of the QTDW with the tides that might lead to the observed feature. However, this phase locking needs a rather exact two-day wave to be observed or analysed, which is not the case for the COMMA-LIM wave. Nevertheless, tides can be modulated by the QTDW and secondary waves may arise even if no phase locking occurs. Such features are the appearance of the 16 h -oscillation as well as a 9 h -oscillation which were observed on times, when the QTDW was active (e.g. Harris and Vincent (1993) or Thayaparan et al. (1997)). Former model results from Palo et al. (1999) investigating the QTDW-tidal interaction gave reduced tidal amplitudes in the order of about 50% for the diurnal tide and a $\sim 40\%$ reduction for the semidiurnal tide. In their analysis of secondary planetary waves the sum of QTDW and semidiurnal tide with wave number 5 and period $T = 9.6 h$ showed the strongest response. Maximum amplitudes in this particular zonal wind perturbation reached $18 m s^{-1}$.

Listing	Experiment
4.A	as case 1.A, but 2-hourly output
4.B	steady forced QTDW as 1.B, with 2.hourly output

Table 4.5: Overview of the experiments.

This study investigates how the QTDW interacts with tides. In order to resolve the tides and possibly secondary waves a control run (4.A) is compared with the steady forced QTDW-run (4.B) with an output of every 2 hours instead of 4 hours.

The upper 4 panels of Fig.(4.24) show the amplitudes for both horizontal wind components for the diurnal tide together with the percentage change due to the QTDW. The lower 4 panels depict the amplitudes of the semidiurnal tide and their QTDW-changes. The QTDW leads to dominantly decreasing amplitudes in a range of about 5 – 15% in case for the DT and up to 8% for the SDT. There also exist confined regions, where the tides are larger if a QTDW is present. However, regions exceeding values of $\pm 5\%$ changes are very small. The meridional component is more affected than the zonal one, which is in accordance with larger north-south wind amplitudes of the QTDW. The absolute values of changes are smaller as in Palo et al. (1999) but in their study the January-QTDW was almost 3 times stronger than the COMMA-LIM July-QTDW.

Table(4.6) lists the secondary waves arising from sum and difference between QTDW and DT and QTDW and SDT, respectively. Fig.(4.25) shows the secondary waves due to interaction between the QTDW and the tides in the zonal wind field. The strongest response gives the 16 h - oscillation with maximum values in the zonal wind of about $9 m s^{-1}$, the weakest amplitude shows the wave number 5-wave due to QTDW+SDT interaction.

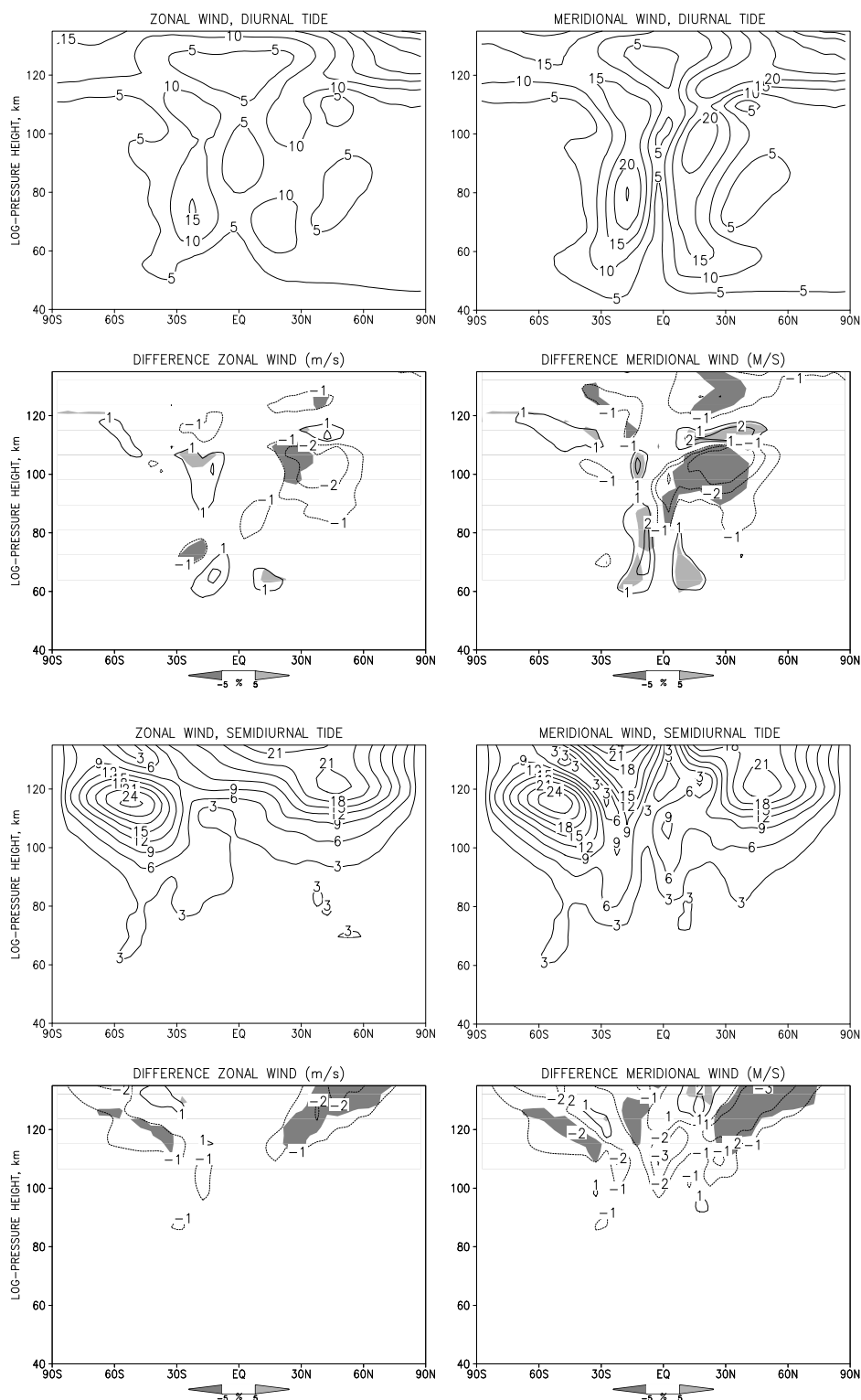


Figure 4.24: Top panels: diurnal tide amplitude for zonal (left panel) and meridional wind obtained from control run. Below: Difference between experiment 4.A and 4.B for the upper amplitudes. Shaded regions indicate changes stronger than $\pm 5\%$. Bottom panels: The same investigations but for the semidiurnal tide.

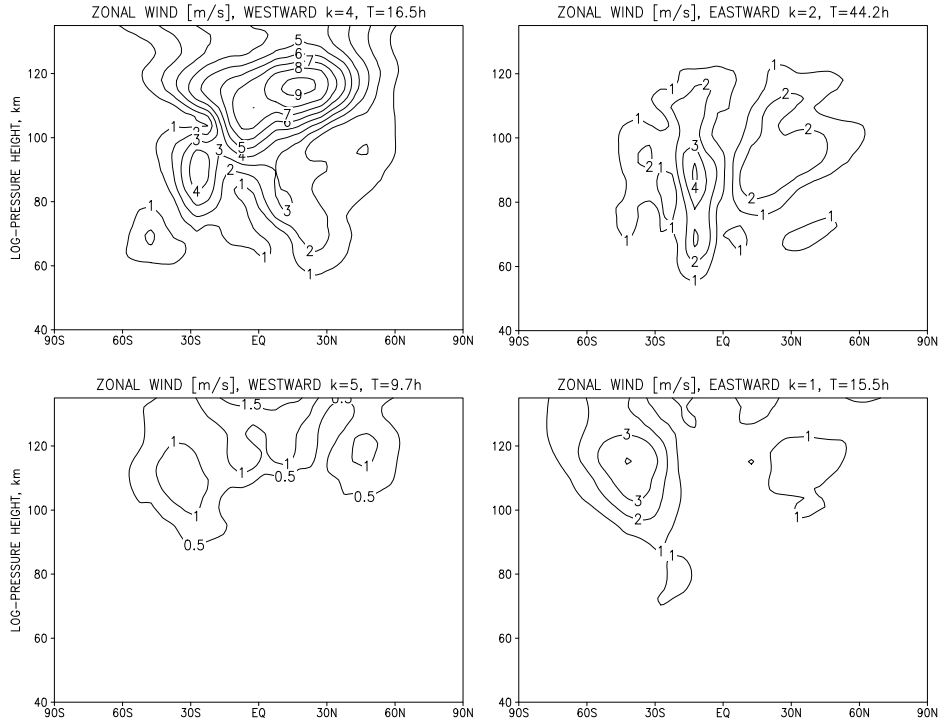


Figure 4.25: Top panels: Secondary planetary waves amplitudes for zonal wind arising from interaction of diurnal tide and QTDW. Bottom panels: waves due to semidiurnal tide and QTDW interaction. See also table 4.6. Note, that the lower boundary has been raised for convenience.

Interaction	Wave number of secondary PW ($k_{sPW} = k_1 \pm k_2$)	Period of secondary PW (h) ($1/T_{sPW} = 1/T_1 \pm 1/T_2$)	Spectral analysis (h)
<i>QTDW</i> +DT	4	-16.47	15.5
<i>QTDW</i> -DT	2	44.2	44.5
<i>QTDW</i> +SDT	5	-9.7	9.7
<i>QTDW</i> -SDT	1	15.5	15.5

Table 4.6: Secondary waves arising as the sum and the difference between the QTDW and diurnal or semidiurnal tide, respectively. The negative or positive sign at the period corresponds to westward or eastward propagating waves.

Except this latter oscillation the results obtained by Palo et al. (1999) (see there Fig.(8)) compare quite well with COMMA-LIM results for both " $DT \pm QTDW$ "- waves and for the eastward propagating $15.5 h$ wave. This is surprising because the QTDW forced in the TIME-GCM delivered amplitudes of about $50 m s^{-1}$ for the zonal wind and $\sim 80 m s^{-1}$ for the meridional wind. However, tidal amplitudes are comparable with COMMA-LIM tides. Thus, our results indicate that for the latter three waves the tides provide the dominant energy, but the QTDW is more responsible for feeding the $k = 5$ wave.

4.7 Influence of the 11-year solar cycle on the QTDW

Since solar radiation is the driving force of atmospheric dynamics, changes of the solar energy input should be accompanied by a climate response. However, observations of solar induced atmospheric changes, that have to separate competing effects on the atmosphere, do not agree up to now with numerical model results. If the observational data are accepted to be correct numerical simulations underestimate the observed solar response of the (middle) atmosphere. It has been shown that radiative forcing alone can account only for a part of the signal. So additional coupling mechanisms between radiation, dynamics and chemistry must be responsible. Planetary waves are thought to play an essential role in these processes. During their vertical propagation these waves interact with the background flow and reallocate energy and momentum in the middle atmosphere. Data analyses (Labitzke and van Loon, 1988) suggested stronger planetary wave activity during solar maximum conditions when the Quasi-Biennial-Oscillation (QBO) is in its western phase (eastward winds). During their eastern phase however, planetary waves were stronger under solar minimum conditions. It is important to note, that in their study winter data were analysed in connection with planetary wave activity. First numerical investigations (Arnold and Robinson, 1998, 2000) confirmed these results qualitatively. Jacobi (1998) also found from wind measurements at the mid-latitude mesopause region a positive correlation between solar activity and quasi two-day wave activity during northern summers but he found no relations to the phase of QBO.

Listing	Experiment
5.A	control run under solar maximum conditions
5.B	control run under solar minimum conditions
5.C	run with steady forced QTDW under solar maximum conditions
5.D	run with steady forced QTDW under solar minimum conditions

Table 4.7: Overview of the experiments.

The question raised, what response the zonal mean circulation and the QTDW in COMMA-LIM give to changes due to solar variability.

Absorption bands	Range of wavelength	Applied variation (%)
EUV - Extreme		
ultra violet	< 120 nm	± 20
Lyman- α	121.6 nm	± 36
Schumann-Runge-Continuum I	125 – 152 nm	± 13
Schumann-Runge-Continuum II	152 – 175 nm	± 8
Schumann-Runge-Band	175 – 205 nm	± 4
Herzberg-Bands	205 – 245 nm	± 3
Hartley-Bands	200 – 300 nm	± 2

Table 4.8: Applied variations to the radiation routine, after results by Rottmann (1999).

Simulation of the 11-year solar cycle

The variation of total solar irradiance over 11 years strongly depends on the wavelengths with a dramatic increase towards shorter wavelengths. The total variation of the solar constant accounts only for 0,1% but to this variation the solar ultra violet (UV) radiation below 300 nm contributes up to 14% (Fligge et al., 2001). This UV-radiation is absorbed in the middle atmosphere by molecular and atomic oxygen and ozone in different absorption lines or bands. In order to calculate the heating rates in the model the absorption of solar radiation by the gas components is increased or decreased in the corresponding bands using data from UARS SOLSTICE instrument (Rottmann, 1999), see also table (4.8).

The increased/decreased radiation leads to a variation in ozone content of about 2% (e.g. Haigh (1994)). This has to be taken into account while using the ozone data, because COMMA-LIM does not include a self-consistent ozone calculation. McCormack et al. (1997) found a latitudinal and seasonal dependence of the total ozone column change in response to the 11-year variation. The reported June/July/August mean was approximated for the COMMA-LIM ozone climatology:

$$C'_{O_3} = (1 \pm (0.026 \exp[-\frac{(\phi - 27.5)^2}{510}] + 0.018 \exp[-\frac{(\phi + 27.5)^2}{510}])) \cdot C_{O_3}, \quad (4.8)$$

where the alternating sign stands for increase and decrease of the ozone concentration and ϕ is the latitude. Fig.(4.26) demonstrates the solar induced change in the total ozone column. Note that a latitudinal variation of ozone even in the small range of 2% leads to a different response of the atmosphere as if a uniformly 2%-variation is applied as, for instance, in Fröhlich and Jacobi (2004). This points to the important role ozone is playing in the middle atmosphere.

In this study the QBO has not been taken into account, rather the equatorial circulation shows easterlies on the summer side and westerlies on the winter side. So one cannot relate this behaviour to one of both possible phases. This may have an effect on the results.

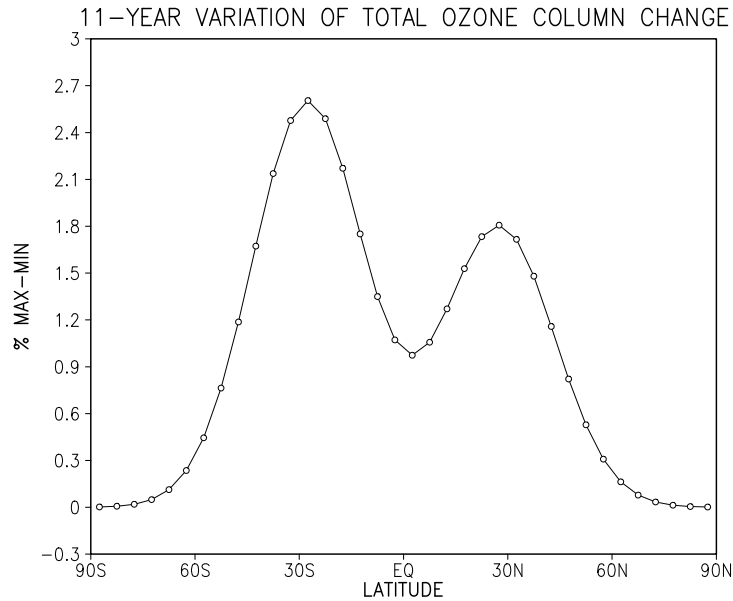


Figure 4.26: June/July/August mean of total ozone column change in response to the 11-year variation in solar UV analytical approximated to the observed solar regression coefficients published by McCormack et al. (1997). Note, that the peak value of 2.6% has an $\pm 2\sigma$ uncertainty of $\pm 1.1\%$.

In order to get an idea about the atmospheric response on the 11-year solar variability the first calculations were made without travelling planetary waves (5.A and 5.B). Fig.(4.27) shows difference plots between solar maximum and solar minimum conditions for the zonal wind and temperature field.

The changes in the temperature field due to the solar cycle show everywhere positive values. Considerable temperature variations are found upwards of the level of ozone absorption. The first maximum appears around the equatorial stratopause/lower mesosphere region with a difference of about ~ 3 Kelvin, which results not only from different absorption rates but also depends on the total amount of ozone in the middle atmosphere. The temperature maximum in the winter mesopause region between 70 and 90 km stems mainly from adiabatic heating and heating due to breaking gravity waves. These processes are stronger during solar maximum. The cooling terms like the infrared radiation are also enhanced for solar maximum conditions. Although heating dominates, as can be seen in Fig.(4.28), cooling is responsible for the local minimum at mesopause heights around the equator. At thermospheric heights the differences increase rapidly due to the extreme ultraviolet-radiation absorbing gas components as molecular and atomic oxygen.

The differences in the zonal mean flow between solar maximum and minimum show a cell of positive difference of $> 5 \text{ m s}^{-1}$ at the mid-latitude winter mesosphere. The equator is dominated by negative values but the summer mesosphere exhibits also cell of about

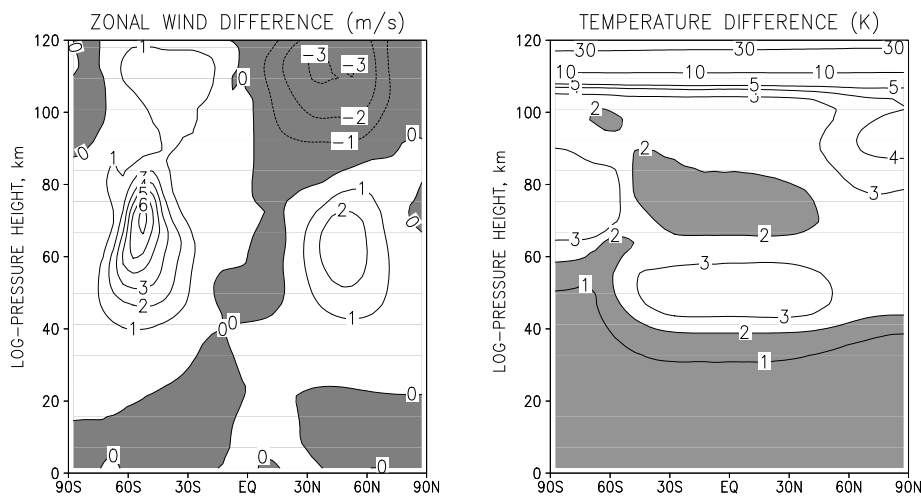


Figure 4.27: Left: Differences between solar maximum and solar minimum conditions for zonal mean zonal wind. Right: the same for the temperature. Negative differences in the zonal wind are dark shaded, temperature changes $< 2K$ are light shaded.

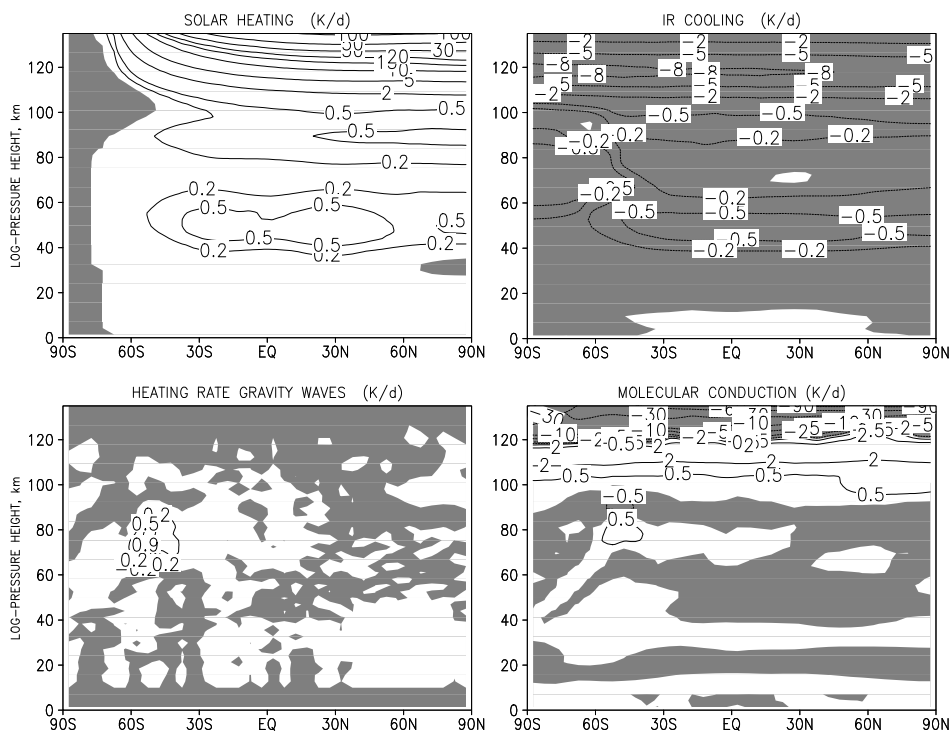


Figure 4.28: Differences between solar maximum and solar minimum for the four heating rate terms contributing to the temperature. Note, the contour intervals are not equidistant in order to highlight the small but important changes.

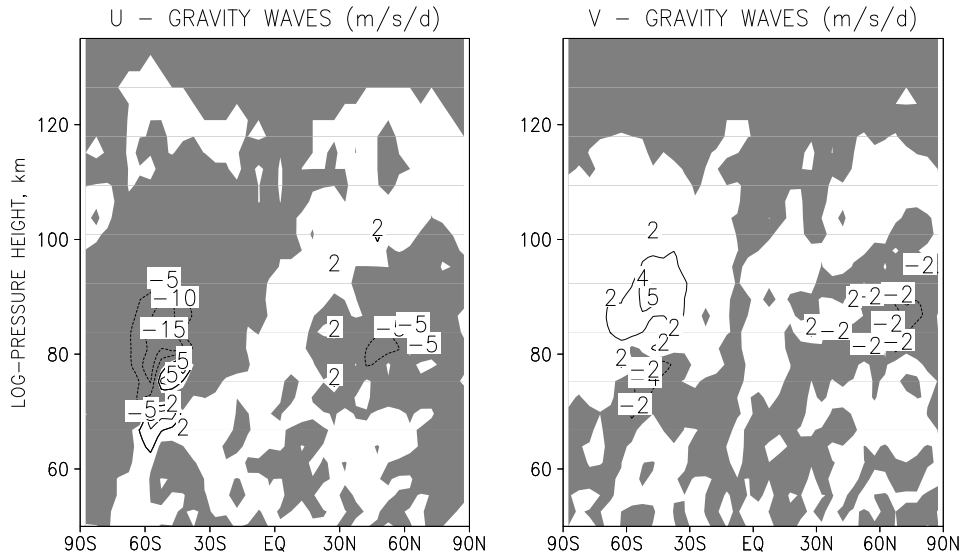


Figure 4.29: Differences between solar maximum and solar minimum conditions for zonal (left panel) and meridional (right panel) acceleration due to gravity wave breaking.

$2 m s^{-1}$ solar induced change. The maximum on the winter hemisphere means an intensification of the jet during enhanced solar activity, whereas in the summer hemisphere it represents a stronger jet during solar minimum conditions. It is important to note, that the ozone variation is responsible for the small equatorial minimum and the positive cell of wind change in the summer hemisphere. Experiments with an equally distributed ozone variation of $\pm 2\%$ throughout the middle atmosphere led to a negative cell in the summer mesosphere indicating stronger easterlies during solar maximum (Fröhlich and Jacobi, 2004). Thus, the positions of local maxima of $\sim 0.5 K/d$ at the stratopause are caused by the ozone distribution. The so induced meridional temperature gradient between mid-latitudes and pole drives the westward jet in the summer hemisphere. At thermospheric heights variations in EUV-bands lead to wind changes that are also stronger during solar minimum conditions. In Fig.(4.29) the solar induced behaviour of the gravity wave drag is shown in the zonal and meridional direction. Negative differences in the winter hemisphere mean stronger acceleration on the mean flow during solar maximum (because the zonal acceleration is directed westward) while in the summer hemisphere acceleration is larger for solar minimum. The same applies for the meridional acceleration due to gravity waves.

The QTDW was then forced under the same conditions as aforementioned (experiments 5.C and 5.D). Fig.(4.30) illustrates the plots of difference of the wave for wind, temperature and geopotential amplitudes. The wave amplitudes do not show a uniform behaviour for the whole middle atmosphere. The wave activity in the mesospheric wind field around the equator is stronger during solar maximum conditions, while negative values in the northern

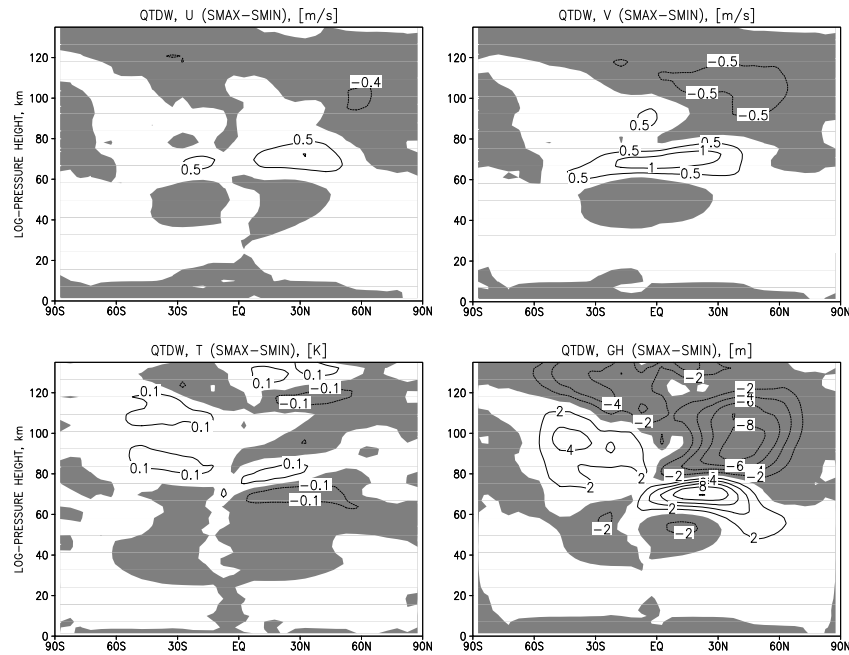


Figure 4.30: Differences of QTDW amplitudes between solar maximum and solar minimum conditions for winds, temperature and geopotential height. Shaded regions indicate weaker propagation during solar maximum conditions.

hemisphere mean better propagation during solar minimum. The weakest signal of change shows the temperature amplitude with $< 5\%$. For the horizontal wind components and the geopotential amplitude the maximum change in amplitude due to the solar cycle accounts for approximately $5 - 10\%$. The question, if planetary waves are able to contribute in a remarkable way to solar induced wind and temperature changes, has therefore to be answered in the negative in the case for the QTDW.

By comparing the results of wind amplitudes at mid-latitude MLT with Jacobi (1998) the results are not in agreement, because the QTDW-activity is smaller during solar maximum conditions. However, at mesospheric heights around the equator the QTDW propagates better for solar maximum conditions. Several reasons may account for this discrepancy: first, the missing QBO, which provides another background circulation. Another possibility is the ozone climatology, its variation in total and its latitudinal distribution throughout the solar cycle. Former studies gave remarkable different results if another data set for ozone or another variation between solar maximum and minimum were applied. Therefore, additional experiments should be carried out, testing what impact the variation of ozone in the range of the $\pm 2\sigma$ uncertainty (McCormack et al., 1997) will have on the propagation conditions for the QTDW.

4.8 Experiments with unstable stages of the atmosphere

It has been shown in several papers and theses, that the QTDW can also be a result of an unstable mesosphere, especially in the summer months when the westward jet reaches its maximum and strong vertical and latitudinal wind gradients arise (e.g. Plumb (1983a); Norton and Thuburn (1996); Limpasuvan et al. (2000); Schröder (2003); Merzlyakov and Jacobi (2004)). Then, the meridional gradient of potential vorticity $\partial\bar{q}/\partial\phi$ becomes negative and provides the necessary condition for an instability to occur. All these authors used different models, ranging from highly simplified dynamical models to global circulation models. While the users of simplified models prescribed appropriate winds, Norton and Thuburn (1996) claimed the necessary role of GWs in an GCM in order to maintain an unstable stage of the zonal mean flow.

Listing	Experiment
6.A	control run for enhanced July conditions
6.B	initial forcing of noise and wave numbers 3 and 4 at 22° N, 65 km
6.C ₁	permanent in situ QTDW forcing at 45° N, 85 km referring to strong vertical wind shear
6.C ₂	permanent in situ QTDW forcing at 22° N, 65 km referring to strong latitudinal and vertical wind shear
6.C ₃	permanent in situ QTDW forcing at 2° N, 60 km referring to strong latitudinal wind shear
6.D	permanent in situ QTDW forcing at 22° N, 65 km with increased amplitude
6.E ₁	permanent in situ QTDW forcing at 22° N, 65 km with numerical diffusion $\varepsilon = 0.07$
6.E ₂	permanent in situ QTDW forcing at 22° N, 65 km with numerical diffusion $\varepsilon = 0.05$

Table 4.9: Overview of the experiments.

At this stage of investigation it can be excluded that under summer conditions with strong wind shears a QTDW forced from the troposphere is able to propagate upwards into the MLT region, whereas under moderate conditions such a process is a reasonable assumption. By considering the activity of planetary waves in the winter hemisphere it turned out, that a QTDW is modulated by the period of a 16DW or 10DW up to 20% of its amplitude or may increase in amplitude up to 60% if the SPW1-QTDW interaction is considered. However, a self-developing QTDW could not be generated until now.

The July climatology of COMMA-LIM, as used in the other experiments, only shows

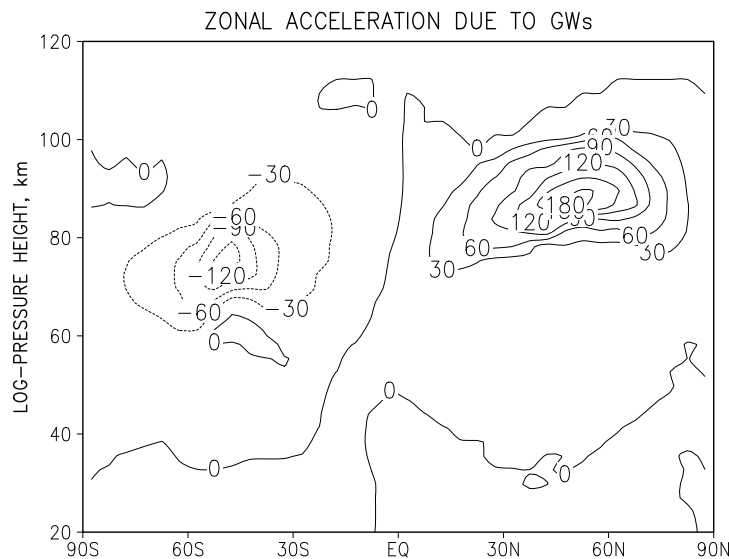


Figure 4.31: Enhanced zonal acceleration on the mean flow due to increased gravity wave activity. July conditions at COMMA-LIM day 90 are applied. Values are given in $m s^{-1} d^{-1}$.

moderate summer jets, as is shown in Appendix C in Fig.(C.5). Under the assumption that an appropriate atmospheric stage will lead to unstable conditions, this wind climatology was compared with the July mean zonally averaged fields as produced by the UGAMP-model (Norton and Thuburn, 1999). The maximum of the COMMA-LIM westward jet reaches $> 40 m s^{-1}$ and is located between $50-70 km$ height, while the UGAMP jet showed $> 60 m s^{-1}$ at the same place. The easterlies in UGAMP extend at $50 km$ farther into the winter hemisphere than in COMMA-LIM. Such an edge of winds might be responsible for inertial and/or barotropic instabilities as they were investigated by Limpasuvan et al. (2000) and Schröder (2003). Furthermore, the gravity wave drag in COMMA-LIM accounts for $\sim \pm 100 m s^{-1} d^{-1}$ in both hemispheres, whereas Norton and Thuburn (1996, 1999) reported on $> 140 m s^{-1} d^{-1}$ of zonal acceleration on the mean flow at the summer side. The spectral resolution of UGAMP of T21 refers to a longitudinal distance of about $\Delta \lambda = 17^\circ$; the mesospheric vertical resolution was $3-4 km$. Assuming that the smallest to be resolved UGAMP-wave needs 3 points to be represented, these parameters have approximately the same resolution as COMMA-LIM. Therefore, COMMA-LIM was subject of several investigations, in order to generate similar conditions as in UGAMP. Tuning the model atmosphere reveals the gaps of knowledge, however, if successful, it helps to understand the dynamical processes on a first step.

An obvious tool for tuning provides the gravity wave drag scheme. As is outlined in the Appendix A the gravity wave amplitudes underlie a latitudinal distribution simulating stronger wave activity in the winter hemisphere than in the summer hemisphere. The larger winter amplitudes lead to faster growing gravity waves, breaking at lower heights as

the summer GWs do. Therefore, the two jets have a different vertical extension. However, simply to increase the GW amplitudes would mean to lower the zonal wind reversal and to exert a too strong deceleration of the jets. Thus, an increase of the latitudinal shear in the GW amplitude distribution with a slight decrease of the GW amplitude was accompanied by doubling the effect of breaking gravity waves on the mean flow. An efficiency factor of GW-momentum deposition was used in former schemes to tune the acceleration of GWs (Jakobs, 1986; Grollmann, 1992) but is substituted (or set to 1) in the current scheme by the insertion of a weak Rayleigh friction that parameterises the loss of energy due to non-linear interaction between the mean flow and waves and waves which are not taken into consideration.

Additionally, a latitudinal distribution was applied to the Rayleigh friction and horizontal turbulent diffusion terms that provide stronger diffusion in the winter hemisphere than in the summer hemisphere. This might be a reasonable assumption as long as not too many additional planetary waves are forced in the winter hemisphere. The vertical \tanh -function of Rayleigh friction (compare with Fig. 3.2) and turbulent diffusion were also raised of about 5 km to 65 km, in order to allow the development of a strong westward jet. The SPW2 was forced in order to maintain the speed of the eastward jet. All changes are listed in table(4.10).

Term	Experiment 1.A	Experiment 6.A
efficiency of GW momentum deposition	1	2
Rayleigh friction	$\beta_r(z) = [1.25 + 0.75 \tanh(\frac{z-60}{20})]10^{-6}$	$\beta_r(z) = [1.25 + 0.75 \tanh(\frac{z-65}{20}) - 0.25 \tanh \frac{\phi-\phi_{EQ}}{9}]7.5^{-6}$
horizontal turbulent diffusion	$K_H(z) = [1.25 + 0.75 \tanh(\frac{z-60}{20})]10^6$	$K_H(z) = [1.25 + 0.75 \tanh(\frac{z-65}{20}) - 0.25 \tanh \frac{\phi-\phi_{EQ}}{9}]7.5^{-6}$
vertical bi-harmonic diffusion smoothing	$BH_z = [1.25 + 0.75 \tanh(\frac{z-60}{20})]10^8$	$BH_z = [0.6 + 0.75 \tanh(\frac{z-65}{20}) - 0.25 \tanh \frac{\phi-\phi_{EQ}}{9}]7.5^8$
stationary PWs	SPW1	SPW1+SPW2

Table 4.10: Overview of the changed parameters. Compare the Rayleigh friction and diffusion terms with Eqs.(3.30,3.26).

The resulting zonal mean flow and its meridional gradient of \bar{q} is plotted in Fig.(4.32) on the right panel. On the left side moderate conditions (1.A) are shown for comparison.

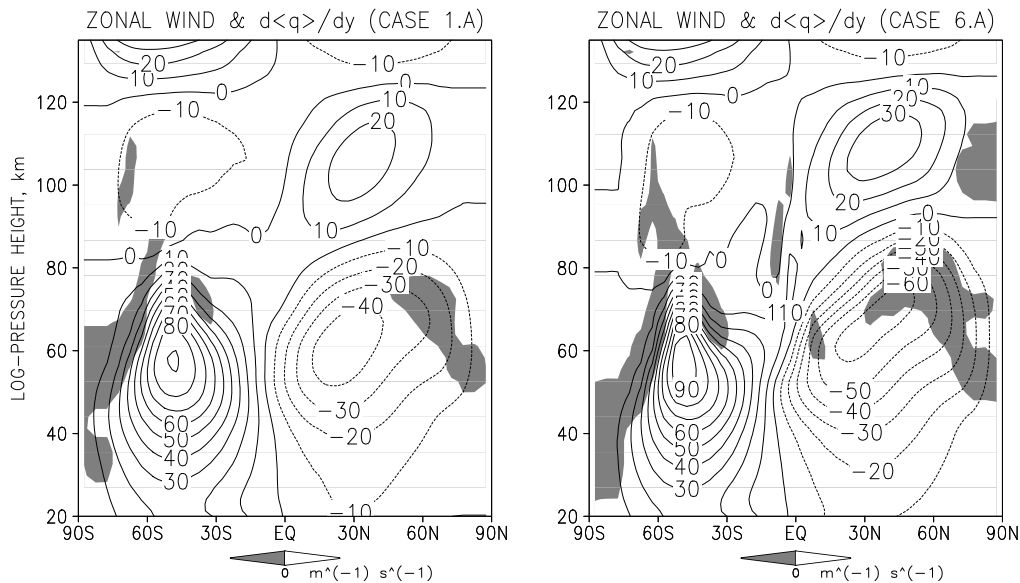


Figure 4.32: Zonal mean flow and shaded the negative meridional gradient of potential vorticity for moderate summer conditions on the right panel and on the left side for enhanced conditions.

There, $\partial\bar{q}/\partial\phi$ is negative only in a small region at higher latitudes in the summer mesosphere, whereas the "tuned" flow (6.A) leads to an extending negative vorticity gradient up to low latitudes. Such a condition seems to be appropriate for unstable generated waves.

Therefore, the enhanced conditions are now disturbed by a wave like disturbance "in-situ" at mesospheric heights (experiment 6.B). If the mesosphere is in an unstable stage, only a spark of disturbance should be enough to excite the inherent solution of a wave. Along the the upper edge of the westward jet that is tilted from the lower equatorial mesosphere towards the polar mesopause, latitudinal as well as vertical wind gradients can be found which refer to barotropic and baroclinic unstable conditions, respectively. Therefore, small oscillations were introduced at three different places referring to baroclinic, barotropic/baroclinic and barotropic conditions (experiments 6.C_{1,2,3}). The local forcing was smoothed with a sine curve in latitude and height. Zonal wave numbers 3 and 4 and periods of 52.5 and 48 h, respectively, have been chosen. Amplitudes corresponded to a heating rate per unit mass of $\sim 2 K/d$. However, analyses both with initial disturbances as well as with permanent disturbances revealed no or only a weak response of a QTDW, respectively. Results of permanent forcing at the separate places are shown in Figs.(4.33) and (4.34). The weakest signal results from experiment 6.C₁, which corresponds to the highest latitude, but all excited oscillations do not propagate very well from its exciting point and the amplitudes do not grow, rather remain with their forced values. Increased forcing (experiment 6.D) leads to an increase in the response but remains limited in magnitude and propagation.

Searching for reasons of suppression of potential developing instabilities one possibility might be the numerical diffusion factor $\varepsilon = 0.1$ in COMMA-LIM, which was introduced into the leapfrog system following Asselin (1972) in order to ensure a convergent solution of the system. This Asselin-filtered leapfrog scheme has only a first-order accuracy. However, this filter parameter has the greatest impact on the most poorly resolved component of the solution, the $2\Delta t$ oscillation (Durran, 1999). Each filter application reduces the amplitude of the $2\Delta t$ -wave by a factor of $1 - 4\varepsilon$. Thus, the reduction of ε will act to increase the smallest oscillation. Nevertheless, experiments (6.E) with decreased $\varepsilon = 0.07, 0.05$ gave nearly no changes for the solutions, but smaller ε led to an interruption of calculation.

If COMMA-LIM summer stages are compared to other model results, they show similar values in the background flow as well as in gravity wave drag or in the development of a negative potential vorticity gradient. One can argue, that the necessary condition of $\partial\bar{q}/\partial\phi < 0$ might be not sufficient, but it was obviously sufficient for all other models. It turns out furthermore, since the different model design ranging from linear and purely dynamical models up to GCMs does not prevent a wave from developing, this instability is a dynamical process existing in the mesosphere and the troposphere may play an indirect role as upward propagation disturbances alter the mesospheric jets. A bad resolved troposphere is therefore not the relevant factor in this discussion.

However, a common feature of all successfully applied numerical models is their spectral or semi-spectral design. There, the horizontal structure of the numerical solution is represented as a truncated series of spherical harmonics (Durran, 1999). The spectral method is able to correctly capture the amplitude and phase speed of the shortest resolvable waves for the spatial derivative. This is a significant advantage over conventional grid-point methods, in which the spatial derivatives are approximated by finite differences. Additionally, it exists a down-scale energy cascade that develops if the governing equations of motion are accurately approximated. In spectral models this energy transfer from larger to smaller scales is accompanied by a second energy transfer from smaller to larger scales, which ensures the domain integrated kinetic energy. However, grid-point models generate only the down-scaling which is actually present in the atmosphere. The dissipation processes that eliminate the kinetic energy at those small scales have to be parameterised in order to stabilise the solution and prevent numerical nonlinear instability. This parameterisation should be designed to represent the true behaviour of the physical system as closely as possible, but it might be at the same time a blocking factor for experiments with instabilities.

These differences between spectral and grid-point models may have the most relevant importance in relation with generating unstable growing waves in the atmosphere, because such waves grow from small scale oscillations excited by the instabilities.

The question, if the grid-point structure in principle or the certain method of finite differences are responsible for damping such waves, has to be investigated in future.

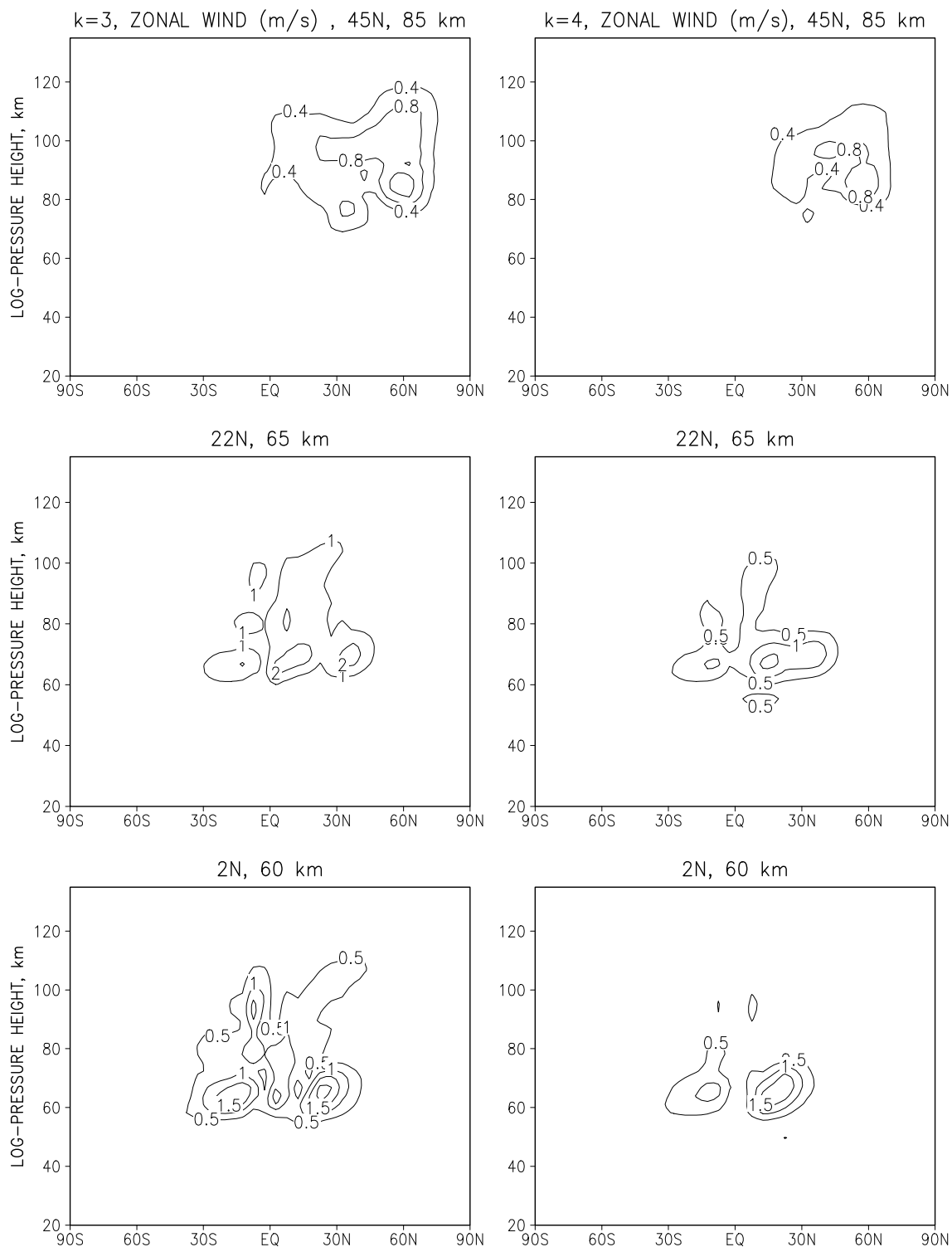


Figure 4.33: Zonal wind amplitudes of in situ 2-day waves forced at three different locations in the summer mesosphere corresponding to experiments 6.C₁, 6.C₂, and 6.C₃.

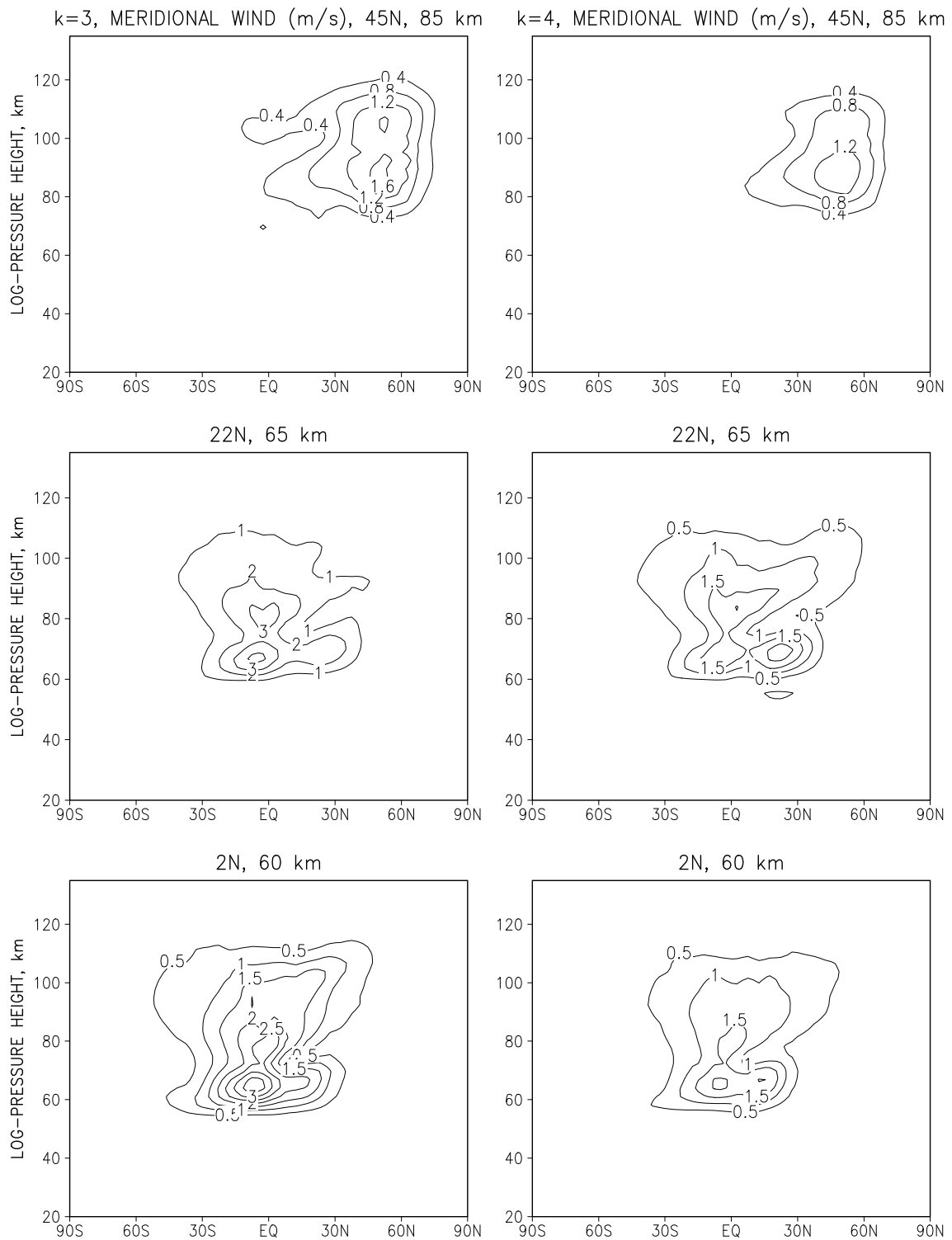


Figure 4.34: As in Fig.(4.33) but for meridional wind amplitudes.

Chapter 5

Conclusions

5.1 Summary

The COMMA-LIM model was used to study the propagation of the QTDW in the middle atmosphere, its impact on the mean flow and its interaction with manifold middle atmosphere waves. In this way, the knowledge about the wave could be summed up but revealed also the the gaps in understanding and modelling the middle atmosphere.

The numerical simulation of a QTDW forced as a steady Eigenmode shows a Rossby-gravity wave propagating upwards into the MLT region, predominantly in the summer hemisphere. The maximum of the meridional wind disturbance is twice as large as the maximum of the zonal wind component and has a symmetric behaviour with respect to the equator in contrast to the other wave fields u' , T' , Φ' . The resonant period in COMMA-LIM for July conditions was obtained for $52.5 h$. In the summer hemisphere the wave exerts a westward acceleration on the mean flow that intensifies the summer westward jet.

A transient QTDW exerts a stronger acceleration on the mean flow than the forcing with a steady wave. The most intense effect of a transient QTDW was found around the equator extending into both hemispheres. If a transient wave propagates upwards for the first time the change in zonal mean wind amounts to a maximum of $\sim 10 ms^{-1}$. However, if a transient wave has time to establish during 60 days its impact on the mean circulation is strongly reduced because the atmosphere is able to adjust to a regularly amplifying phenomenon. On the other hand, in a real atmosphere transient processes may not reach the level of a balanced interaction between wave and mean flow, thus the processes connected to the primary appearance of disturbances in the middle atmosphere might be more important.

Gravity waves play an important role in the propagation conditions for the QTDW. These waves provide the path for QTDW upward propagation. Additionally, due to their highly variable nature of generation GWs might be responsible for transient-like amplitudes of an Eigenmode-QTDW since their influence on the mean flow may supports or prevents

the wave from propagation into the MLT region over relatively short time scales. However, COMMA-LIM could show such a behaviour only in case studies.

The interaction of the QTDW with other PWs leads to significant amplitude modulations of the quasi two-day wave and a number of secondary PWs arise. During its interaction with the 16DW and 10DW the wave modulation is characterised by a remarkable loss of amplitude up to 20% but no amplitude growth was observed. The SPW1 seems to play the most important role in these non-linear interactions since the arising secondary PWs have the same period as the primary QTDW. The sum of all QTDWs is up to 60% stronger than the wave number-3 QTDW alone. Additionally, without a SPW1 in the model there exists only the primary QTDW but with the same magnitude of amplitude. This means that during the SPW1-QTDW interaction the stationary planetary wave provides the dominant part of energy on the secondary waves. Thus, radar data from a single station that cannot distinguish between the wave numbers may observe increased QTDW-amplitudes at a time, where the SPW1 shows a transient behaviour.

Considering the tides in relation with the QTDW it turned out that during QTDW events the tidal amplitudes reduce. This reduction seems to depend on the magnitude of the QTDW. Results of investigation on the secondary planetary waves and comparisons with Palo et al. (1999) indicate that the 16 h and 44 h-waves due to interaction with the diurnal tide draw their energy dominantly from the tide, while the QTDW is more responsible for feeding the $k = 5$, 9 h-wave in interaction with the semidiurnal tide.

The question, if the QTDW is able to contribute in a remarkable way to solar induced wind and temperature changes, has to be answered in the negative. By comparing the numerical results of wind amplitudes at mid-latitude MLT region with Jacobi (1998) the results are not in agreement, because the QTDW-activity is smaller during solar maximum conditions. However, at mesospheric heights around the equator the QTDW propagates better for solar maximum conditions. Several reasons may account for this discrepancy: first, the missing QBO in COMMA-LIM, which provides another background circulation. Another possibility is the ozone climatology, its variation in total and its latitudinal distribution throughout the solar cycle. Former studies gave remarkable different results if another data set for ozone or another variation between solar maximum and minimum were applied.

The numerical investigations on exciting an unstable growing QTDW from inertial or baroclinic instability failed. COMMA-LIM can be tuned to exhibit similar summer conditions that are known to be sufficient for generating a QTDW in other models, however no growing QTDW could be observed. It turned out furthermore, since the different model design ranging from linear and purely dynamical models up to GCMs does not prevent a wave from developing, this instability is a dynamical process existing in the mesosphere. The troposphere may play an indirect role as upward propagating disturbances alter the mesospheric jets but cannot penetrate the enhanced summer jet. Thus, the coarsely resolved troposphere is not the reason for the failure. Therefore, the most important difference between successful and unsuccessful model seems to be the spectral design of the models

that appears to be able to generate unstable waves.

In summary it could be shown, that not only instability processes can lead to an increase in QTDW activity during summer. In particular, varying gravity waves or transient stationary planetary waves were found to be important in these processes. It does not mean in turn, that a QTDW may not arise from instabilities, however the results underline that the atmosphere allows several solutions to the phenomenon called the QTDW.

5.2 Outlook

From this work arise several interesting points to be investigated in future.

The knowledge of gravity waves, their time and spatially varying nature and their impact on the mean circulation as well as on the large scale eddies has to be improved together with increasing numerical capabilities in simulating the atmospheric processes.

Considering the researches on the influence of the 11-year solar cycle on the middle atmosphere a study is recommended that investigates the sensitivity of small ozone changes on the mean flow, and therefore on the propagation conditions of the waves. This is particularly important for models that use prescribed ozone climatologies such as COMMA-LIM.

An important point to clarify in detail is, to what extent the differences between spectral models and grid point models and their difference schemes are responsible for the prevention of the development of unstable growing waves.

List of symbols

Symbol	Parameter	Value/Unit
a	earth radius	6366197 m
a_{GW}	acceleration due to breaking gravity waves	$m s^{-2}$
c	phase speed of a wave	$m s^{-1}$
\vec{c}_g	group velocity of waves	$m s^{-1}$
c_p	specific heat at constant pressure	$J kg^{-1} K^{-1}$
c_v	specific heat at constant volume	$J kg^{-1} K^{-1}$
e_{wh}	efficiency of mechanical energy conversion into heat	
f	Coriolis parameter $\equiv 2 \Omega \sin \phi$	s^{-1}
g	gravity	9.81 $m s^{-2}$
\mathbf{j}	electrical current density	$A m^{-2}$
k_λ	absorption coefficient	m^{-1}
k	zonal wavenumber	m^{-1}
l	meridional wavenumber	m^{-1}
m	vertical wavenumber	m^{-1}
m'	ratio of the molecular weights m/m_0	
m	molecular weight of air at level z	g
m_0	molecular weight of air at $z = 0$	28,96 $kg kmol^{-1}$
p	pressure	hPa
p_s	$= 1000 hPa$, if $z = z_0$, reference pressure	
q	potential vorticity	$m^{-1} s^{-1}$
t	time	s
u	zonal velocity	$m s^{-1}$
v	meridional velocity	$m s^{-1}$
w	$= \partial z / \partial t$, vertical velocity	$m s^{-1}$
z	$= H \ln(p/p_s)$, log. vertical coordinate	m
\mathbf{B}	magnetic field	nT
C	cooling rate	$K s^{-1}$
D	eddy diffusion coefficient	$m^2 s^{-1}$
\mathbf{E}	electrical field	$V m^{-1}$
E	GW energy	$kg m^{-2} s^{-1}$
F	Eliassen-Palm flux	$kg m^{-1} s^{-2}$

Symbol	Parameter	Value/Unit
F_λ	zonal acceleration due to unresolved and thermospheric processes	$m s^{-2}$
F_ϕ	meridional acceleration due to unresolved and thermospheric processes	$m s^{-2}$
F_T	heating rates due to unresolved and thermospheric processes	$K s^{-1}$
H	$= RT/g = 7000$, scale height	m
J	diabatic heating rate per unit mass	$J kg^{-1} s^{-1}$
K_m	thermal conduction coefficient	$W m^{-1} K^{-1}$
K_h	turbulent thermal conduction coefficient	$W m^{-1} K^{-1}$
K_H	coefficient of horizontal diffusion	$m^2 s^{-1}$
N	Brunt-Väisälä frequency	s^{-1}
R	gas constant for dry air	$287 J kg^{-1} K^{-1}$
Ri_f	dynamical Richardson number	0.4
Pr	turbulent Prandtl Number	3
T	temperature	K
Q	heating rate	$K s^{-1}$
\mathbf{V}	horizontal wind field vector	$m s^{-1}$
W	vertical streaming mass	$m s^{-1}$
Φ	geopotential	$m^2 s^{-2}$
Ω	rotation rate of earth $2\pi (sidereal\ day)^{-1}$	$7.292 \cdot 10^{-5} s^{-1}$
α	Newtonian cooling coefficient	s^{-1}
$\beta_{r\lambda,\phi}$	merged ion drag and Rayleigh friction in zonal/meridional direction	s^{-1}
ε_b	work against buoyancy force	$m^2 s^{-3} K^{-1}$
θ	potential temperature	K
λ	longitude	
κ	$\equiv R/c_p$	
μ	dynamic viscosity	$kg m^{-3} s^{-1}$
ν	kinematic eddy viscosity	$kg m^{-3} s^{-1}$
ρ_0	$= \rho_s exp[-z/H]$, basic density	$kg m^{-3}$
ρ_s	reference density at level z_0	
σ_0	parallel conductivity	$S m^{-1}$
σ_1	Pedersen conductivity	$S m^{-1}$
σ_2	Hall conductivity	$S m^{-1}$
ϕ	latitude	
φ	wave phase	
ω	angular frequency	s^{-1}
ω^+	intrinsic frequency	s^{-1}

Appendix A

Parameterisation of gravity waves

A.1 WKB solution

The linearised set of equations describing the propagation of GW for complex disturbance values $u', \phi', \theta' = (u'_{k,\omega}, \phi'_{k,\omega}, \theta'_{k,\omega})(z) \exp[i(kx - \omega t)]$ and $w' = w'(x, z, t) \exp[-i(kx - \omega t)]$ can be written as follows :

$$i\omega^+ u' - \frac{1}{k} \frac{\partial \omega^+}{\partial z} w' + ik\Phi' = \frac{1}{\rho} \frac{\partial}{\partial z} \rho D \frac{\partial u'}{\partial z}, \quad (\text{A.1})$$

$$\frac{\partial \Phi'}{\partial z} = \theta' \frac{R}{H} \exp\left(-\frac{\kappa z}{H}\right), \quad (\text{A.2})$$

$$iku' + \frac{1}{\rho} \frac{\partial}{\partial z} \rho w' = 0, \quad (\text{A.3})$$

$$-i\omega^+ \theta' + \frac{\partial \bar{\theta}}{\partial z} w' = \frac{1}{\rho} \frac{\partial}{\partial z} \rho \frac{D}{Pr} \frac{\partial \theta'}{\partial z} - \alpha \theta', \quad (\text{A.4})$$

where u' and w' are the perturbed horizontal (along the horizontal component of the wave vector) and vertical (positive) velocities, Φ' is the gravity wave geopotential, and θ' is the perturbed potential temperature; $\omega^+ = \omega - k(\bar{u} \cos \vartheta + \bar{v} \sin \vartheta)$ is an intrinsic frequency of a gravity wave, k is the horizontal wave number, \bar{u} and \bar{v} are zonal and meridional components of the background wind, ϑ is the azimuth of GW propagation; D and α are the eddy diffusion and Newtonian cooling coefficients, and Pr is turbulent Prandtl number. The further variables are explained in the list of symbols. Overbars denote the background values averaged over a wave period.

Without dissipation ($D = \alpha = 0$) equations (A.1)-(A.4) can be reduced to one equation of the perturbed vertical velocity $w' = w'(x, z, t) \exp[-i(kx - \omega t)]$

$$\left[\frac{d^2}{dz^2} + \mathcal{L} \frac{d}{dz} + \mathcal{M} \right] w'(z) = 0, \quad (\text{A.5})$$

where the operators \mathcal{L} , \mathcal{M} are

$$\mathcal{L} = -\frac{1}{H}, \quad \mathcal{M} = \frac{N^2 k^2}{\omega^{+2}} - \frac{1}{H} \frac{1}{\omega^+} \frac{\partial \omega^+}{\partial z} - \frac{1}{\omega^+} \frac{\partial^2 \omega^+}{\partial z^2},$$

and $N^2 = R(\partial \bar{T} / \partial z + \kappa \bar{T} / H) / H$ is the Brunt- Väisälä frequency squared.

In the case of slowly varying media equation A.5 has an approximate analytical solution, the so called WKB solution:

$$w'(z) = w'(z_0) [m(z_0) / m(z)]^{1/2} e^{\pm i \int_{z_0}^z m(z') dz'} e^{-\frac{1}{2} \int_{z_0}^z \mathcal{L}(z') dz'}, \quad (\text{A.6})$$

where the vertical wavenumber squared is:

$$m^2 = \mathcal{M} - \frac{1}{4} \mathcal{L}^2 - \frac{1}{2} \frac{\partial \mathcal{L}}{\partial z}.$$

One can show that for $\omega > 0$, the upper sign (plus) in solution (A.6) corresponds to the downward and the lower one (minus) to the upward propagating GWs.

A.2 First order correction due to dissipative terms

Assuming that dissipation is weak, we can obtain a first order correction to solution (A.6). To apply the perturbation theory, we introduce small parameters and reduce the initial set of equations to nondimensional form. Assuming that $m \gg 1/H$ (Lindzen, 1981), the initial set of equations (A.1-A.4) can be written as follows

$$(\varepsilon_u - i\tilde{\omega}^+) \tilde{u} - \frac{1}{\tilde{k}} \frac{\partial \tilde{\omega}^+}{\partial \zeta} \tilde{w} + i\tilde{k} \tilde{\Phi} = 0, \quad (\text{A.7})$$

$$\frac{d\tilde{\Phi}}{d\zeta} = \frac{R\bar{T}}{gH} \tilde{\theta}, \quad (\text{A.8})$$

$$i\tilde{k} \tilde{u} + \left(\frac{d}{d\zeta} - 1 \right) \tilde{w} = 0, \quad (\text{A.9})$$

$$(\varepsilon_t - i\tilde{\omega}^+) \tilde{\theta} + \frac{gH}{R\bar{T}} \tilde{N}^2 \tilde{w} = 0, \quad (\text{A.10})$$

where $\varepsilon_u = Dm^2/\omega$ and $\varepsilon_t = (Dm^2/Pr + \alpha)\omega$ are small parameters; $\zeta = z/H$ is the nondimensional height; $\tilde{\omega}^+ = \omega^+/\omega$, $\tilde{k} = kH$, $\tilde{N}^2 = N^2/\omega^2$, and we introduce the following nondimensional amplitudes of perturbations:

$$\begin{aligned} \tilde{u}(\zeta) &= \frac{\omega u'}{g} \exp[-i(kx - \omega t)], & \tilde{w}(\zeta) &= \frac{\omega w'}{g} \exp[-i(kx - \omega t)], \\ \tilde{\Phi}(\zeta) &= \frac{\Phi'}{gH} \exp[-i(kx - \omega t)], & \tilde{\theta}(\zeta) &= \frac{\theta'}{\theta} \exp[-i(kx - \omega t)]. \end{aligned}$$

Eliminating $\tilde{\theta}$ using (A.8) and (A.10), we obtain the perturbed energy equation in terms of the geopotential perturbation

$$(\varepsilon_t - i\tilde{\omega}^+) \frac{d\tilde{\Phi}}{d\zeta} + \tilde{N}^2 \tilde{w} = 0. \quad (\text{A.11})$$

Solving (A.7) with respect to $\tilde{\Phi}$ and using the linearised continuity equation (A.9) to eliminate \tilde{u} , we obtain

$$\tilde{\Phi} = i \frac{\tilde{\omega}^+}{\tilde{k}^2} \left[\left(1 + \frac{i\varepsilon_u}{\tilde{\omega}^+}\right) \left(\frac{d}{d\zeta} - 1\right) - \frac{1}{\tilde{\omega}^+} \frac{\partial \tilde{\omega}^+}{\partial \zeta} \right] \tilde{w}. \quad (\text{A.12})$$

Accounting that $\tilde{m} = mH \gg 1$ and the zero order solution (A.6), we can rewrite (A.12) as follows

$$\tilde{\Phi} = i \frac{\tilde{\omega}^+}{\tilde{k}^2} \left(\frac{d}{d\zeta} - 1 - \frac{1}{\tilde{\omega}^+} \frac{\partial \tilde{\omega}^+}{\partial \zeta} \right) \tilde{w} + \frac{i\varepsilon_u \tilde{m}}{\tilde{k}^2} \tilde{w}. \quad (\text{A.13})$$

The first order solution of (A.11) with respect to $d\tilde{\Phi}/d\zeta$ can be written as follows:

$$\frac{d\tilde{\Phi}}{d\zeta} = -i \frac{\tilde{N}^2}{\tilde{\omega}^+} \left(1 - \frac{i\varepsilon_t}{\tilde{\omega}^+}\right) \tilde{w}. \quad (\text{A.14})$$

Eliminating $\tilde{\Phi}$ in (A.14) using (A.13), we obtain

$$\left(\frac{d^2}{d\zeta^2} - \frac{d}{d\zeta} + \frac{\tilde{N}^2 \tilde{k}^2}{\tilde{\omega}^{+2}} - \frac{1}{\tilde{\omega}^+} \frac{\partial \tilde{\omega}^+}{\partial \zeta} - \frac{1}{\tilde{\omega}^+} \frac{\partial^2 \tilde{\omega}^+}{\partial \zeta^2} \right) \tilde{w} + \frac{\varepsilon_u \tilde{m}}{\tilde{\omega}^+} \frac{d\tilde{w}}{d\zeta} - \frac{i\varepsilon_t \tilde{N}^2 \tilde{k}^2}{\tilde{\omega}^{+3}} \tilde{w} = 0. \quad (\text{A.15})$$

To obtain the differential equation with real coefficients, we have to rearrange the last term in (A.15). Accounting that $\tilde{m} \approx \tilde{N}\tilde{k}/\tilde{\omega}^+ \gg 1$ and using the zero order solution (A.6), we can write the last term in (A.15) as follows:

$$-\frac{i\varepsilon_t \tilde{N}^2 \tilde{k}^2}{\tilde{\omega}^{+3}} \tilde{w} = \frac{\varepsilon_t \tilde{N}^2 \tilde{k}^2}{\tilde{\omega}^{+3} \tilde{m}} \frac{d\tilde{w}}{d\zeta} = \frac{\varepsilon_t \tilde{m}}{\tilde{\omega}^+} \frac{d\tilde{w}}{d\zeta}. \quad (\text{A.16})$$

Comparison between the equations of the first order (A.15) and zero order (A.5) with accounting of (A.16) shows that the dissipative terms only change the expression for \mathcal{L} , which in dimensional form can be written as follows:

$$\mathcal{L} = -\frac{1}{H} + \frac{(\varepsilon_u + \varepsilon_t)m}{\tilde{\omega}^+} = -\frac{1}{H} + \frac{D(1 + 1/Pr)m^3}{\omega^+} + \frac{\alpha m}{\omega^+}. \quad (\text{A.17})$$

Accounting $m \approx Nk/\omega^+$, we obtain that the dissipative terms in (A.17) tend to infinity when ω^+ tends to zero, i.e., near a critical level. The perturbation approach is applicable only if these dissipative terms are small in comparison with $1/H$. Usually, an upward propagating GW does not reach the critical level due to breaking or overturning in result of convective instability (see the next paragraph). Nevertheless, in numerical realisation we assume that the wave is near a critical level if $\alpha m/\omega^+ = O(1/H)$.

A.3 Breaking of GWs due to convective instability

Linearised theory is known to give a reasonable representation of even large-amplitude waves observed in the upper atmosphere. It is also used to estimate limits on the maximum amplitudes that such waves can attain (Hodges, 1967, 1969; Lindzen, 1981, 1968). Wave overturning (or breaking) due to convective instability occurs if the wave amplitude exceeds a certain limit. In terms of the perturbed potential temperature the breaking condition is $|\partial\theta'/\partial z| \geq \partial\bar{\theta}/\partial z$. This creates a convectively unstable situation and a transition from laminar to turbulent regime. To investigate the situation using the obtained analytical solution, we express this condition in terms of the perturbed vertical velocity. Equation (A.4) without dissipative terms and taking into account that in equation (A.6) the exponential term with integral of m is the strongest, gives the following approximate relation for breaking conditions

$$\left| \frac{\partial\theta'}{\partial z} \right| / \frac{\partial\bar{\theta}}{\partial z} = \frac{m|w'|}{\omega^+} \geq 1. \quad (\text{A.18})$$

Assuming that eddy diffusion limits the further increase in wave amplitude with height, we obtain the saturation condition in the following form

$$\frac{\partial}{\partial z} \left(\frac{m|w'|}{\omega^+} \right) = 0. \quad (\text{A.19})$$

Using solution (A.6), $m = kN/\omega^+$, and the first order solution for \mathcal{L} (A.17), we obtain

$$\frac{1}{2H} - \frac{D(1 + 1/Pr)m^3}{2\omega^+} - \frac{\alpha m}{2\omega^+} - \frac{3}{2} \frac{1}{\omega^+} \frac{\partial\omega^+}{\partial z} = 0. \quad (\text{A.20})$$

Solving (A.20) with respect to the eddy diffusion coefficient D and using $m = kN/\omega^+$, we obtain (Schoeberl et al., 1983)

$$D = \frac{\omega^{+4}}{k^3 N^3 (1 + 1/Pr)} \left(\frac{1}{H} - \frac{\alpha m}{\omega^+} - 3 \frac{1}{\omega^+} \frac{\partial\omega^+}{\partial z} \right). \quad (\text{A.21})$$

For the Newtonian cooling coefficient we use the parameterisation of radiative damping rate given by Zhu (1993).

A.4 Mean flow acceleration due to dissipation and breaking of GWs

Under breaking conditions GWs accelerate the mean flow due to vertical divergence of the vertical momentum flux. Usually, following the suggestions by Lindzen (1981), this forcing per unit mass is calculated using the obtained expressions for D (A.21) and \mathcal{L} (A.17) and

under the assumption that GWs are under breaking condition everywhere above the first breaking level (Jakobs et al., 1986).

However, the background wind can substantially influence the propagation conditions of GWs (Pogoreltsev and Pertsev, 1996) and we have to expect the wave overturning only in some layers where the breaking condition is satisfied (Akmaev, 2001). Especially this is important when the "mean" flow includes large-scale atmospheric waves with a short vertical wavelength (for instance, at low latitudes in the MLT region, where the diurnal tide and sometimes Kelvin waves have substantial amplitudes). To take into account such possibility, we consider the divergence of the vertical momentum flux. The forcing per unit mass due to this divergence can be written using equation (A.3) and solution (A.6) as follows

$$a_{GW} = -\frac{1}{\rho} \frac{\partial}{\partial z} (\overline{\rho u' w'}) = -\frac{1}{\rho} \frac{\partial}{\partial z} \left(\rho \frac{m \overline{w'^2}}{k} \right) = \frac{|w'|^2 m}{2k} (\mathcal{L} + \frac{1}{H}), \quad (\text{A.22})$$

accounting being taken that $\overline{w'^2} = 0.5|w'|^2$. Eq.(A.22) shows that without dissipation ($\mathcal{L} = -1/H$) the GWs do not accelerate the mean flow. Using the first order solution for \mathcal{L} (A.17), we obtain

$$a_{GW} = \frac{|w'|^2 m^2}{2k\omega^+} [D(1 + 1/Pr)m^2 + \alpha]. \quad (\text{A.23})$$

Substituting $|w'|_b = \omega^+/m$ (amplitude of the vertical velocity perturbation at breaking level) and eddy diffusion coefficient D (A.21) in (A.23), we obtain the explicit expression for the forcing per unit mass, which usually has been used to calculate the GW drag in general circulation models (Hunt, 1986; Jakobs et al., 1986; Holton and Zhu, 1984; Schoeberl et al., 1983) with the Lindzen (1981) parameterisation

$$a_{GW} = \frac{\omega^+}{2k} \left[\frac{\omega^{+2}}{kN} \left(\frac{1}{H} - \frac{\alpha m}{\omega^+} - 3 \frac{1}{\omega^+} \frac{\partial \omega^+}{\partial z} \right) + \alpha \right] \approx \frac{\omega^{+3}}{2k^2 N} \left(\frac{1}{H} - 3 \frac{1}{\omega^+} \frac{\partial \omega^+}{\partial z} \right). \quad (\text{A.24})$$

However, as is noted above, this parameterisation assumes that GWs are under breaking condition everywhere above the first breaking level. To apply the Lindzen-type parameterisation of the GW drag to background conditions with a strong variability of zonal and meridional winds with altitude, we follow the suggestions by Akmaev (2001). Stepping up from a given height level z , it is sufficient to calculate $|w'(z + \Delta z)|$ using the WKB solution (A.6) with \mathcal{L} taking into account some background dissipation (radiative damping in our case). The second integral in the right-hand part of (A.6) can be estimated using the simplest quadrature formula (Gavrilov, 1990). $|w'(z + \Delta z)|$ is next compared with the breaking value $|w'|_b = \omega^+/m$. If $|w'(z + \Delta z)|$ exceeds $|w'|_b$, then it is reset to $|w'|_b$, the GW assumed to break between z and $z + \Delta z$, and the forcing per unit mass (A.22) is calculated by finite differences

$$a_{GW}(z + \Delta z/2) = \frac{1}{2k} \left[\frac{m(z + \Delta z)|w'(z + \Delta z)|^2 + m(z)|w'(z)|^2}{2H} - \frac{m(z + \Delta z)|w'(z + \Delta z)|^2 - m(z)|w'(z)|^2}{\Delta z} \right]. \quad (\text{A.25})$$

Otherwise, the wave is assumed to propagate free of breaking and the acceleration of the mean flow is conditioned only by radiative damping of GWs. It should be noted that in practice the GW levels are situated between the levels of the COMMA-LIM model, and accelerations in zonal and meridional directions are calculated as follows

$$a_{GW\lambda} = a_{GW} \cos \vartheta, \quad a_{GW\vartheta} = a_{GW} \sin \vartheta,$$

where ϑ is the azimuth of GW propagation.

Using $|w'(z_k)|$, we can estimate more correctly the eddy diffusion coefficient. One can obtain from solution (A.6) the following relation:

$$\frac{\partial}{\partial z} \ln(m^{1/2}|w'|) = -\mathcal{L}/2. \quad (\text{A.26})$$

Substituting \mathcal{L} (A.17) into (A.26) and solving the obtained equation with respect to D , we obtain

$$D = \frac{\omega^+}{m^3(1+1/Pr)} \left[\frac{1}{H} - \frac{\alpha m}{\omega^+} - 2 \frac{\partial}{\partial z} \ln(m^{1/2}|w'|) \right], \quad (\text{A.27})$$

which will be used to estimate the cooling/heating contribution of the GWs. To calculate $D(z_k + \Delta z/2)$, i.e., at the COMMA-LIM levels, the ω^+ and m averaged over GW levels z_k are used, and the last term in (A.27) is calculated by finite differences.

A.5 Heating/cooling of the atmosphere by GWs

Accounting that in log-pressure coordinates $\bar{T} = \bar{\theta} \exp(-\kappa z/H)$, the thermodynamic equation can be written in terms of the background temperature (Schoeberl et al., 1983)

$$\frac{\partial \bar{T}}{\partial t} + \bar{\mathbf{V}} \cdot \nabla \bar{T} + \bar{w} \frac{\kappa \bar{T}}{H} = -\frac{\bar{T}}{\bar{\theta}} \frac{1}{\rho} \frac{\partial}{\partial z} (\overline{\rho w' \theta'}) + \frac{\bar{T}}{\bar{\theta}} \frac{1}{\rho c_p} \frac{\partial}{\partial z} (\rho c_p \frac{D}{Pr} \frac{\partial \bar{\theta}}{\partial z}) + \bar{Q} - \bar{C}, \quad (\text{A.28})$$

where \bar{Q} and \bar{C} are the mean heating and cooling per unit mass, respectively. Subsequently the overbars denoting the background state will be omitted. The first term in the right-hand side of equation (A.28) describes the heating/cooling effects due to GW dissipation. Accounting that $\theta'/\theta = T'/T$, we obtain in terms of the heat flux:

$$-\frac{T}{\theta} \frac{\partial}{\partial z} (\overline{\rho w' \theta'}) = -\frac{1}{\rho} \frac{\partial}{\partial z} (\overline{\rho w' T'}) - \frac{\kappa}{H} \overline{w' T'}. \quad (\text{A.29})$$

Using the zero order solution for GWs and equation (A.4) we can obtain the following expression:

$$\frac{\overline{w' \theta'}}{\theta} = \frac{\overline{w' T'}}{T} = -(\alpha + Dm^2/Pr) \left(\frac{1}{\theta} \frac{\partial \theta}{\partial z} \right)^{-1} \frac{\overline{\theta'^2}}{\theta^2} = -\frac{(\alpha + Dm^2/Pr)}{2} \left(\frac{1}{\theta} \frac{\partial \theta}{\partial z} \right)^{-1} \frac{|\theta'^2|}{\theta^2}. \quad (\text{A.30})$$

Taking into account the polarisation relation between θ' and w' [zero order solution of equation (A.4)], we obtain

$$\left(\frac{1}{\theta} \frac{\partial \theta}{\partial z}\right)^{-1} \frac{|\theta'^2|}{\theta^2} = \frac{1}{\omega^{+2}} \frac{1}{\theta} \frac{\partial \theta}{\partial z} |w'|^2, \quad (\text{A.31})$$

and the heat flux in terms of the vertical velocity perturbation can be written as follows

$$\overline{w'T'} = -\frac{HN^2(\alpha + Dm^2/Pr)}{2R\omega^{+2}} |w'|^2 \approx -\frac{Hm^2(\alpha + Dm^2/Pr)}{2Rk^2} |w'|^2, \quad (\text{A.32})$$

accounting being taken that

$$\frac{1}{\theta} \frac{\partial \theta}{\partial z} = \frac{H}{RT} N^2.$$

The dissipative GW deposits energy in the atmosphere, and in the presence of wind shear the energy conservation equation for GWs can be written (Plumb, 1983b):

$$\frac{\partial E}{\partial t} + \nabla \cdot \mathbf{F} = \frac{\rho}{k} \frac{\partial \omega^+}{\partial z} \overline{u'w'} - S_{GW}, \quad (\text{A.33})$$

where

$$\begin{aligned} E &= \frac{\rho}{2} [\overline{u'^2} + N^2 \left(\frac{\partial \theta}{\partial z}\right)^{-2} \overline{\theta'^2}], \\ \mathbf{F} &= \rho \overline{\mathbf{V}'\Phi'} - \mathbf{i}_z \rho D \left[u' \frac{\partial u'}{\partial z} + \frac{N^2}{Pr} \left(\frac{\partial \theta}{\partial z}\right)^{-2} \theta' \frac{\partial \theta'}{\partial z} \right], \end{aligned}$$

and \mathbf{i}_z is the unit vector along the vertical coordinate. The first term in the right-hand side of (A.33) is the conversion of GW kinetic energy to the kinetic energy of the mean state. The nonconservative sink term S_{GW} describes the loss of the GW energy due to dissipation and can be written as follows

$$S_{GW} = N^2 \left(\frac{\partial \theta}{\partial z}\right)^{-2} \left[\rho \frac{D}{Pr} \overline{\left(\frac{\partial \theta'}{\partial z}\right)^2} + \alpha \rho \overline{\theta'^2} \right] + \rho D \overline{\left(\frac{\partial u'}{\partial z}\right)^2}. \quad (\text{A.34})$$

Using polarisation relations of GWs [equations (A.3-A.4) without dissipative terms] and taking into account that

$$m \gg 1/H, \quad \overline{\left(\frac{\partial \theta'}{\partial z}\right)^2} = 0.5 \text{Re} \left[\frac{\partial \theta'}{\partial z} \left(\frac{\partial \theta'}{\partial z}\right)^* \right] \approx 0.5 m^2 |\theta'|^2,$$

where * denotes a complex conjugate value, we obtain

$$S_{GW} = \frac{\rho}{2} \left[\frac{N^2}{\omega^{+2}} \left(\alpha + \frac{Dm^2}{Pr} \right) + \frac{Dm^4}{k^2} \right] |w'|^2 \approx \frac{\rho N^2 [\alpha + Dm^2(1/Pr + 1)]}{2\omega^{+2}} |w'|^2, \quad (\text{A.35})$$

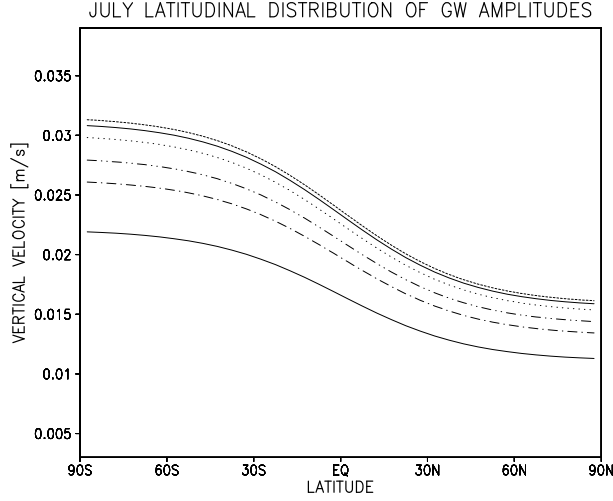


Figure A.1: Latitudinal distribution of July-mean gravity waves for 6 waves with different phase speed. Amplitudes are given in terms of vertical velocity.

or in terms of the heat flux (see Eq.(A.32))

$$S_{GW}/\rho c_p = -(1 + \frac{D}{\alpha + Dm^2/Pr}) \frac{\kappa}{H} \overline{w'T'}. \quad (\text{A.36})$$

Comparison of (A.36) and (A.29) shows that the last term in the right-hand side of (A.29) can be interpreted as the local heating rate due to conversion of the potential energy provided by GW dissipation into heat [see also (A.34) and (A.35)]. This term appears in (A.28) explicitly. The second term in the right-hand side of (A.36) describes the mechanical energy provided by GW dissipation. Some part of this energy is lost through production of turbulence and/or other waves that remove energy from the region considered. The remaining mechanical energy will be converted into heat (Schoeberl et al., 1983; Medvedev and Klaassen, 2003), and we have to introduce the corresponding heating term into the right-hand side of (A.28). Finally, the total heating rate due to GW dissipation can be written as follows:

$$Q_{GW} = -\frac{1}{\rho} \frac{\partial}{\partial z} (\rho \overline{w'T'}) - (1 + e_{wh} \frac{D}{\alpha + Dm^2/Pr}) \frac{\kappa}{H} \overline{w'T'}, \quad (\text{A.37})$$

where $e_{wh} \leq 1$ is an efficiency of the mechanical energy conversion into heat. In COMMA-LIM it is set $e_{wh} = 1$. It should be noted that without dissipation $\overline{w'\theta'} = \overline{w'T'} = 0$ [see (A.32)] and GWs do not interact with the mean state.

In each GW time step, 48 waves are initialised, horizontally propagating in eight equally spaced directions, and six different phase speeds ranging from 5 to 30 $m s^{-1}$. All waves have the same horizontal wavelength $\lambda_x = 300, km$ and the wave amplitudes w_0 (given

here in terms of the vertical velocity) are weighted by frequency and phase speed in order to provide a realistic spectrum at launch height $z_0 = 10 \text{ km}$.

$$w'(\omega, c, z = z_0) = w_0 c \frac{1}{1 + (\omega/\omega_0)^\alpha} \frac{1}{1 + (c/c_1)^\beta + (c/c_2)^\gamma}, \quad (\text{A.38})$$

with the spectrum parameters $\omega_0, \alpha, \beta, \gamma, c_1, c_2$ as given in Gavrilov and Fukao (1999). In addition a latitudinal and seasonal weighted term with increasing GW activity in the winter hemisphere is applied. The so obtained wave-amplitude distribution is shown in Fig.(A.1). In Fig.(A.2) the accelerations on the zonal and meridional wind due to divergence of the vertical momentum flux of gravity waves is displayed together with the heating rate caused by the gravity waves.

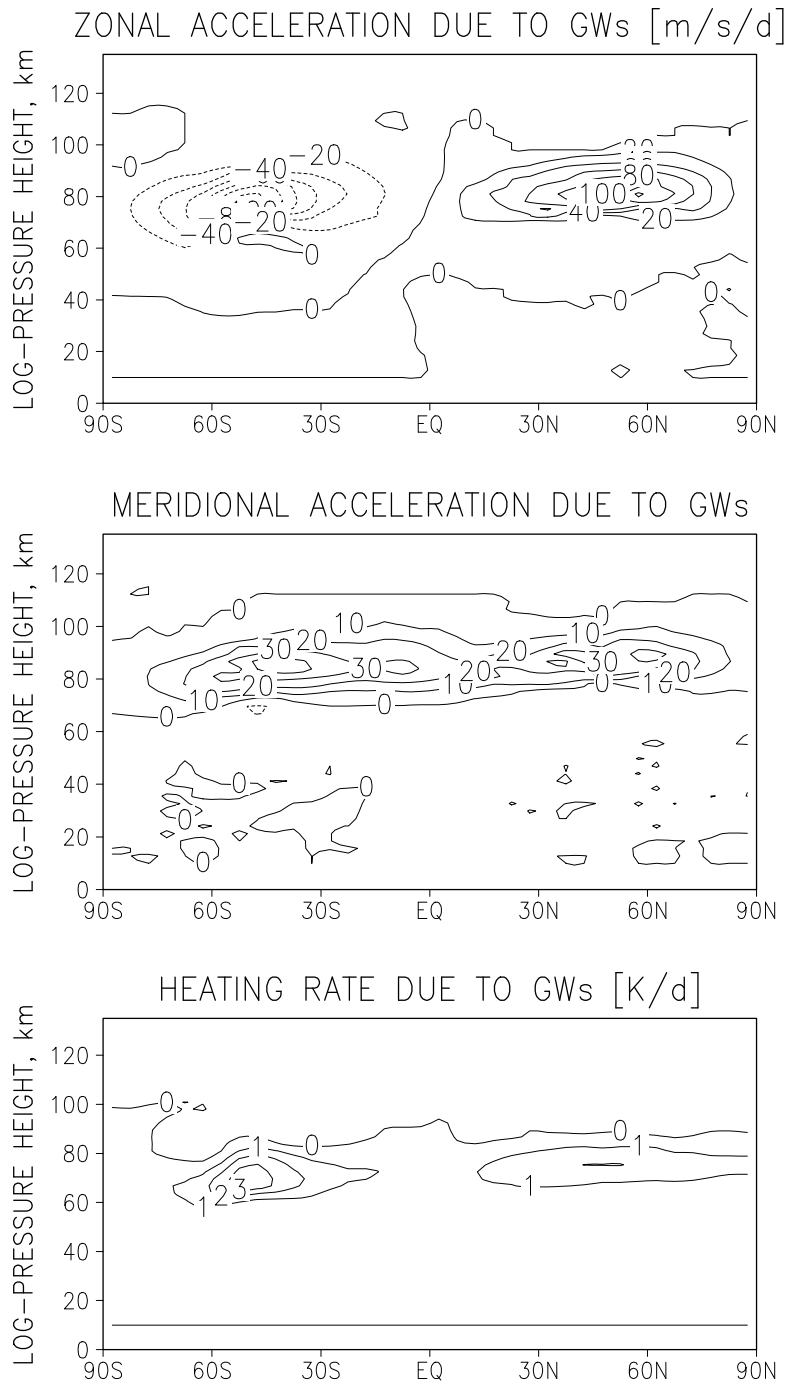


Figure A.2: Top panel: The acceleration on the zonal wind caused by GWs. Middle: the same for the meridional wind. Bottom: heating rate of the atmosphere caused by GWs. July conditions at COMMA-LIM day 90 are applied.

Appendix B

Radiation

B.1 Heating due to absorption of solar radiation

We first consider a nonscattering atmosphere. The direct downward solar flux at level τ is given by the exponential attenuation of the effective solar flux at the top of the atmosphere (TOA) $\mu_0 F_{\lambda\infty}$. Thus

$$F_{dir}^-(\tau) = \mu_0 F_{\lambda\infty} \exp^{-\tau/\mu_0}, \quad (\text{B.1})$$

where $\mu_0 = \cos \vartheta_0$, ϑ_0 denotes the solar zenith angle, and for monochromatic direct solar flux, the total direct downward solar flux can be written as

$$F_s(z) = \int_0^\infty \mu_0 F_{\lambda\infty} \exp\left(-\frac{k_\lambda u(z)}{\mu_0}\right) d\lambda, \quad (\text{B.2})$$

where $k_\lambda u(z)$ represents the optical depth, k_λ is the absorption coefficient. The absorbing gaseous path length is defined by

$$u(z) = \int_z^{z_\infty} \rho_a(z') dz', \quad (\text{B.3})$$

where ρ_a denotes the density of the absorbing gas and z_∞ denotes the height at TOA. The total solar flux at TOA can be written as follows

$$S = \int_0^\infty F_{\lambda\infty} d\lambda, \quad (\text{B.4})$$

and monochromatic absorptance may be expressed by

$$A_\lambda(u/\mu_0) = 1 - \exp(-k_\lambda u/\mu_0). \quad (\text{B.5})$$

We may define broadband solar absorptance as follows (Liou, 1992):

$$A(z) = \frac{1}{S} \int_0^\infty F_{\lambda\infty} A_\lambda(u/\mu_0) d\lambda, \quad (\text{B.6})$$

and equation (B.2) can be rewritten in the form

$$F_s(z) = \mu_0 S [1 - A(z)]. \quad (\text{B.7})$$

Broadband solar absorptance may be rewritten in terms of spectral absorptance A_i in the form

$$A(z) = \int_0^\infty A_\lambda(u/\mu_0) w_\lambda d\lambda \approx \sum_i A_i(u/\mu_0) w_i \Delta\lambda_i, \quad (\text{B.8})$$

where $w_\lambda = F_{\lambda\infty}/S$. For large values of total absorption, the empirical expression for the mean spectral absorptivity can be written as follows (Liou and Sasamory, 1975):

$$\bar{A}_i = A_i \Delta\lambda_i = \frac{1}{\Delta\nu_i} [C_i + D_i \log_{10}(u p^{\eta_i}/\mu_0 + \chi_{0i})], \quad (\text{B.9})$$

or in terms of the reduced pressure \tilde{p} (Liou, 1992)

$$\bar{A}_i = \frac{1}{\Delta\nu_i} [C_i + D_i \log_{10}(\tilde{p}/\mu_0 + \chi_{0i})], \quad (\text{B.10})$$

where

$$\tilde{p}_i = \int_0^u p^{\eta_i} du = \int_z^{z_\infty} \rho_a p^{\eta_i} dz'. \quad (\text{B.11})$$

The heating rate can be written (Liou, 1992):

$$\left(\frac{\partial T}{\partial t}\right)_s = -\frac{\mu_0 S}{\rho c_p} \sum_i w_i \frac{d\bar{A}_i(u/\mu_0)}{dz} = \frac{\mu_0 S \rho_a}{\rho c_p} \sum_i w_i \frac{d\bar{A}_i(u/\mu_0)}{du}, \quad (\text{B.12})$$

where

$$\frac{d\bar{A}_i(u/\mu_0)}{du} = \frac{\log_{10} e}{\mu_0} \sum_i \frac{D_i}{\Delta\nu_i} (\tilde{p}_i/\mu_0 + \chi_{0i})^{-1} \frac{d\tilde{p}_i}{du}, \quad (\text{B.13})$$

and

$$\frac{d\tilde{p}_i}{du} = p^{\eta_i}. \quad (\text{B.14})$$

Finally, taking into account Rayleigh scattering and surface reflection (Liou, 1992), we obtain

$$\left(\frac{\partial T}{\partial t}\right)_s = \frac{S \rho_a \log_{10} e}{\rho c_p} \sum_i \frac{w_i D_i}{\Delta\nu_i} \left\{ \frac{p^{\eta_i}}{\tilde{p}_i/\mu_0 + \chi_{0i}} + \frac{\mu_0 r(\mu_0)}{\bar{\mu}} [1 - A(z_b)] \frac{p^{\eta_i}}{\tilde{p}_{b_i}/\bar{\mu} + \chi_{0i}} \right\}, \quad (\text{B.15})$$

where $r(\mu_0)$ is the combined reflection due to the Rayleigh layer and the surface, $1/\bar{\mu}$ is the diffusivity factor, $z_b = 0$ for water vapor absorption, and

$$\tilde{p}_{b_i} = \int_{z_b}^z \rho_a p^{\eta_i} dz'. \quad (\text{B.16})$$

Fig.(B.1) shows the heating rates of the considered gas components in different bands as described in chapter 3.

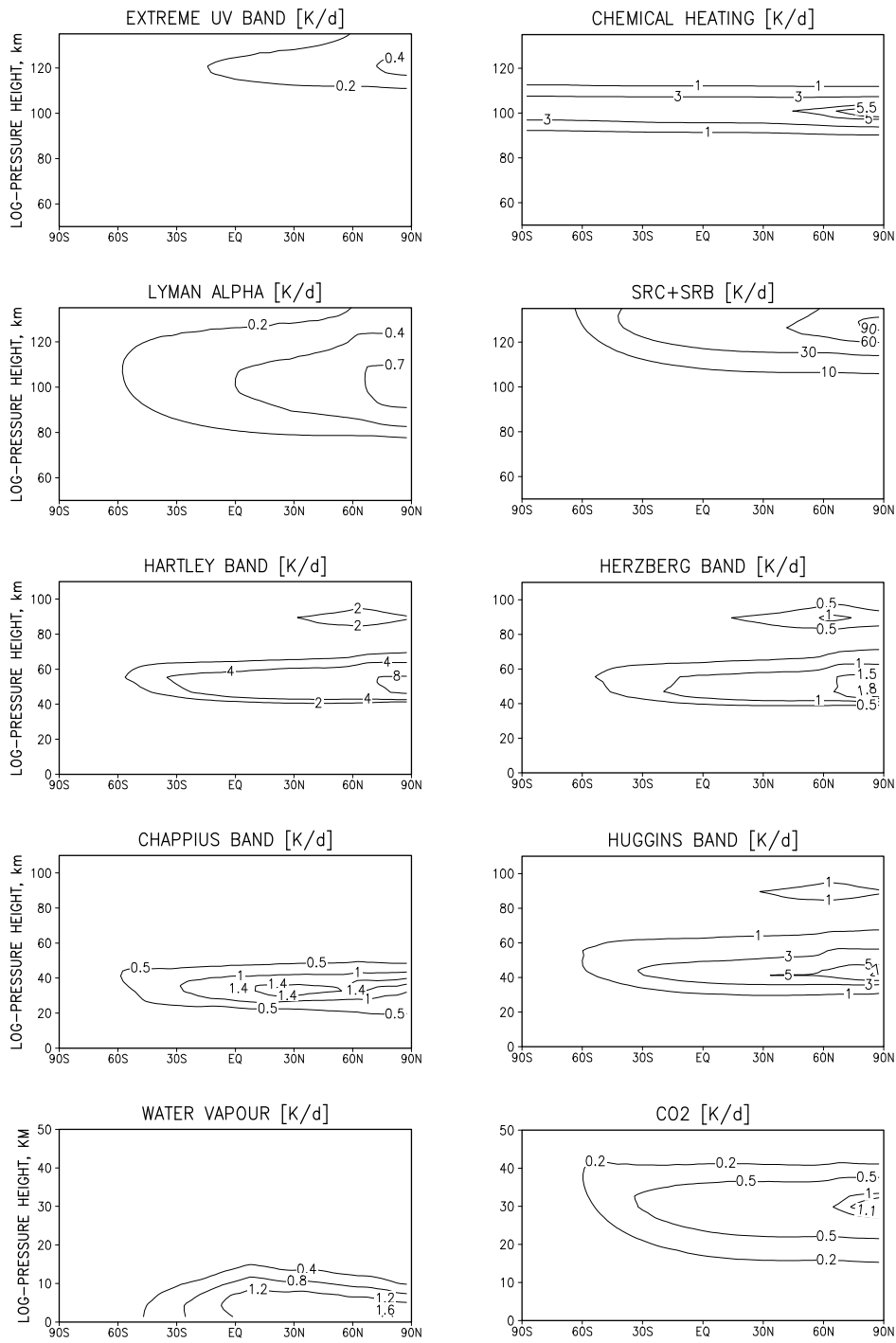


Figure B.1: Heating rates of the several gas components in different bands as calculated with COMMA-LIM under July conditions. Please note, that the height ranges are adjusted to the local maxima of absorption of each considered term.

B.2 Infrared radiation

Here, only a brief overview will be given on the fundamentals and parameterisation and for a details the reader is referred to Andrews et al. (1987).

The radiative transfer equation describes the rate of decrease or increase of monochromatic radiance L of a given frequency ν , L_ν along a length element ds in the direction $\hat{\Omega}$ which is proportional to the amount of absorbing matter

$$dL_\nu(\hat{\Omega}) = -k_\nu \rho_a [L_\nu(\hat{\Omega}) - J_\nu(\hat{\Omega})] ds \quad (\text{B.17})$$

Here, k_ν is the extinction coefficient describing the rate of extinction of L_ν along ds , ρ_a the density of absorbing gas component and J_ν the source function, describing the rate of increase. Extinction is expressed as the sum of absorption and scattering processes, but infrared waves are too long to be scattered. Under conditions of local thermodynamic equilibrium (LTE) with no scattering the source function J_ν is equal to the Planck function $B_\nu = 2 h \nu^3 / c^2 (e^{h\nu/k_b T} - 1)^{-1}$. The *flux density* F is derived as the integration of the radiance L of given frequency from the surface into the half-space in the direction of the unit normal vector $\hat{\mathbf{n}}$

$$F = \int_{2\pi} (\hat{\mathbf{n}} \cdot \hat{\Omega}) L_\nu(\hat{\Omega}) d\Omega. \quad (\text{B.18})$$

The net flux F_n is the difference between the upward and downward directed flux densities F_\uparrow and F_\downarrow in a plane-parallel atmosphere. Calculation of the exchange of thermal infrared radiation requires integration over the IR-spectrum, which are thousands of absorption lines. However, the source (Planck) function is generally a slowly varying function of frequency, so it is convenient to work with spectrally integrated functions over a band r . The band transmission function, representing the extinction of radiation, is then defined as

$$\bar{T}_r = \Delta\nu_r^{-1} \int_{\Delta\nu_r} \exp\left[-\int_{z_1}^{z_2} k_\nu(z) \rho_a(z) dz\right] d\nu, \quad (\text{B.19})$$

where $\Delta\nu_r$ is the spectral band width. \bar{T}_r has to be weighted over the considered half space with zenith angle $\mu \equiv \cos\theta$ and is then called the *flux transmission function*

$$\tau(z_1, z_2) = 2 \int_0^1 \mu \bar{T}_r(z_1, z_2, \mu) d\mu. \quad (\text{B.20})$$

The upward directed density flux F_\uparrow of a given level z is composed by the blackbody radiation from the earths surface weakened on the path through the atmosphere and the upward directed IR radiation in adjacent layers which are also subject of extinction between z' and z .

$$F_\uparrow(z) = \pi B_r(z=0) \tau(0, z) + \pi \int_0^z B_r(z') \frac{\partial \tau(z, z')}{\partial z'} dz'. \quad (\text{B.21})$$

Then, the downward directed density flux F_\downarrow represents the IR radiation at a given layer z weakened through the above lying levels

$$F_\downarrow(z) = -\pi \int_z^\infty B_r(z') \frac{\partial \tau(z, z')}{\partial z'} dz'. \quad (\text{B.22})$$

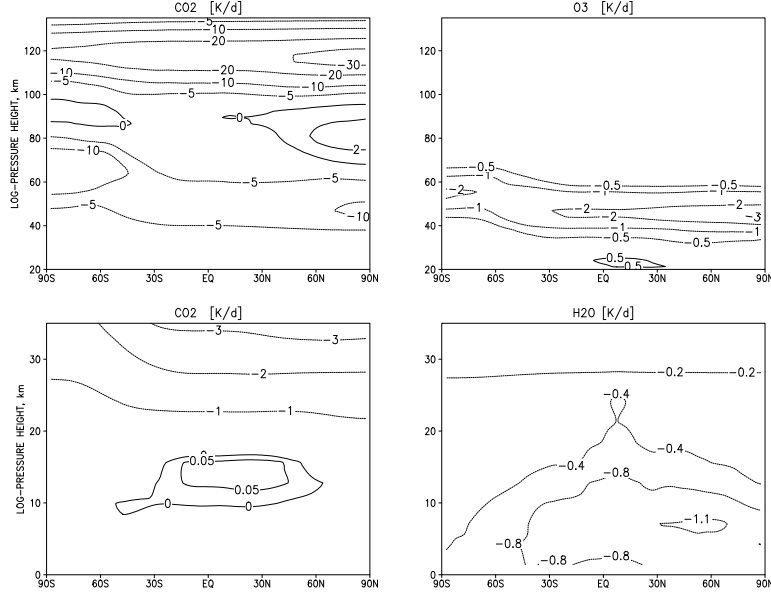


Figure B.2: Cooling rates of the three gas components as calculated with COMMA-LIM under July conditions. Please note, that the height ranges are adjusted to the local maxima of absorption of each considered term.

Note that $\partial\tau(z, z')/\partial z' < 0$ and therefore $F_{\downarrow}(z) > 0$. The heating rate per unit mass of air due to band r , $h_r(z)$ is given by

$$c_p \frac{dT_r}{dt} = -\rho_0^{-1} \frac{dF_{n,r}}{dz}, \quad (\text{B.23})$$

so it follows from Eqs.(B.21), (B.22) and (B.23)

$$\begin{aligned} c_p \frac{dT_r}{dt} = & \pi/\rho_0(z) \left\{ -B_r(z) \frac{d\tau(z, \infty)}{dz} - [B_r(0) - B_r(z)] \frac{d\tau(z, 0)}{dz} \right. \\ & - \int_0^z [B_r(z') - B_r(z)] \frac{\partial^2 \tau(z, z')}{\partial z \partial z'} dz' \\ & \left. - \int_z^\infty [B_r(z') - B_r(z)] \frac{\partial^2 \tau(z, z')}{\partial z \partial z'} dz' \right\} \quad (\text{B.24}) \end{aligned}$$

The terms in this exchange integral formulation of the heating rate represent the contributions to infrared heating at z due to the possible exchange of photons between levels. The first term describes the exchange with space. This term contributes always to *cooling*, since downward IR-flux from space can be neglected. The second term refers to the exchange with the underlying surface. Depending on the sign of $\partial\tau(z, 0)/\partial z$ - if it is negative -, it contributes to heating if $B_r(0) > B_r(z)$. Similarly, the last two terms stands for the exchanges with underlying and overlying layers and contribute to heating wherever $B_r(z') > B_r(z)$. $\partial^2 \tau(z, z')/\partial z \partial z'$ is always negative or zero.

Appendix C

July climatology

Since the work concentrates on the Northern Hemisphere summer this sections shows and discusses the climatology of July.

Figures (C.1, C.2, C.3) show the different contributing parts of the horizontal momentum equations and the thermodynamic equation on day 90 for July 1. No traveling planetary waves are excited at this stage; only the SPW1 is included.

C.1 Temperature field

Observed features of the atmospheric temperature field are (Scaife et al., 2000): a cold equatorial tropopause below 210 K , a cold winter stratosphere together with a raised altitude of the winter stratopause, a warm stratosphere/stratopause at the summer hemisphere due to absorption by ozone and above a very cold summer mesopause region with temperatures down to 130 K . While the temperature maximum at the summer stratopause and the minimum in the polar winter stratosphere derived from radiation processes the other extremes develop through the meridional circulation and eddy motions in the middle atmosphere. In general, COMMA-LIM matches these features well. However, in comparison with the CIRA-86 temperature (note the different latitude-height extension) the model overestimates the temperature maximum at the stratopause. The most important difference occurs at the polar summer mesopause, where COMMA-LIM temperatures are below 160 K . This temperature value is not in agreement with the $< 140 K$. Recent observations reported even on $\sim 120 K$ polar mesopause temperatures in July. This means, that there is still a lack of knowledge to what amount gravity waves, tides and planetary waves act to cool the mesopause region. Another important point is the distribution of mesospheric ozone which contributes to heating there. These factors have to be investigated in future. In the thermosphere the temperature increases rapidly with height due to heating of molecular and atomic oxygen as described in the foregoing subsections.

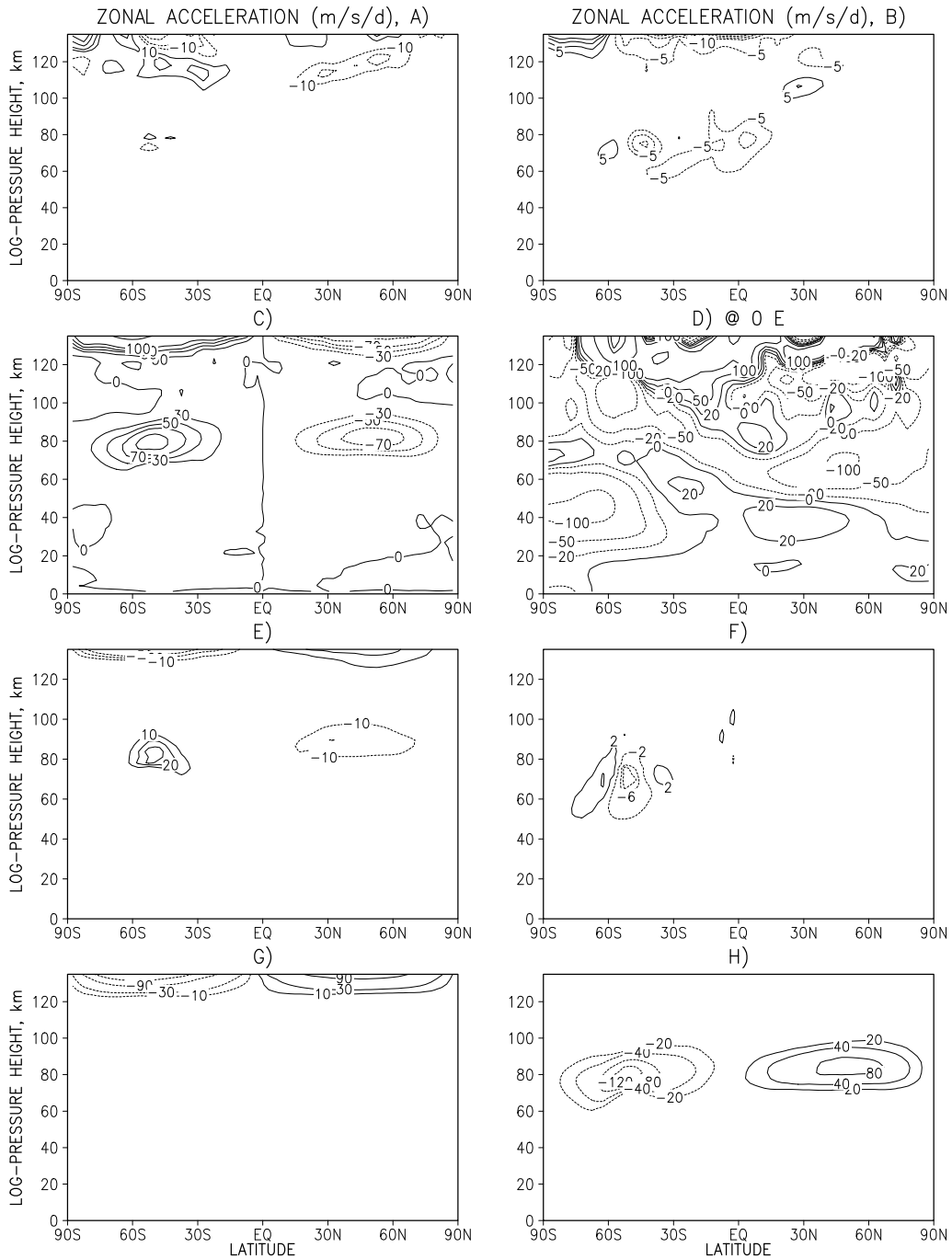


Figure C.1: The individual terms contributing to the zonal momentum budget as calculated with COMMA-LIM after 90 days of July 1. Units of the zonal means are $m s^{-1} d^{-1}$. A) zonal acceleration due to local change, B) advection, C) Coriolis acceleration including correction due to Hall conductivity, D) zonal pressure gradient at $0^\circ E$, E) molecular and eddy viscosity, F) turbulent diffusion, G) Rayleigh friction, including ion drag due to Pedersen conductivity, H) gravity wave drag.

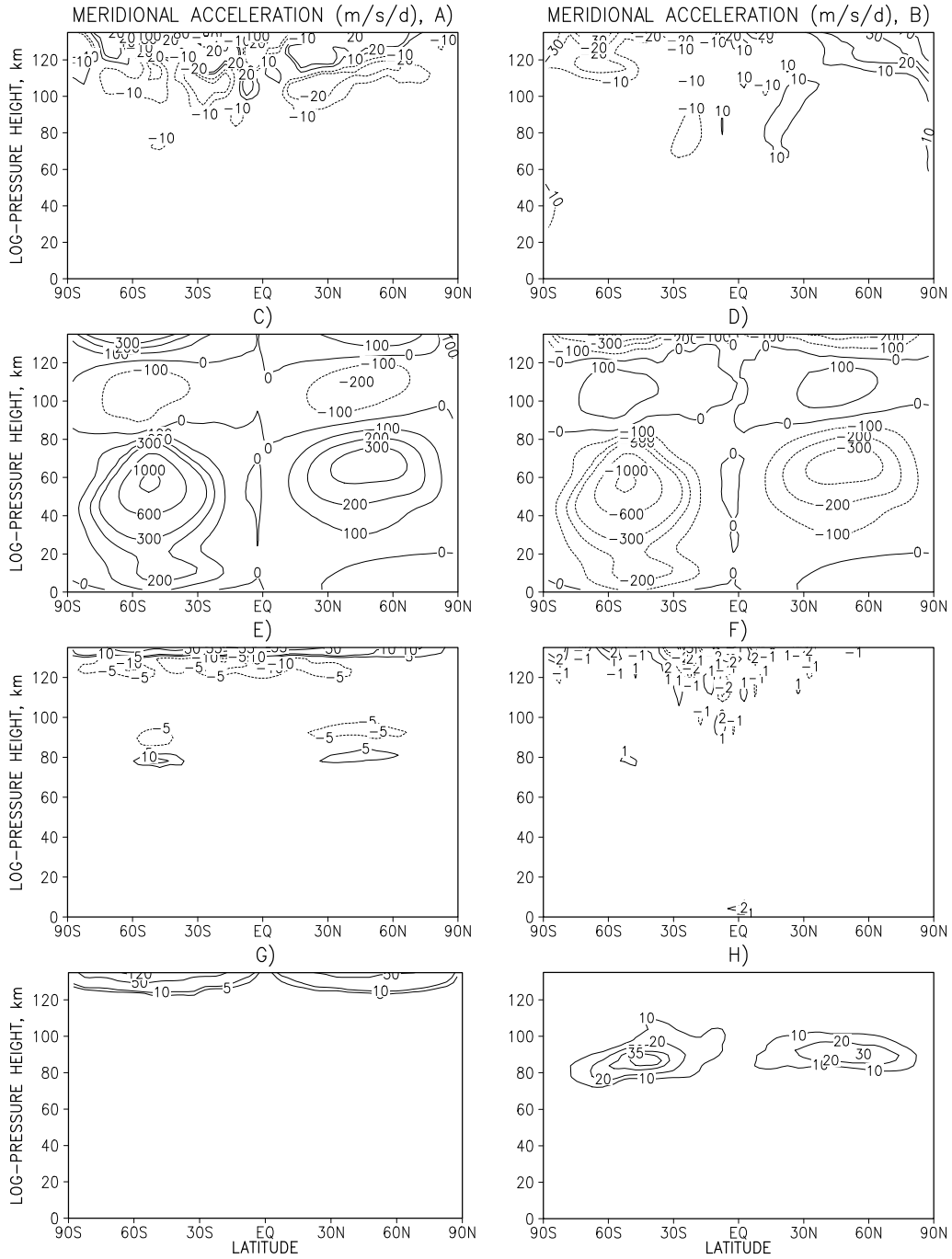


Figure C.2: The individual terms contributing to the meridional momentum budget as calculated with COMMA-LIM after 90 days of July 1. Units of the zonal means are $m s^{-1} d^{-1}$. A) meridional acceleration due to local change, B) advection, C) Coriolis acceleration including correction due to Hall conductivity, D) meridional pressure gradient, E) molecular and eddy viscosity, F) turbulent diffusion, G) Rayleigh friction, including ion drag due to Pedersen conductivity, H) gravity wave drag.

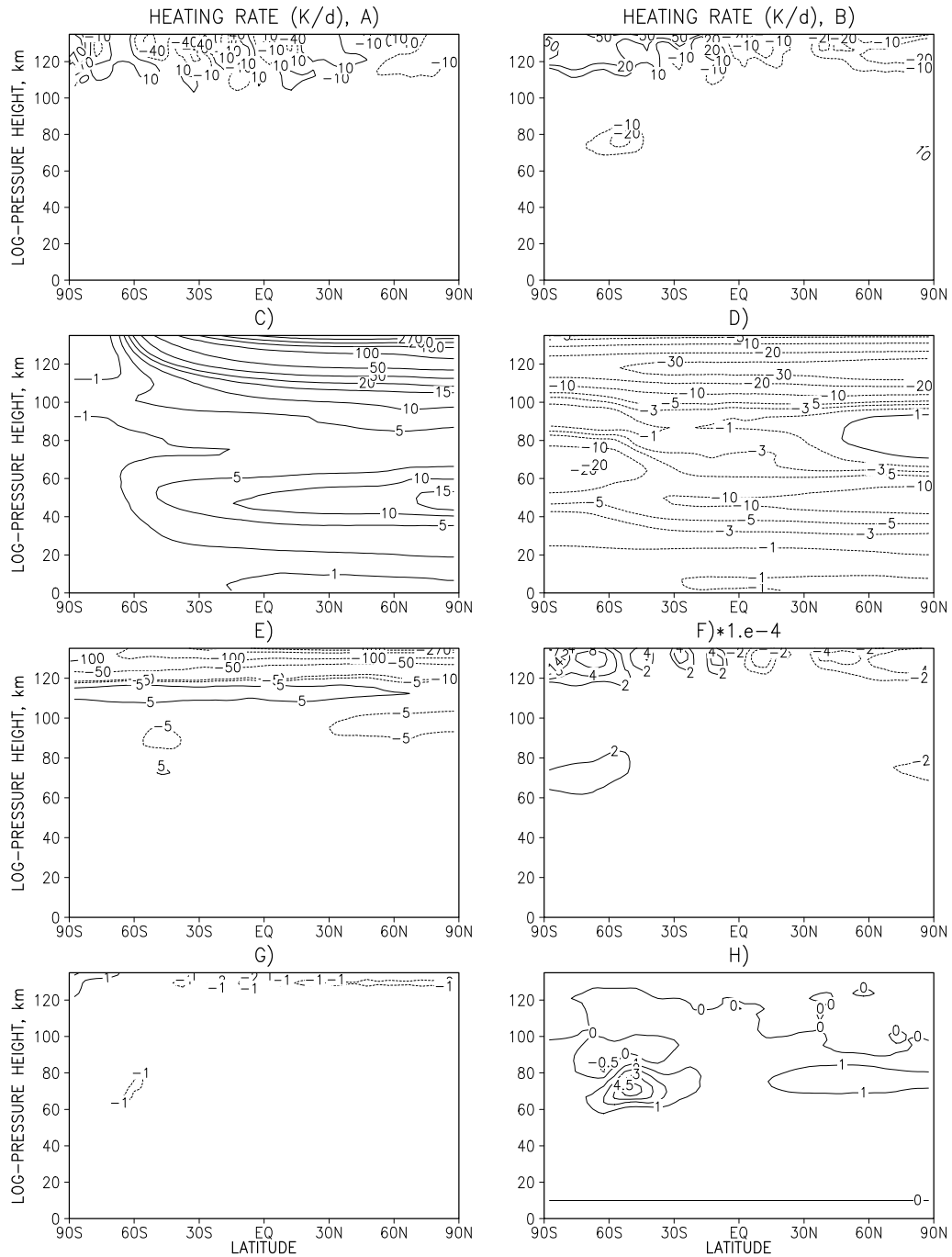


Figure C.3: The individual terms contributing to the energy budget as calculated with COMMA-LIM after 90 days of July 1. Units of the zonal means are $K d^{-1}$. A) heating rate due to local change, B) advection, C) heating due to absorption of solar radiation, D) cooling due to infrared radiation, E) molecular conduction, F) adiabatic transport, G) turbulent diffusion, H) heating due to breaking gravity waves.

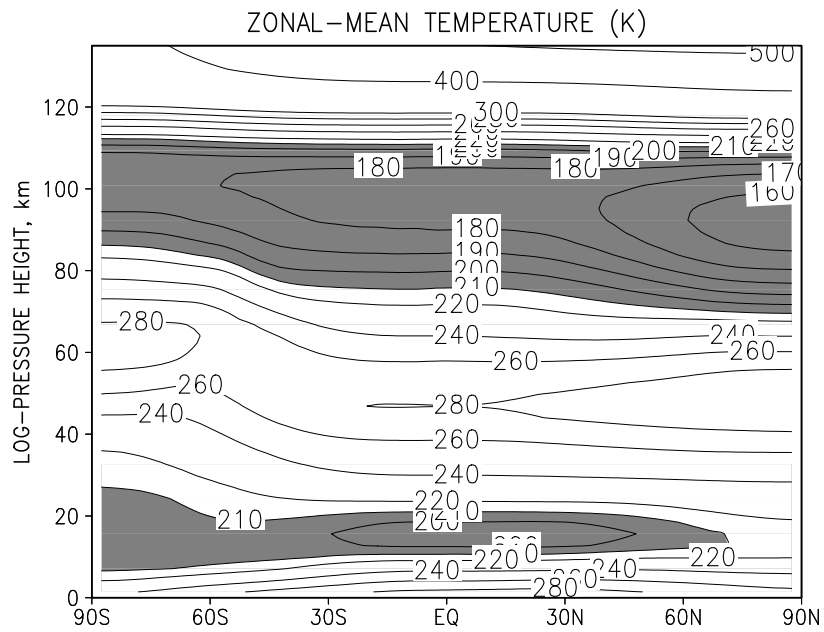
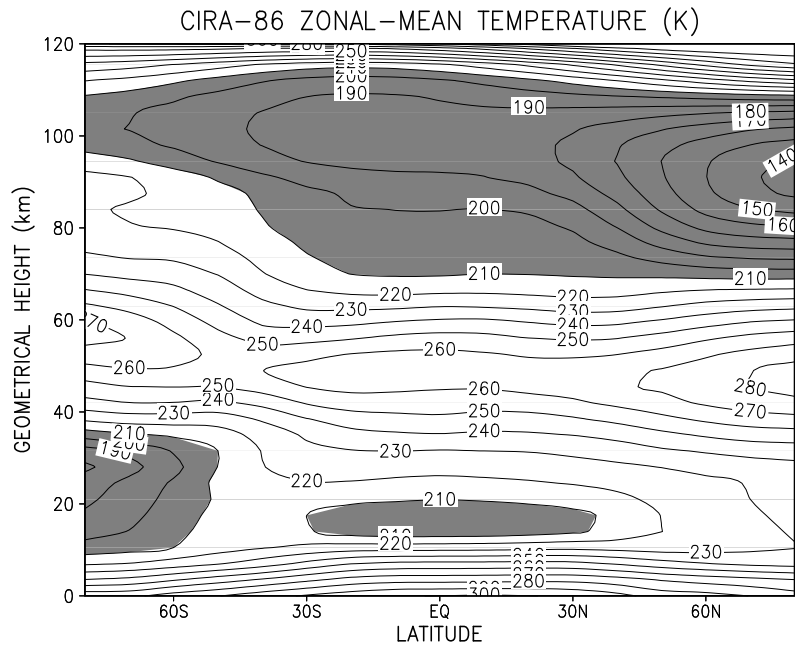


Figure C.4: Top panel: CIRA-86 zonal mean temperature for July. Note the geometrical height and upper boundary at ~ 120 km. The latitude ranges from -80° to 80° . Values are taken from Fleming et al. (1988). Bottom panel: zonal-mean temperature latitude-height cross-sections for July as calculated with COMMA-LIM. Values below 210 K are shaded.

C.2 Wind field

The climatological values for the zonal and meridional winds can be easily recognised. For the troposphere one has to take into account that we only have four layers to describe it and no hydrological cycle. The troposphere therefore acts as a lower boundary and we have only very coarse dynamical conditions. We compare our zonal winds with wind measurements from the High Resolution Doppler Imager (HRDI) which were combined with results from the UK Met. Office stratospheric data assimilation system within URAP (UARS Reference Atmosphere Project), see also Swinbank and Ortland (2003). They published monthly mean values from April 1992 to March 1993. Note that this publication presents only monthly values from one year and cannot take into account year to year variability.

Beginning with the troposphere, one can see the easterly jet appearing only in the summer tropical region. The westerly jet in the winter hemisphere at around 30° S and the respective jet in the summer hemisphere at about 40° N agree very well in location but not so well in absolute values compared with URAP values. But one can see the asymmetric seasonal behaviour that is conditioned by the topography of the earth (here, approximated via the included SPW1) and the distribution of water vapor.

In the stratosphere and mesosphere the westward jet extends over the summer hemisphere and is tilted northward with height like observations suggest. However, the summer jet in COMMA-LIM is about 20 m s^{-1} weaker and has only one maximum instead of two as observed. Several reasons are assumed to be responsible for this difference: first, no planetary waves besides the SPW1 are included. A second reason can be the medium scale variability in ozone (and heating rate) which is not presented in the climatological fields. The winter jet maximum of COMMA-LIM is in agreement with the URAP climatology in height and magnitude, however it is placed more equatorwards than the measured winds. Furthermore, the eastward wind in COMMA-LIM is replaced by the wind reversal at heights of 80 km , whereas URAP eastward winds extend up to 95 km . The mesopause region is characterized by the zonal wind reversal due to the momentum deposition of breaking gravity waves. The measurements show a good agreement of jet reversal in the winter hemisphere but not such strong reversal in the northern hemisphere.

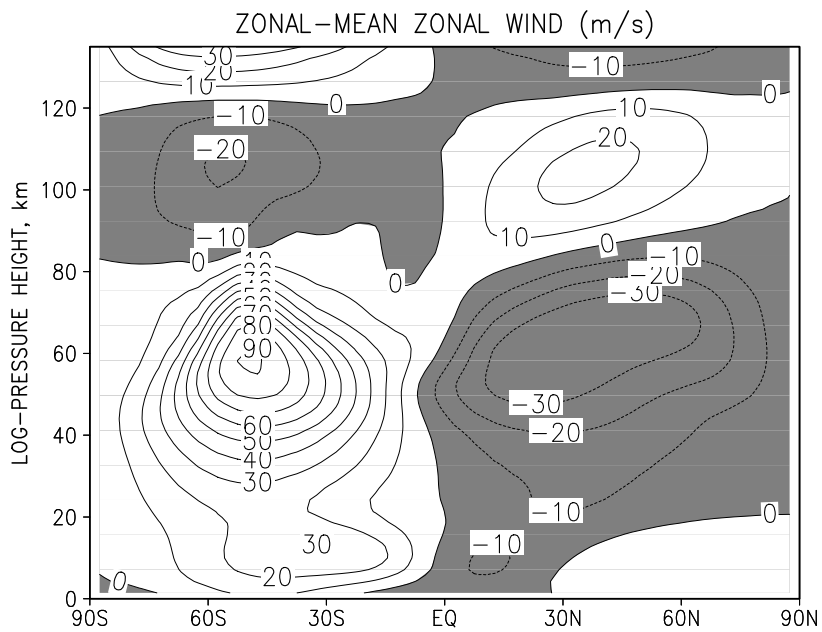
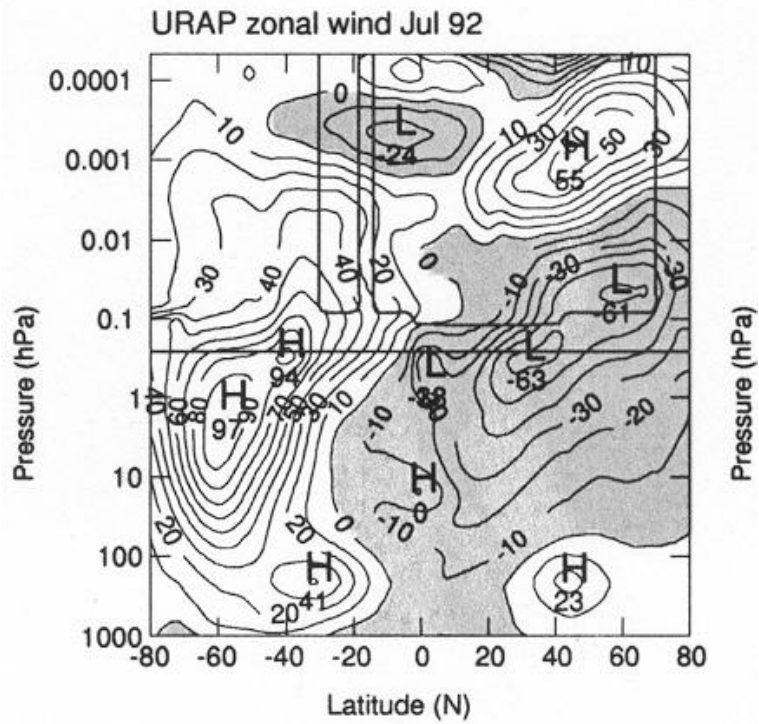


Figure C.5: Top panel: Zonal-mean zonal wind cross-section for July in the URAP baseline year. The additional lines show where the values are mainly derived from interpolated or climatological data. Taken from Swinbank and Ortland (2003). Bottom: Zonal-mean zonal winds cross-sections for July as calculated with COMMA-LIM. Negative values are shaded.

Bibliography

- Akmaev, R. A. (2001). Simulation of large scale dynamics in the mesosphere and lower thermosphere with Doppler-spread parameterization of gravity waves. 2. Eddy mixing and the diurnal Tide . *J. Geophys. Res.*, 102:1205–1203.
- Andrews, D., Holton, J., and Leovy, C. (1987). *Middle Atmosphere Dynamics*. Academic Press.
- Andrews, D. and McIntyre, M. (1978). Generalized Eliassen-Palm and Charney-Drazin theorems for waves on axisymmetric mean flows in compressible atmospheres. *J. Atmos. Sci.*, 35:175–185.
- Arnold, N. and Robinson, T. (1998). Solar cycle changes to planetary wave propagation and their influence on the middle atmosphere circulation . *Ann. Geophysicae*, 16:69–76.
- Arnold, N. and Robinson, T. (2000). Amplification of the influence of solar flux on the winter stratosphere by planetary waves. *Space Sci. Rev.*, 94:279–286.
- Asselin, R. (1972). Frequency filter for time integrations. *Mon. Wea. Rev.*, 100:487–490.
- Baier, F. (2000). *Entwicklung und Anwendung eines adjungierten Modells zur Simulation des Ozonhaushaltes der Stratosphäre während realer Episoden*. Mitteilungen aus dem Institut für Geophysik und Meteorologie der Universität zu Köln, University of Cologne.
- Berger, U. (1994). *Numerische Simulation klimatologischer Prozesse und thermischer Gezeiten in der mittleren Atmosphäre*. Mitteilungen aus dem Institut für Geophysik und Meteorologie der Universität zu Köln, University of Cologne.
- Bristow, W., Yee, J.-H., Zhu, X., and Greenwald, R. (1999). Simultaneous observations of the July 1996 2-day wave event using the Super Dual Auroral Radar Network and the High Resolution Doppler Imager. *J. Geophys. Res.*, 104(A6):12715–12721.
- Chou, M.-D., Ridgway, W., and Yan, M.-H. (1993). One-Parameter Scaling and Exponential-Sum Fitting for Water Vapor and CO_2 Infrared Transmission Functions. *J. Atmos. Sci.*, 50(14):2294–2303.

- Clark, R., Current, A., Manson, A., Meek, C., Avery, S., Palo, S., and Aso, T. (1994). Hemispheric properties of the two-day wave from mesosphere-lower thermosphere radar observations. *J. Atmos. Terr. Phys.*, 56(10):1294–1288.
- Coy, L. and Fritts, D. (1988). Gravity wave heat fluxes: A Lagrangian approach. *J. Atmos. Sci.*, 45:1770–1780.
- Craig, R. and Elford, W. (1981). Observations of the quasi 2-day wave near 90 km altitude at Adelaide (35°S). *J. Atmos. Terr. Phys.*, 43(10):1051–1056.
- Durrán, D. (1999). *Numerical Methods for Wave Equations in Geophysical Fluid Dynamics*. Springer-Verlag.
- Eliassen, A. (1949). The quasi-static equations of motion with pressure as independent variable. *Geofys. Publ.*, 17(3):44.
- Eliassen, A. and Palm, E. (1961). On the transfer of energy in stationary mountain waves. *Geofys. Publ.*, 22(3):1–23.
- Fedulina, I., Pogoreltsev, A., and Vaughan, G. (2004). Seasonal, interannual and short-term variability of planetary waves in met. office stratospheric assimilated fields. *Quart. J. R. Met. Soc.*, 130(60):2445–2460.
- Fleming, E., Chandra, S., Schoeberl, M., and Barnett, J. (1988). *Monthly mean global climatology of temperature, wind, geopotential height, and pressure for 0-120 km*. National Aeronautics and Space Administration. Technical memorandum 100697. Washington. D.C.
- Fligge, M., Solanki, S., Pap, J., Fröhlich, C., and Wernli, C. (2001). Variations of solar spectral irradiance from near UV to the infrared - measurements and results. *J. Atmos. Solar-Terr. Phys.*, 63:1479–1487.
- Fomichev, V., Blanchet, J.-P., and Turner, D. (1998). Matrix parameterization of the 15μ CO_2 band cooling in the middle and upper atmosphere for variable CO_2 concentration. *J. Geophys. Res.*, 103(D10):11505–11528.
- Fomichev, V. and Shved, G. (1985). Parameterization of the radiative flux divergence in the 9.6μ O_3 band. *J. Atmos. Terr. Phys.*, 47:671–688.
- Fomichev, V., Ward, W. E., Beagley, S. R., McLandress, C., Connell, J., Farlane, N., and Shepherd, T. (2002). Extended Canadian Middle Atmosphere Model: Zonal-mean climatology and physical parameterizations. *J. Geophys. Res.*, 107(10):ACL9 1–16.
- Forbes, J. and Garrett, H. (1979). Theoretical studies of atmospheric tides. *Rev. Geophys. Space Phys.*, 17(8):1951–1981.

- Fortuin, J. and Langematz, U. (1995). An update on the global ozone climatology and on concurrent ozone and temperature trends. *SPIE, Atmospheric Sensing and Modeling*, 2311:207–216.
- Fritts, D. and Isler, J. (1994). Mean Motions and Tidal and Two-Day Structure and Variability in the Mesosphere and Lower Thermosphere over Hawaii. *J. Atmos. Sci.*, pages 2145–2164.
- Fritts, D., Isler, J., Lieberman, R., Burrage, M., Marsh, D., Nakamura, T., Toshitaka, T., Vincent, R., and Reid, I. (1999). Two-day wave structure and mean flow interactions observed by radar and High Resolution Doppler Imager. *J. Geophys. Res.*, 104(D4):3953–3969.
- Fröhlich, K. and Jacobi, C. (2004). The solar cycle in the middle atmosphere: changes of the mean circulation and of propagation conditions for planetary waves. *Rep. Inst. Meteorol. Univ. Leipzig*, 34:106–117.
- Garcia, R. (1987). On the mean meridional circulation of the middle atmosphere. *J. Atmos. Sci.*, 44:3599–3609.
- Gavrilov, N. (1990). Parameterization of accelerations and heat flux divergences produced by internal gravity waves in the middle atmosphere. *J. Atmos. Terr. Phys.*, 52:707–713.
- Gavrilov, N. and Fukao, S. (1999). A comparison of seasonal variations of gravity wave intensity observed with the middle and upper atmosphere radar with a theoretical model. *J. Atmos. Sci.*, 56:3485–3494.
- Gavrilov, N. and Yudin, V. (1992). Model for the coefficients of turbulence and effective prandtl number produced by breaking gravity waves in the upper atmosphere. *J. Geophys. Res.*, 97:7619–7624.
- Glass, M., Fellous, J., Masseur, M., Spizzichino, A., Lysenko, I., and Portnyagin, Y. I. (1975). Comparison and interpretation of the results of simultaneous wind measurements in the lower thermosphere at Garchy (France) and Obninsk (U.S.S.R.) by meteor radar technique. *J. Atmos. Terr. Phys.*, 37:1077–1087.
- Grollmann, T. (1992). *Wechselwirkung freier Moden, Gezeiten und Schwerewellen in der mittleren Atmosphäre*. Mitteilungen aus dem Institut für Geophysik und Meteorologie der Universität zu Köln, University of Cologne.
- Günther, G. (1995). *Die numerische Simulation von Transportprozessen in der mittleren Atmosphäre*. Mitteilungen aus dem Institut für Geophysik und Meteorologie der Universität zu Köln, University of Cologne.
- Gurubaran, S., Sridharan, S., Ramkumar, T., and Rajaram, R. (2001). The mesospheric quasi-2-day wave over Tirunelveli 8.7°N. *J. Atmos. Solar-Terr. Phys.*, 63:975–985.

- Hagan, M. (2004). <http://www.hao.ucar.edu/public/research/tiso/gswm/gswm.html>.
- Haigh, J. (1994). Modelling the impact of solar variability on climate. *J. Atmos. Solar-Terr. Phys.*, 61:63–72.
- HAMMONIA (2004). <http://www.mpimet.mpg.de/en/depts/bgcs/drg/>.
- Harnik, N. (2002). The evolution of a stratospheric wave packet. *J. Atmos. Sci.*, 59:202–217.
- Harnik, N. and Lindzen, R. (2001). The effect of reflecting surfaces on the vertical structure and variability of stratospheric planetary waves. *J. Atmos. Sci.*, 58:2872–2894.
- Harris, T. and Vincent, R. (1993). The quasi 2-day wave in the equatorial middle atmosphere. *J. Geophys. Res.*, 98:10713–10723.
- Herman, R., Robinson, W., and Franke, S. (1999). Observational evidence of quasi two-day/gravity wave interaction using MF radar. *Geophys. Res. Lett.*, 26(8):1141–1144.
- Hines, C. (1997a). Doppler-spread parameterization of gravity wave momentum deposition in the middle atmosphere, 1, Basic formulation. *J. Atmos. Solar-Terr. Phys.*, 59:371–386.
- Hines, C. (1997b). Doppler-spread parameterization of gravity wave momentum deposition in the middle atmosphere, 2, Broad and quasi-monochromatic spectra, and implementation. *J. Atmos. Solar-Terr. Phys.*, 59:387–400.
- Hodges, R. R. J. (1967). Generation of turbulence in the upper atmosphere by internal gravity waves. *J. Geophys. Res.*, 72:3455–3458.
- Hodges, R. R. J. (1969). Eddy diffusion coefficients due to instabilities in internal gravity waves. *J. Geophys. Res.*, 74:4087–4090.
- Holton, J. (1992). *An introduction to dynamic Meteorology*. Academic Press.
- Holton, J. and Zhu, X. (1984). A further study of gravity wave induced drag and diffusion in the mesosphere. *J. Atmos. Sci.*, 41:2653–2662.
- Hunt, B. (1981). The 2-day wave in the middle atmosphere as simulated in a general circulation model extending from surface to 100 km. *J. Atmos. Terr. Phys.*, 43(11):1143–1154.
- Hunt, B. (1986). The impact of gravity wave induced drag and diurnal variability on the general circulation of the middle atmosphere. *J. Meteorol. Sci. Jap.*, 64:1–16.
- Izakov, M. N. (1978). On the influence of turbulence on a thermal regime of the planetary thermospheres. *Cosmic Research*, 16:4033–411.

- Jacobi, C. (1998). On the solar cycle dependence of winds and planetary waves as seen from mid-latitude D1 LF mesopause region wind measurements. *Ann. Geophysicae*, 16:1534–1543.
- Jacobi, C., Schminder, R., and Kürschner, D. (1998). Nonlinear-interaction of the quasi 2-day wave and long-term oscillations in the summer midlatitude mesopause region as seen from LF D1 wind measurements over Central Europe (Collm, 52°N,15°E). *J. Atmos. Solar-Terr. Phys.*, 60:1175–1191.
- Jacobi, C., Schminder, R., and Kürschner, D. (1997). The quasi 2-day wave as seen from D1 LF wind measurements over Central Europe (52° N,15° E) at Collm. *J. Atmos. Solar-Terr. Phys.*, 11:1277–1286.
- Jakobs, H. J. (1986). *Untersuchungen von Schwerewelleneffekten mit Hilfe eines 3-d Zirkulationsmodelles der mittleren Atmosphäre*. Mitteilungen aus dem Institut für Geophysik und Meteorologie der Universität zu Köln, University of Cologne.
- Jakobs, H. J., Bischof, M., Ebel, A., and Speth, P. (1986). Simulation of gravity wave effects under solstice conditions using a 3-D circulation model of the middle atmosphere. *J. Atmos. Terr. Phys.*, 48:1203–1223.
- Johnson, R. and Killeen, T. (1995). *The Upper Mesosphere and Lower Thermosphere: A Review of Experiment and Theory*. American Geophysical Union.
- Kalchenko, B. and Bulgakov, S. (1973). Exploration of periodic components in the wind speed of lower thermosphere above the equator. *Geomag. and Aeronomy*, 13:1125–1126.
- Labitzke, K. and van Loon, H. (1988). Associations between the 11-year solar cycle, the QBO and the atmosphere. Part I: the troposphere and stratosphere in the northern hemisphere in winter. *J. Atmos. Terr. Phys.*, 50(3):197–206.
- Lange, M. (2001). *Modellstudien zum CO₂-anstieg und O₃-Abbau in der mittleren Atmosphäre und Einfluss des Polarwirbels auf die zonale Symmetrie des Windfeldes in der Mesopausenregion*. Rep. inst. meteorol. univ. leipzig, University of Leipzig.
- Liebermann, R. (1999). Eliassen-Palm Fluxes of the 2-day Wave. *J. Atmos. Sci.*, 56:2846–2861.
- Limpasuvan, V. (1998). *Tropical Dynamics near the stratopause: the Two-day Wave and Its Relatives*. PhD thesis, University of Washington.
- Limpasuvan, V., Leovy, C., and Orsolini, Y. (2000). Observed Temperature Two-day Wave and its Relatives near the Stratopause. *J. Atmos. Sci.*, 57(11):1689–1701.
- Lindzen, R. S. (1968). The application of classical atmospheric tidal theory. *Proc. R. Soc. London*, 303:299–316.

- Lindzen, R. S. (1981). Turbulence and stress owing to gravity wave and tidal breakdown. *J. Geophys. Res.*, 86:9709–9714.
- Liou, K. (1992). *Radiation and Cloud Processes in the Atmosphere*. Oxford Monographs on Geology and Geophysics No. 20.
- Longuet-Higgins, M. (1968). The eigenfunctions of Laplace's tidal equation over a sphere. *Phil. Trans. Roy. Soc. London*, 262:511–607.
- Manson, A., Meek, C., Luo, Y., Hocking, W., MacDougall, J., Riggin, D., Fritts, D., and Vincent, R. (2003). Modulation of gravity waves by planetary waves (2 and 16 d): observations with the North American-Pacific MLT-MFR radar network. *J. Atmos. Solar-Terr. Phys.*, 62:85–104.
- Marchuk, G., Dymnikov, V., Zalesny, V., Lykossov, V., and Galin, V. Y. (1984). *Mathematical Modelling of the General Circulation of the Atmosphere and Ocean*. Gidrometeoizdat.
- McCormack, J., Hood, L., Nagatani, R., Miller, A., Planet, W., and McPeters, R. (1997). Approximate separation of volcanic and 11-year signals in the SBUV-SBUV/2 total ozone record over the 1979-1995 period. *Geophys. Res. Lett.*, 24:2729–2732.
- McLandress, C. (2002). The seasonal variation of the propagating diurnal tide in the mesosphere and lower thermosphere. Part I: The role of gravity waves and planetary waves. *J. Atmos. Sci.*, 59:893–906.
- Medvedev, A. and Klaassen, G. P. (2003). Thermal effects of saturated gravity waves in the atmosphere. *J. Geophys. Res.*, 108, doi:10.1029/2002JD002504.
- Meek, C., Manson, A., Franke, S., Singer, W., Hoffman, P., Clark, R., Tsuda, T., Nakamura, T., Tsutsumi, M., Hagan, M., Fritts, D., Isler, J., and Portnyagin, Y. (1996). Global study of northern hemisphere quasi-2-day wave events in recent summers near 90 km altitude. *J. Atmos. Terr. Phys.*, 58(13):1401–1411.
- Merzlyakov, E. and Jacobi, C. (2004). Quasi two-day wave in an unstable summer atmosphere - some numerical results on excitation and propagation. *Ann. Geophysicae*, 22:1917–1929.
- Mlynzak, M. and Solomon, S. (1993). A detailed evaluation of the heating efficiency in the middle atmosphere. *J. Geophys. Res.*, 98:10517–10541.
- Monin, A. S. and Yaglom, A. M. (1975). *Statistical Fluid Mechanics: Mechanics of Turbulence*. MIT Press, Cambridge, Massachusetts.
- Muller, H. (1972). Long period wind oscillations. *Phil. Trans. Roy. Soc. London*, 272:585–598.

- Muller, H. and Nelson, L. (1978). A travelling quasi 2-day wave in the meteor region. *J. Atmos. Terr. Phys.*, 40:761–766.
- Norton, W. and Thuburn, J. (1996). The two-day wave in a middle atmosphere GCM. *Geophys. Res. Lett.*, 23:2113–2116.
- Norton, W. and Thuburn, J. (1999). Sensitivity of mesospheric flow, planetary waves, and tides to strength of gravity wave drag. *J. Geophys. Res.*, 24:30897–30911.
- Ogibalov, V., Fomichev, V., and Kutepov, A. (2000). Radiative Heating affected by Infrared CO_2 bands in the Middle and Upper Atmosphere. *Izvestiya, Atmospheric and Oceanic Physics*, 34(4):454–464.
- Orsolini, Y., Limpasuvan, V., and Leovy, C. (1997). The tropical stratopause in the UKMO stratospheric analyses: Evidence for a 2-day wave and inertial circulations. *Quart. J. R. Met. Soc.*, 123:1707–1724.
- Palo, S. E., Roble, R., and Hagan, M. (1999). Middle atmosphere effects of the Quasi-two-day wave determined from a General Circulation Model. *Earth Planets Space*, 51:629–647.
- Pancheva, D., Beard, A., Mitchell, N., and Muller, H. (2000). Nonlinear interactions between planetary waves in the mesosphere/lower-thermosphere region. *J. Geophys. Res.*, 105(A1):157–170.
- Pfister, L. (1985). Baroclinic Instability Jets with Applications to the Summer Mesosphere. *J. Atmos. Sci.*, 42(4):313–330.
- Phillips, N. A. (1966). The equations of motion for a shallow rotating atmosphere and the "traditional approximation". *J. Atmos. Sci.*, 24:537–550.
- Plumb, A. (1983a). Baroclinic Instability of the Summer Mesosphere: A Mechanism for the Quasi-Two-Day wave? *J. Atmos. Sci.*, 40:262–270.
- Plumb, A. (1983b). A new look at the energy cycle. *J. Atmos. Sci.*, 40:1669–1688.
- Plumb, A., Vincent, R., and Craig, R. (1987). The Quasi-Two-Day Wave Event of January 1984 and its Impact on the Mean Mesospheric Circulation. *J. Atmos. Sci.*, 44(20):3030–3036.
- Pogoreltsev, A. I. (1996). Production of electromagnetic field disturbances due to interaction between acoustic gravity waves and the ionospheric plasma. *J. Atmos. Terr. Phys.*, 56:1125–1141.
- Pogoreltsev, A. I., Pancheva, D., and Mitchell, N. (2002). Secondary planetary waves in the middle atmosphere: numerical simulation and analysis of the neutral wind data. *J. Atmos. Solar-Terr. Phys.*, 64:1251–1261.

- Pogoreltsev, A. I. and Pertsev, N. N. (1996). The influence of background wind on the formation of the acoustic-gravity wave structure in the thermosphere. *Izv. Acad. Sci. USSR Atmos. Oceanic Phys.*, 31:723–728.
- Poole, L. and Harris, T. (1995). The propagation of the mesospheric two-day wave in the southern hemisphere. *J. Atmos. Terr. Phys.*, 57:1661–1666.
- Randel, W. J. (1994). Observations of the 2-day Wave in NMC Stratospheric Analyses. *J. Atmos. Sci.*, 51(2):306–313.
- Riese, M., Offermann, D., and Brasseur, G. (1994). Energy released by recombination of atomic oxygen and related species at mesopause heights. *J. Geophys. Res.*, 99:14585–14593.
- Rodger, C. and Prata, A. (1981). Evidence for a Traveling Two-day Wave in the Middle Atmosphere. *J. Geophys. Res.*, 86(C10):9661–9664.
- Rose, K. (1983). On the influence of nonlinear wave-wave interactions in a 3-D primitive equation model for sudden stratospheric warmings. *Beitr. Phys. Atmosph.*, 56:14–41.
- Rottmann, G. (1999). Solar ultraviolet irradiance and its temporal variation. *J. Atmos. Solar-Terr. Phys.*, 61:37–44.
- Salby, M. (1981). The 2-Day Wave in the Middle Atmosphere: Observations and Theory. *J. Geophys. Res.*, 86(C10):9654–9660.
- Salby, M. and Callaghan, P. (2000). Seasonal Amplification of the 2-Day-Wave: Relationship between Normal Mode and Instability. *J. Atmos. Sci.*, 58:1858–1869.
- Salby, M. and Callaghan, P. (2003). Dynamics of the 2-day wave in a nonlinear model of the middle and upper atmosphere. *J. Geophys. Res.*, 108(23):1–13.
- Scaife, A., Austin, J., Butchart, N., Pawson, S., Keil, M., Nash, J., and James, I. (2000). Seasonal and interannual variability of the stratosphere diagnosed from UKMO TOVS analyses. *Quart. J. R. Met. Soc.*, 126:2585–2604.
- Schoeberl, M. F., Strobel, D. F., and Apruzese, J. P. (1983). A Numerical Model of Gravity Wave Breaking and Stress in the Mesosphere. *J. Geophys. Res.*, 88(C9):5249–5259.
- Schröder, H. (2003). *Kopplung von barotroper Instabilität und Trägheitsinstabilität - Die Zweitagewelle in der unteren Mesosphäre*. PhD thesis, Leibniz-Institut für Atmosphärenphysik e.V. an der Universität Rostock.
- Stening, R., Meek, A., Manson, A., and Stephenson, D. (1978). Winds and Wave Motions to 110 km at Midlatitudes. VI. Tidal, Gravity and Planetary Waves, 1976. *J. Atmos. Sci.*, 35:2194–2204.

- Strobel, D. (1978). Parameterization of the atmospheric heating rate from 15 to 120 km due to O_2 and O_3 Absorption of Solar Radiation. *J. Geophys. Res.*, 83(C12):6225–6230.
- Swartztrauber, P. and Kasahara, A. (1985). The vector harmonic analysis of Laplace’s tidal equations. *SIAM J. Sci. Stat. Comput.*, 6:464–491.
- Swinbank, R. and Ortland, D. (2003). Compilation of wind data for the Upper Atmosphere Research Satellite (UARS) Reference Atmosphere Project. *J. Geophys. Res.*, 108(19): doi:10.1029/2002JD003135.
- Teitelbaum, H. and Vial, F. (1991). On tidal variability induced by nonlinear interaction with planetary waves. *J. Geophys. Res.*, 96:14169–14178.
- Thayaparan, T., Hocking, W., and Mac Dougal, J. (1997). Amplitude, phase and period variations of the quasi 2-day wave in the mesosphere and lower thermosphere over London Ontario ($43^\circ N, 81^\circ W$), during 1993 and 1994. *J. Geophys. Res.*, 102:9461–9478.
- TIME-GCM (2004).
<http://www.hao.ucar.edu/public/research/tiso/tgcm/tgcm.html>.
- Tsuda, T., Kato, S., and Vincent, R. (1988). Long period wind oscillations observed by the Kyoto meteor radar and comparison of the quasi 2-day wave with Adelaide HF radar observations. *J. Atmos. Terr. Phys.*, 50(3):225–230.
- Ward, W., Wang, D., Solheim, B., and Shepherd, G. (1996). Observations of the two-day wave in WINDII data during January, 1993. *Geophys. Res. Lett.*, 23(21):2923–2926.
- Wu, D., Fishbein, E., Read, W., and Waters, J. (1996). Excitation and Evolution of the Quasi-2-Day Wave observed in UARS/MLS Temperature Measurements. *J. Atmos. Sci.*, 53:728–738.
- Wu, D., Hays, P., Skinner, W., Marshall, A., Lieberman, R., and Ortland, D. (1993). Observations of the quasi 2-day wave from the High Resolution Doppler Imager on UARS. *Geophys. Res. Lett.*, 20:2853–2856.
- Zhu, X. (1993). Radiative damping revisited: Parameterization of damping rate in the middle atmosphere. *J. Atmos. Sci.*, 50:3008–3021.

Acknowledgements

This work was supervised by Prof. Dr. Christoph Jacobi. I thank him very much for his support and guidance, his fair comments and fruitful discussions. The same gratitude I would like to express to Prof. Dr. Alexander Pogoreltsev for his suggestions und encouragement and his valuable work that led to an improved LIM-version of COMMA. Большое спасибо! Special thanks go to Evgeny Merzlaykov who was a good partner for discussions, particularly in the topic of unstable wave generation, and to Inna Fedulina who provided new climatologies for COMMA-LIM and contributed in this way to its actualisation. I thank also Martin Lange for introducing me to the work with COMMA.

I thank all former and today colleagues and fellow students at the Leipzig Institute for Meteorology for this time and for the valueable exchange of knowledge.

Furthermore, I would like to thank the colleagues of the MEDEC-project for the fruitful discussions and cooperation.

My great respect I want to express to Max for her bravery while reading and correcting my english script.

Thank you, Karsten, for your encouragement and your patience.

This work was supported by the BMBF under grant 07ATF10.

Werdegang

1977 – 1987	Polytechnische Oberschule „Nikolai Ostrowski“ Dobritz (Kreis Zerbst, Bezirk Magdeburg)
1987 – 1991	Ausbildung zur Krankenschwester an der Medizinischen Fachschule Dessau/Wittenberg
1991 – 1995	Krankenschwester am Elisabeth-Krankenhaus Leipzig
1994	Erhalt der Sonder-Hochschulzugangsberechtigung zum Studium der Meteorologie
1994 – 1995	Aneignung des Abiturstoffes in Mathematik im Selbststudium
1995 – 2001	Studium an der Universität Leipzig
1997	Vordiplom im Fach Meteorologie
2001	Diplom im Fach Meteorologie
2001 – 2004	wissenschaftliche Mitarbeiterin am Institut für Meteorologie der Universität Leipzig